# Development and Characterization of Pressure-Sensitive Microbeads for Simultaneous Barometry and Velocimetry for Fluid Dynamic Applications

Daniel J Lacroix

A thesis
submitted in partial fulfillment of the
requirements for the degree of

Master of Science

University of Washington
2014

Committee:
Dana Dabiri, Chair
Gamal Khalil

Program Authorized to Offer Degree:
Aeronautics and Astronautics

The views expressed in this article are those of the author and do not reflect the official policy or position of the United States Air Force, Department of Defense, or the U.S. Government.

University of Washington

## Abstract

Development and Characterization of Pressure-Sensitive Microbeads for Simultaneous Barometry and Velocimetry for Fluid Dynamic Applications

Daniel J Lacroix

Chair of the Supervisory Committee:
Dana Dabiri
Department of Aeronautics and Astronautics

The use of luminescent dyes to measure pressures and temperatures on surfaces using Pressure Sensitive Paint (PSP) and Temperature-Sensitive Paint (TSP) is a well-established methodology. New technology has allowed for microbeads to be loaded with pressure and/or temperature sensitive dyes. These microbeads can be seeded into flow fields in order to measure the pressure and/or temperature fields in the fluid flow. In addition, the microbeads act as tracer particles to the fluid velocity and therefore, standard PIV techniques can be applied to quantify the velocity of the flow simultaneously with the pressure and/or temperature measurement. Existing studies have investigated the use of polystyrene microbeads for simultaneous flow barometry and velocimetry yet the polystyrene microbeads have a slow response time to changing pressures, making them incapable of resolving accurate pressures in fast flow applications such as wind tunnels. In this contribution, silicon dioxide and oxide-based multi-dye microbeads were characterized and found to have much faster response times than polystyrene-based microbeads. The pressure response times and sensitivity of these microbeads were tested to determine the most viable candidate for future unsteady applications. It will also be shown that the intensity-based approach applied to these microbeads coated on a glass slide can be used to accurately measure pressure with a significantly high measure of precision and low pressure uncertainties down to 106Pa. Finally, this paper will demonstrate the feasibility of using aerosolized pressure-sensitive microbeads for simultaneous barometry and velocimetry for fluid dynamic applications.

# TABLE OF CONTENTS

# LIST OF FIGURES

# LIST OF TABLES

ACKNOWLEDGEMENTS

I would like to send out a special thank you to Professor Dana Dabiri and Professor Gamal Khalil for their continued support and guidance throughout this Master's program. I am also extremely grateful to Dr. Wei-Hsin Tien for his work on this project and mentorship throughout. I would also like to thank Julian Massing, Teddy Viraye-Chevalier, Jonathan Howard, Dr. Christian Cierpka, Guo-Shi Li, Guillaume Seiter, and Lillian Pryor for their work and contributions to this research, as well as Professor Younan Xia and Cun Zhu for their collaboration in development of the microbeads. Finally, I would like to recognize the staff and faculty of the University of Washington Aeronautics and Astronautics Department for giving me this great opportunity to further pursue my education.

# Chapter 1. INTRODUCTION

## *1.1. Pressure, Velocity, & Temperature in Fluid Mechanics*

### *1.1.1. Existing Techniques*

In fluid dynamics, quantifying pressure, velocity, and temperature are fundamental in understanding flow characteristics. Measuring these properties in experiments such as wind tunnels has become an important field of study. There are many different measurement devices that minimize interference with the flow but truly non-intrusive measurement techniques are the most desired. Pressure measurement in fluids is often determined from transducers but these devices often impinge on the flow. Difficulties can arise when trying to measure the pressure at locations where the probe would cause too much interference or a practical location is impossible. Velocity measurement of flow fields can be resolved using a number of different methodologies including pitot-static probes, thermal anemometry, Doppler anemometry, and Digital Particle Image Velocimetry (DPIV).[1] Temperature measurement has also been widely studied with many invasive and non-invasive methods such as thermocouples, liquid crystals, infrared thermometry, and thermal imaging.[2] Along with flow field measurement techniques, Pressure- and Temperature-Sensitive Paint (PSP/TSP) are well-established methods for quantifying pressure and temperature on surfaces and offer accurate techniques with minimal interference with the flow characteristics. Optical measurement techniques, such as PIV and PSP/TSP, are commonly used in various fields of research. They represent major advances over previous single-point measurement practices, as they allow for global measurements in two and three dimensions.

### *1.1.2. Pressure- & Temperature-Sensitive Paint*

PSP provides a technique for continuous and non-intrusive global mapping of pressure distributions over aerodynamically loaded surfaces.[3-6] PSP contains oxygen-sensitive molecules that are held within an oxygen permeable polymer binder. When illuminated by a light source, typically a laser, the molecules are excited to a higher energy state, and then release part of their energy as photons. Surrounding oxygen molecules can absorb these emitted photons. Hence, the

intensity of the luminescence observed is inversely proportional to the surrounding oxygen concentration within the surrounding atmosphere; this well-known phenomenon is called luminescence quenching and is illustrated in Figure 1.1. As concentration of oxygen in the air is proportional to pressure, PSPs can be used to accurately measure pressure. Similarly to PSP, TSP can be applied to surfaces to measure temperature distributions. The intensity of the emitted light is inversely proportional to temperature, due to thermal quenching. Over certain temperature ranges, it is possible to find a relationship between temperature and the luminescent intensity. This effect is described in detail in Liu and Sullivan.[6] In implementation, light sources with the appropriate wavelengths are used to illuminate the desired surface, and digital cameras are used to measure the light emissions from the PSP/TSP-painted surfaces, as described in detail in Khalil *et al.*[1]

This methodology has been successfully used in wind-tunnel applications[6-7] and is now commercially available.[8] Details of this methodology can be found in literature.[6-9] The use of PSP is becoming more common in large transonic tunnels, with production systems in use in several facilities such as AEDC,[10] ARA,[11] TsAGI,[12] and DLR.[13] Fast-responding PSP has been used in unsteady aerodynamic applications, such as airflow over rotor blades.[14] Furthermore, an excellent review of unsteady aerodynamic applications of PSP was presented by Gregory *et al.*[15]

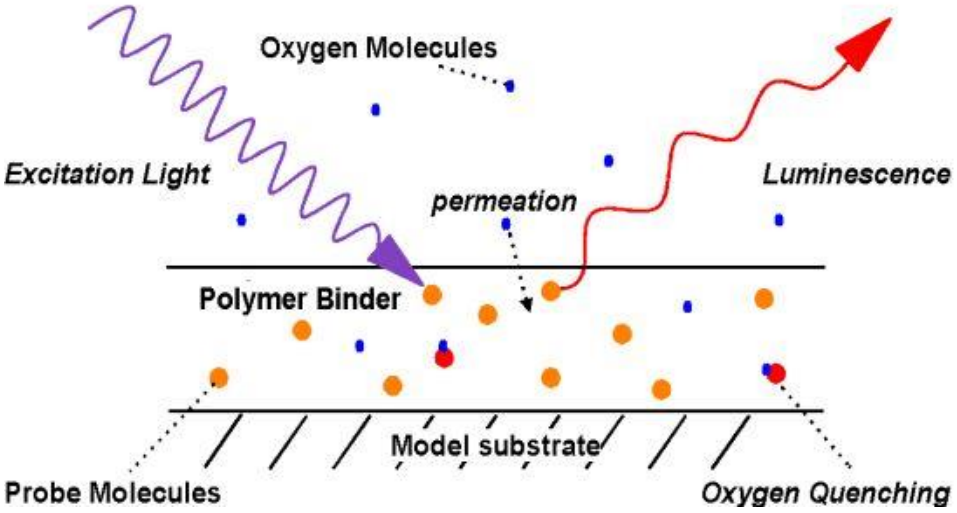


**Figure 1.1. Theoretical diagram of pressure sensitive paint.[16]**

.

### *1.1.3. Digital Particle Image Velocimetry*

DPIV is a well-developed technique that allows for simultaneous two–dimensional velocity measurement in unsteady flows.[17-18] A theoretical diagram of a traditional PIV setup is illustrated in Figure 1.2. The investigated flow is seeded with tracer beads that follow the flow. Upon illumination with a pulsed light source, two sequential images of the beads are obtained using digital cameras. A double pulsed laser is generally used to illuminate the particles with a short pulse difference in time. The velocity distribution can then be estimated through the bead displacements using cross-correlation methods and the elapsed time between two succeeding images.

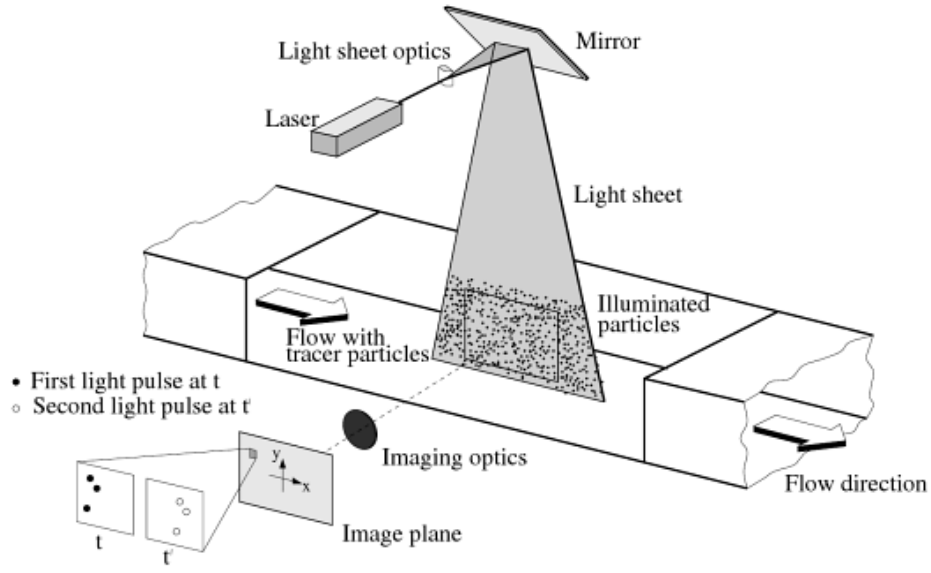


**Figure 1.2. Theoretical setup for PIV[19].**

## *1.2. Simultaneous Measurement (Motivation)*

The success of the PSP methodology has inspired the pursuit of globally measuring pressure within the fluid flow. The three techniques, PSP, TSP, and PIV, can be combined by doping microbeads with pressure- and temperature- sensitive dyes. With these so-called microbeads (PTSBeads) the pressure and temperature in the investigated flow region can be related to the emitted light. Correspondingly, the microbeads act as tracer particles in the fluid flow, thus enabling the use of PIV for determining velocities. Simultaneous measurement of these fluid properties offers extensive experimental possibilities. This measurement technique

would present a new procedure for determining these flow properties in time sensitive experiments such as turbulence and other unsteady aerodynamic conditions.

## *1.3. Current Technology*

Abe *et al.*[20] and Kimura *et al.*[21] showed the validity of this concept by simultaneously measuring velocity and pressure in a small test chamber using aerosolized pressure-sensitive microbeads (PSBeads). The pressure distributions were determined by a lifetime measurement method, which takes two images of the microbeads, coated with a pressure-sensitive dye, in rapid succession and relates the intensity decay to determine the lifetime. In addition to the intensity, the luminescent lifetime of the pressure-sensitive dye is dependent on the oxygen concentration and therefore, the calculated lifetimes can be calibrated to pressures. In these investigations, it was qualitatively shown that pressure variations could be observed within the flow but the uncertainties from the lifetime method pressures were significantly high.

More recently, dual- and multi-luminophor polystyrene microbeads (1-5μm diameters) have been developed by our groups. With these microbeads the pressure- and temperature-sensitive dyes are loaded together with a pressure- and temperature-insensitive dye which allows for self-referencing microbeads.[22] This lab has further demonstrated that these microbeads can be used to measure pressure and temperature simultaneously.[23] In contrast to the method used by Kimura *et al.*,[21] these microbeads use the intensity and not the lifetime of the emitted light to obtain pressure. The settings and excitation conditions during the measurements must not vary significantly, which cannot be ensured during fluid flow measurements, due to bead movement. This requires the intensity variations due to pressure to be compared against the reference intensity that is insensitive to pressure and temperature variations. For this reason, microbeads that are only doped with PSP dyes are insufficient for intensity-based measurements. Thus, the reference dye is crucial to account for these variations. The emitted light from each dye has its own unique wavelength and is captured on separate cameras. The ratios of both images are then calibrated to the pressure values.

Previous studies with an intensity-based method (Khalil *et al.*[24]; Gouterman *et al.*[25]; Im *et al.*[22]; Kose *et al.*[26,27]), demonstrated the feasibility of this methodology using multi-luminophor surface paints in wind tunnel applications. However, the use of multi-dye microbeads and an intensity-based method for flow field pressure measurement has not been fully investigated.

Furthermore, the polystyrene microbeads developed and tested in previous research have demonstrated slow response times.[28] For unsteady aerodynamic applications, with the microbeads following the flow and acting as tracer particles, they must react fast enough to changing pressure conditions to resolve the unsteady nature of the flow. A need for a faster microbead to replace the polystyrene microbead and the development of an intensity-based calibration method for aerosolized applications was evident.

## *1.4. Objectives*

The aim of this research was to characterize newly developed microbeads as an alternative to the polystyrene microbeads used previously. The method of manufacturing, response times, and pressure sensitivity of different particle and dye combinations were investigated to discover a viable option for a fast responding, pressure sensitive particle for use in eventual unsteady applications. Secondly, the existing polystyrene microbeads were used to investigate the intensity-based calibration technique for pressure measurements. Initial characterization of the microbeads for an intensity-based method was investigated followed by a similar experiment to that of Kimura *et al.*[21] to measure the pressure distribution in a small chamber. Experimentations of stationary microbeads were performed on a glass slide in order to develop the calibration techniques for eventual aerosolized microbead pressure measurements. Finally, testing of aerosolized polystyrene microbeads was conducted to get a preliminary understanding of the experimentation and challenges associated with it.

Chapter 2 will begin with a discussion of the theory behind the response times of pressure-sensitive dyes and microbeads. The experimental facility and results from the characterization of the fast-responding microbeads will be presented. Chapter 3 will outline the theory for surface PSP measurement as well as the eventual wind tunnel application with aerosolized microbeads. This paper will discuss the experimental system used to capture the sequences of pressure and reference emission images, the calibration processing technique for calculating pressures from these images, and the results of the technique. The work will show the feasibility of the intensity-ratio approach for stationary dual-luminophor PSBeads. Furthermore, the paper will outline the development of a highly robust calibration technique for pressure measurement of these stationary PSBeads. Lastly, the results from initial aerosolized microbeads

tests will be presented, which combine this pressure measurement technique with particle image velocimetry.

# Chapter 2. TESTING & CHARACTERIZING FAST RESPONDING PTSBEADS

## *2.1. Response Time Theory*

Although these microbeads can accurately measure pressures and temperatures, it is essential to quantify the response time to changing pressures and temperature to determine whether the microbeads can adequately perform their function in unsteady environments. The microbeads must respond sufficiently fast to capture rapid changes in pressures and temperatures if they are to be used in conjunction with unsteady flow fields alongside steady aerodynamic regions. The response time of PSPs has been described as being dependent on three important parameters: Luminescent lifetime of the luminophor, the oxygen diffusivity, and thickness of matrix layer. Kimura *et al.*[21] used the lifetime in a previous study where it was shown that the scope of the luminophors' lifetime spans from 1μs to 50μs. The estimation of the 99% rise time of a thin PSP layer can be expressed as:

$$\tau_{99\%} = \frac{12 \times L^2}{\pi^2 \times D}$$

and

$$\tau_{99\%} = \frac{3 \times d^2}{4 \times \pi^2 \times D}$$

for a microbead, where L is the thickness of the layer, d is the diameter of the bead, and D is the oxygen diffusion coefficient of the matrix being used.[29-31] Hence, to develop a fast responding microbead, a compromise would have to be made between the thickness of the layer and the oxygen diffusion coefficient. Kimura *et al.*[28] reported that the response times for 2 μm diameter polystyrene microbeads are estimated to range from 9.8ms to 27.6ms, which would be too slow for desired applications, such as measuring pressure changes in turbulent flows. This led to initial research involving the synthesis of a new type of microbead using a highly porous silicon dioxide structure containing novel pressure-sensitive osmium complexes, with a much faster response time (Kimura *et al.*[28]). While successful, the osmium-based silicon dioxide microbeads had a very low signal-to-noise ratio. Towards this end, research was conducted to exhibit the improvements upon the synthesis of silica microbeads with higher signal-to-noise ratios using

new multi-loaded dyes, while maintaining sensitivity and fast response times. Furthermore, the improvements on the microbead manufacturing led to investigations of a new particle with similar traits to that of the silica microbead. The newly developed particles and dye combinations were characterized for the most superior pressure response and response time.

### *2.1.1. Shock Tube*

Following alongside the development of PSP, different measurement devices for response time have been implemented such as shock tubes, solenoid valve, loudspeaker, periodic shock generator, and fluidic oscillator.[15] The shock tube presents the most common device for generating fast, unsteady pressure changes and was used in this experiment for measuring the response time of the pressure-sensitive microbeads. The shock tube consists of two sections with different pressures, separated by a diaphragm. When the pressure difference is high enough, the force bursts the diaphragm and sends a compression wave down the low pressure section and expansion waves down the opposite, high pressure section. The compression waves quickly form a normal shock wave that propagates downstream and generates a near-instantaneous pressure rise. A theoretical diagram of the shock tube device and the traveling waves over time are illustrated in Figure 2.1.

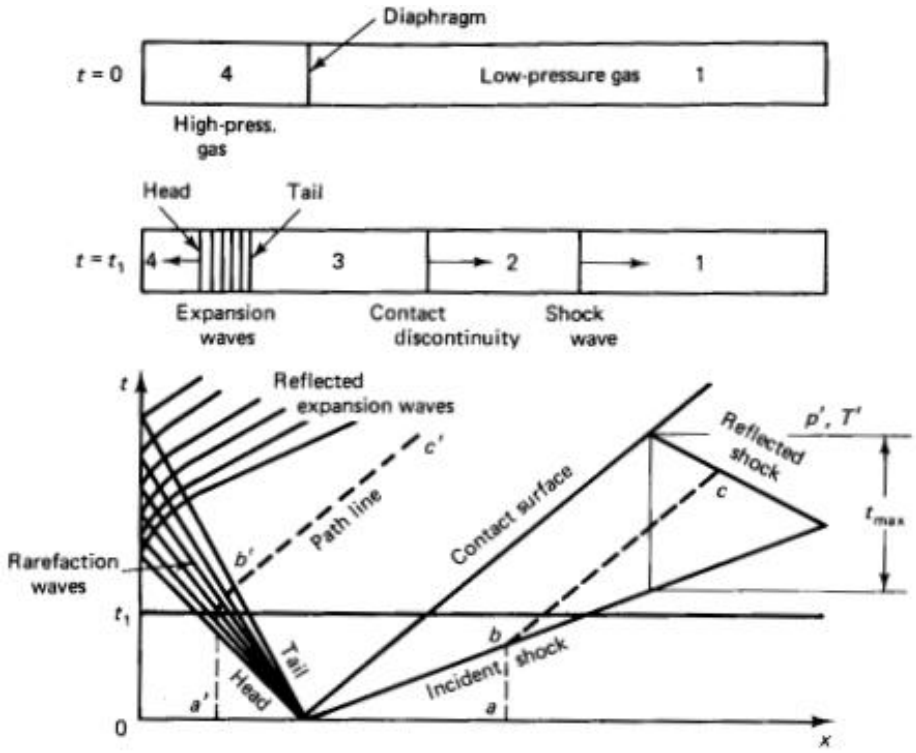


**Figure 2.1. Theoretical diagram of a shock tube.**[32]

## *2.2. Experimental Setup*

The first phase of the experiment involved gathering the various chemicals and materials for microbead manufacturing. Cetyltrimethylammonium bromide (CTAB), ammonium hydroxide ($NH_3$•$H_2O$, 28% $NH_3$ in $H_2O$), tetraethyl orthosilicate (TEOS), methanol, ethanol, acetone, and dichloromethane were all purchased from Sigma-Aldrich. Deionized water with a resistivity of 18.2 MΩ•cm was used for all the syntheses. The initial testing with the silica particles involved loading the microbeads with three different luminescent dyes. The first type was from a family of pressure-sensitive dyes composed of Pt(II)octaethylporphine (dye A), Pt(II) meso-Tetra(pentafluorophenyl)Porphine (dye B), and Bis(3,5-difluoro-2-(2-*pyridyl)phenyl-(2-carboxypyridyl)iridium III (dye D). The respective emission wavelengths of the pressure dyes are 650 nm, 650 nm and 500 nm. The second type of dye corresponds to a reference dye, Coumarin 500 (dye H) or Mg(II)meso-Tetra(pentafluorophenyl)Porphine (dye J). Their emission wavelengths are 530 nm and 650 nm respectively. The emission intensities of both reference dyes are insensitive to pressure and temperature changes. The third dye incorporated in the microbeads was the temperature-sensitive dye Eu(III)thenoyltrifloroacetonate (dye E) with a 615 nm emission wavelength. Dyes A, B, J are from Frontier Scientific, dyes C, D, H are from Luminescence Technology Corporation and dye E is from Gelest. All chemicals were used as received. These materials were used to prepare mesoporous silica microbeads per the synthesis methods described below, where the mesopores are estimated to be 1-2nm in size. The CTAB molecules serve as templates for the generation of these mesopores during the synthesis process.

With the various luminescent dyes, mesoporous silica microbeads were loaded with different dye combinations using a one-step method. In a typical synthesis, 0.4 g of CTAB, 167 mL of methanol, 30 mL of water, and 11 ml of $NH_3$•$H_2O$ were mixed in a 250 mL flask under magnetic stirring. Meanwhile, the different combinations of dyes with specific amounts were dissolved in 1.5 mL of acetone. The dyes were then introduced into the mixture, followed by rapid injection of 0.6 mL of TEOS using a pipette. The reaction was allowed to proceed at room temperature for 24 h. The resultant functionalized mesoporous silica microbeads were collected by centrifugation and washed with water three times.

To complement the one-step method, the silica microbeads were also loaded with the dyes in a second, two-step method. The two-step procedure was composed of the synthesis of mesoporous silica beads utilizing a seed-mediated process, and the loading of dyes into the as-

obtained silica beads. In a typical synthesis, 100 mg of CTAB, 40 mL of methanol, 7.5 mL of $H_2O$, and 3 mL of $NH_3 \bullet H_2O$ were placed in a 100 mL flask, followed by the introduction of 25 μL of TEOS to generate primary silica seeds. After the reaction was proceeded for 1.5 h, 2.4 mL of TEOS was injected into the solution at the rate of 0.4 mL/h with the help of a syringe pump to start the growth. The reaction was allowed to proceed at room temperature under magnetic stirring for 24 h. The resultant mesoporous silica microbeads were collected by centrifugation and washed with ethanol three times. The products were dispersed in 5 mL of ethanol for further use. For the loading of dyes, different combinations of dyes with specific amounts were dissolved in 1.5 mL of acetone at room temperature, and then introduced into 1.5 mL of as-obtained silica beads. The mixture was ultrasonically dispersed for 1 h and then magnetically stirred overnight. The final products were collected by centrifugation and washed with water three times.

Additionally, larger size silica microbeads were used in the fabrication process. For these ~14 μm in diameter hollow glass spheres, Sphericel 110P8, from Potters Industries were used and loaded with dyes. When reporting results in the following sections, the synthesized silica microbeads are identified with an asterisk (*).

Several iterations of different dye concentrations were synthesized. For example, microbead samples were loaded with different ratios of the B:E:H dyes. Over 60 samples of microbeads were evaluated for spectral characteristics and response time to pressure jumps. Test samples were made by drop-casting 100μl of water suspension (~10% solids) of the microbeads onto the surface glass slide of 3cm by 1cm. The samples were dried in an oven set at 70°C.

A shock tube was used for this study to measure the response time of the microbeads to rapid pressure jumps. Other techniques for response time have been studied[33] though the shock tube presented a reliable method for determining response times of pressure rises at the microsecond scale. Gregory and Sullivan[33] characterized the response time of pressure sensitive paints using a Fluidic Oscillator and found that the paints responded faster to pressure decreases than to pressure increases. Thus, this research focused on pressure rises as the limiting factor to response time. The shock tube setup consisted of a square aluminum tube with walls 0.64 cm thick, with a cross section of 3.9 cm by 3.9 cm. The schematic of the testing facility is presented below in Figure 2.2.

The shock tube was assembled by two main sections, a 3.1 m long expansion (driver) chamber and a 1.8 m long compression (driven) chamber. A diaphragm was positioned at the connection between the two sections that burst when the pressure difference between both chambers was high enough, causing a shockwave to propagate down the compression section. Further details on the theory and testing of shock tubes can be found in textbooks[32] and in Kimura *et al.*[28], respectively. The diaphragm was initially made of Parafilm® M (127 μm in thickness, Bemis flexible Packaging, Neenah, WI) and the thickness was varied by modifying the number of layers of Parafilm, thereby changing the pressure difference between the two sections at the instance of the diaphragm bursting. A configuration of six layers of Parafilm was used as the pressure decreased from 100kPa to 4kPa, a pressure ratio obtained of 1/25.

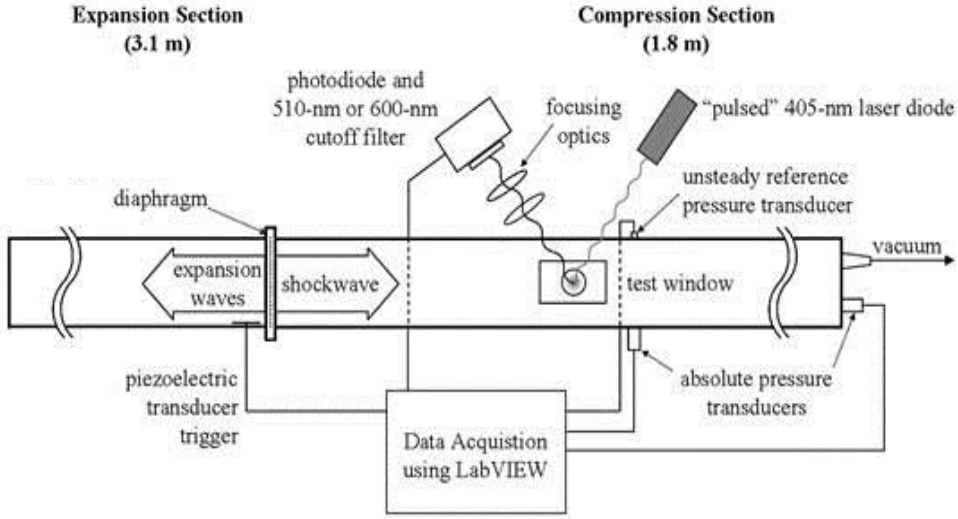


**Figure 2.2. Schematic of the shock tube**

The pressure difference was established in one of two ways: A vacuum pump was used to directly pump out the air in the compression chamber or used to generate low pressure in a large tank, which was then connected to the compression chamber. The motivation for using the latter was to reduce the wait time for the vacuum pump to lower the pressure directly in the compression section. Two 1.9 cm by 3.8 cm test windows, on which the microbeads test samples were mounted, were positioned 0.58 m downstream of the diaphragm. Samples were placed on this top window of the shock tube, oriented face down, in order to reduce the optical interference of the shockwave with the illuminating samples, but still maintain a direct face on the passing shockwave.

Unsteady and steady pressures were measured 0.12 m downstream of the test window using a high sensitivity dynamic pressure sensor with a 90% rise time of 2 μs (model 211B5,

Kistler Instruments, Amherst, NY) attached to a power supply coupler (model 5114, Kistler Instruments, Amherst, NY) for the unsteady pressure measurements. For the steady pressure measurements, an Omega PX236 series pressure transducer was used. The pressure transducers were positioned in the tube flush with the walls so as to not interfere with the flow. The stated accuracy of the steady pressure transducers were 0.25% of the full scale.

The detection system was composed of a 405 nm continuous laser light used to excite the microbeads. The test sample was attached to the top window such that the microbeads were facing down in direct contact to the shock wave. The light emitted by the test sample was focused on a Photomultiplier (PMT Hamamatsu R928) fitted with a band-pass filter at the appropriate wavelength. The PMT had a 2.2 μs rise time and a gain of 107 for an applied voltage of 1000 V. Additionally, a band-pass filter was positioned in front of the laser to reject any other wavelengths. Furthermore, the data from each transducer used were processed by Signal Express Labview through the National Instruments data acquisition board (BNC-2120) connected to the computer, sampling at 100k samples/sec.

Once the sample was placed onto the window, the vacuum pump pumped down the downstream section of the shock tube until the diaphragm burst, all the while the pressure and intensity data were being recorded. The data obtained were exported, plotted, and processed with Excel to calculate the response time of the tested microbeads based on a 63.2% and 90% rise time of the intensity change. Although the responses of PSPs have been shown to follow exponential models, it is more useful to characterize the response time as single numbers rather than exponential models and associated time constants[34].

Following the evaluation of the silica microbeads, experimentation into a newly developed in-house pressure-sensitive microbead was conducted. Several additional pressure-sensitive luminophors and different types of mesoporous microbeads were gathered in addition to the already tested pressure-sensitive silica microbead combinations. Along with dyes A, B, and D, Pt(II) meso-Tetra(Pentafluorophenyl)Porpholactone (designated dye Pt(II) Lactone), Acridine orange (dye A.Orange), tris-(Bathophenanthroline)Ruthenium(II)chloride (dye Ruthenium), and Iridium(III) Bis(3-[2- benzothiazolyl]coumarin)Hexafluoroacetylacetone (dye $D^{+}$) where purchased as pressure-sensitive dyes. The respective peak emissions wavelengths for these dyes are 645nm, 640nm, 595nm, and 585nm. Furthermore, along with the silica particles, aluminum oxide ($Al_2O_3$), zinc oxide (ZnO), and calcium carbonate ($CaCO_3$) microbeads were

gathered for pressure-sensitive testing. The various pressure-sensitive dyes were loaded to the particles in different combinations for single-dye particle testing.

For each dye-particle combination, response times were determined with the same shock tube setup as with the silica particle testing with the exception of two aspects. The Parafilm diagraph was switched out for an aluminum foil diaphragm to generate a faster and cleaner shock as the aluminum foil provided a brittle sheet that burst more instantaneous than the extreme elastic behavior of the Parafilm during the diaphragm bursting. Furthermore, the vacuum pump was used to pump down the pressure in a large air tank, which was then used to quickly vacuum the compression section of the shock tube, rather than having the pump directly attached to the shock tube. This also benefited towards a faster and cleaner shock for the response times. Alongside the testing to ensure that the pressure-sensitive microbeads maintained microsecond response times, the pressure sensitivity of the dye-particle combinations was measured based on the Stern-Volmer relationship[35] of emission intensity to pressure.

The experimental setup for acquiring the pressure sensitivity data from these dye-particle samples is shown in Figure 2.3 and consists of an aluminum chamber, with exterior dimensions of 35cm x 5cm x 5cm. Its interior test section dimensions are 6cm x 4cm x 4cm. The sample of microbeads was secured on a glass slide and then placed inside this test section for experimentation. A cylindrical opening with a diameter of 2.5cm and a length of 12cm was cut into the end of the block. It holds a 60ml syringe plunger, which was pulled out or pushed in to alter the pressure inside the chamber from approximately 70kPa to around 150kPa. A vacuum pump was attached to the end of the chamber in order to achieve pressures from 100kPa down to 2kPa. The optical measurements were performed through 6cm x 2.5cm quartz glass windows on the top, front and bottom faces of the chamber.

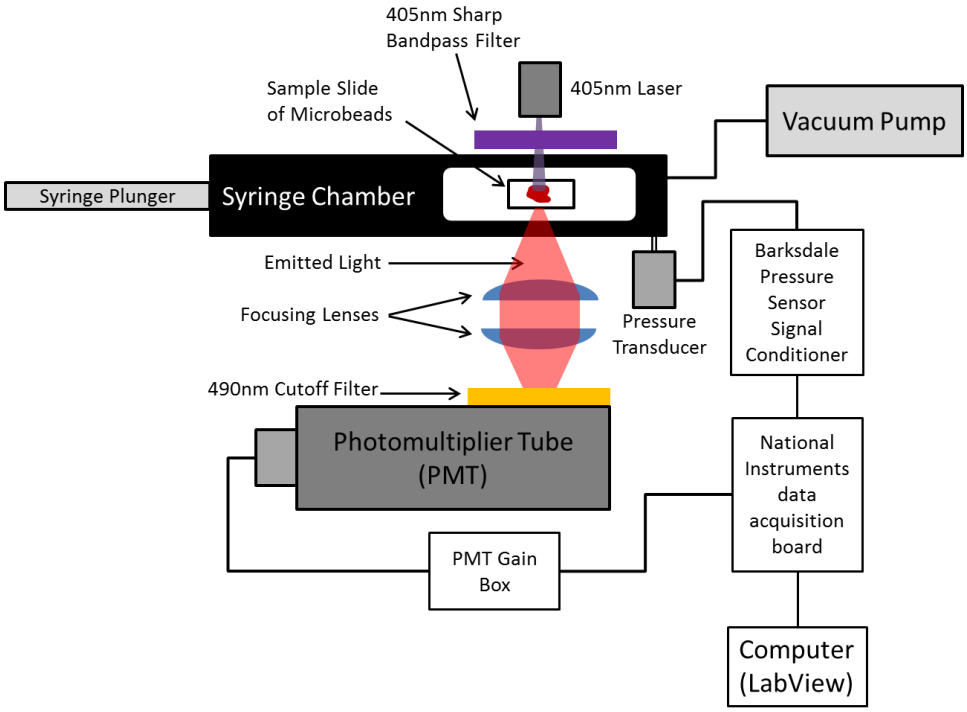


**Figure 2.3. Schematic of Stern-Volmer testing of single-dye (multi-dye required different cutoff filter) pressure-sensitive beads in the test chamber.**

The 405nm continuous laser, as in the shock tube setup, was used as the excitation source and again, the emitted light was focused onto the PMT. For single-dye particle testing the optical filter in front of the PMT was a 490nm cutoff filter to remove the reflected laser light but maximize the emission from the pressure-sensitive luminophor. Using the 490nm filter with a cutoff just above the laser allowed for a consistent optical filter for each of the different pressure-sensitive dyes tested. A Barksdale 402h2 Series pressure transducer with a pressure range of 0-50 psi and an accuracy of 0.25% was used to monitor the pressure throughout the experiment. The signal from this transducer was sent to a Barksdale pressure sensor signal conditioner and recorded, alongside the PMT signal, with LabVIEW.

While recording the emissions intensity and pressure of the chamber, the syringe was pushed in to achieve pressures from atmospheric to around 150kPa. Immediately following this, the valve to the vacuum pump was opened to release the positive pressure before pumping the chamber down to near-vacuum pressures. The data were processed in MATLAB in order to produce the Stern-Volmer plots of emission intensity, normalized with atmospheric intensity, against pressure. Further details of the Stern-Volmer test setup and experimentation, processing, and plotting can be found in the Appendix. Both the pressure-sensitivity and response times of

these different particles were analyzed in comparison to each other and to the silica PTSBeads in order to determine the best particle and pressure luminophor potentials for further development.

## *2.3. Results*

### *2.3.1. Fast Responding Silica Particle*

At first, the emitted light spectrums of the silica microbeads were examined to determine whether the particular samples of silica microbeads were sufficiently illuminating at the wavelengths of each dye. An example of several silica microbeads is shown in Figure 2.4 which illustrates the spectral response of the particular set of silica microbeads.

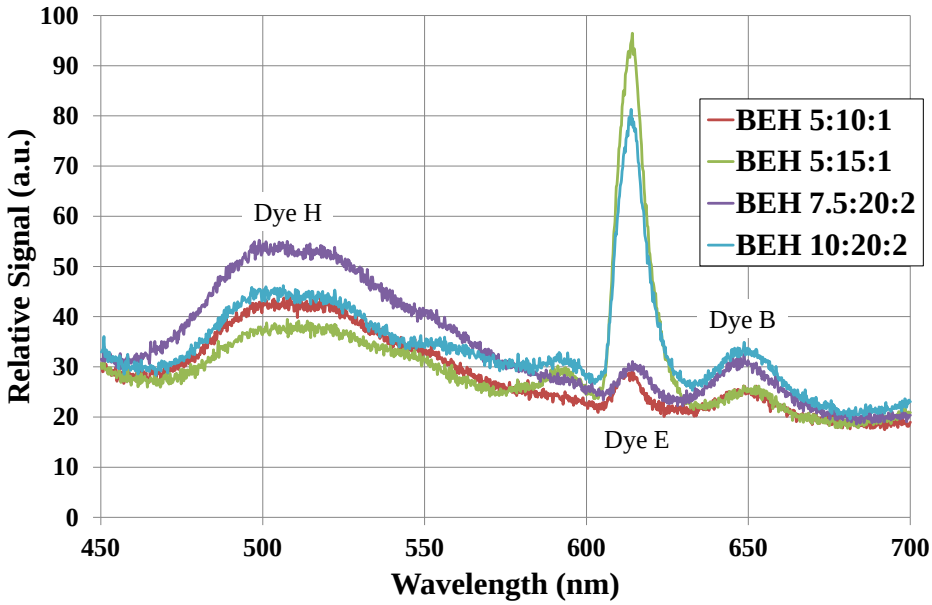


**Figure 2.4. Emission spectra of several silica microbeads excited with a 365 nm LED showing the wavelengths of the different dyes loaded into the silica microbeads.**

In order to demonstrate that our procedures in determining response time were sufficient, initial tests of silica BEH* microbeads (again, the * denoting silica microbeads synthesized by the Xia research group rather than commercial silica microbeads) were performed and the signals for each of the three dyes incorporated into the microbeads was captured. Figure 2.5 shows these microbeads' response to a pressure jump along with the dynamic pressure transducer.
The initial pressure of the driven and driver chamber, P1 and P4, were respectively 4 kPa and 100 kPa with a six-layered Parafilm diaphragm. The dye intensity data presented in Figure 2.5 exhibit a relative magnitude of the signals in order to prove that the variation of the reference dye and the temperature signals are very small compared to the change of emitted light intensity by

the pressure dye. The decrease in signal of the differential pressure transducer after the shock is seen as a slight rise in pressure dye, although this is not a part of the response time. As a result, this proved that the testing facility along with the microbeads tested was reliable as a means for measuring pressure change within a flow field.

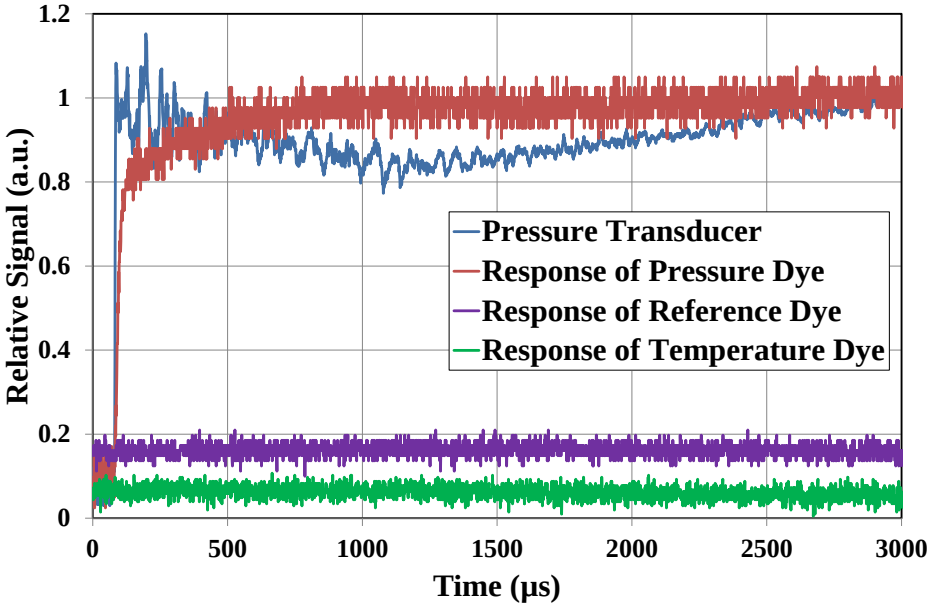


**Figure 2.5. Plot of the intensity changes of Silica BEH* (10:25:0.5) microbeads excited with a continuous 405 nm laser light for each dye incorporated into the microbeads as well as the dynamic pressure sensor.**

In this research, the signal-to-noise ratio was a significant concern in the way that it needed to be high enough to prove the efficiency of the microbeads tested as a tool for measuring pressure within an unsteady fluid flow. A specific criterion for a signal-to-noise ratio of approximately 16 was used to assess whether the microbeads would be adequate for testing. Additionally, the data presented in this study were ten point averages of the raw data processed in LabVIEW. An average of the raw signal was performed in order to reduce the noise that still persists in addition to smoothing out the curve for better response time calculations.

All the data obtained were analyzed in order to find the response times of each sample as explained above. A summary table of the testing and response time results is presented in Table 2.1. The range of response times at 90% rise time due to the shock wave spreads from 26 µs to 1582 µs. For reference, the response times of polystyrene microbeads (following previous procedures[36] are also included, which show that they are the largest response times, which is consistent with previous results[Error! Bookmark not defined.]. The polystyrene and silica microbead esponse time comparison is also shown in Figure 2.6.

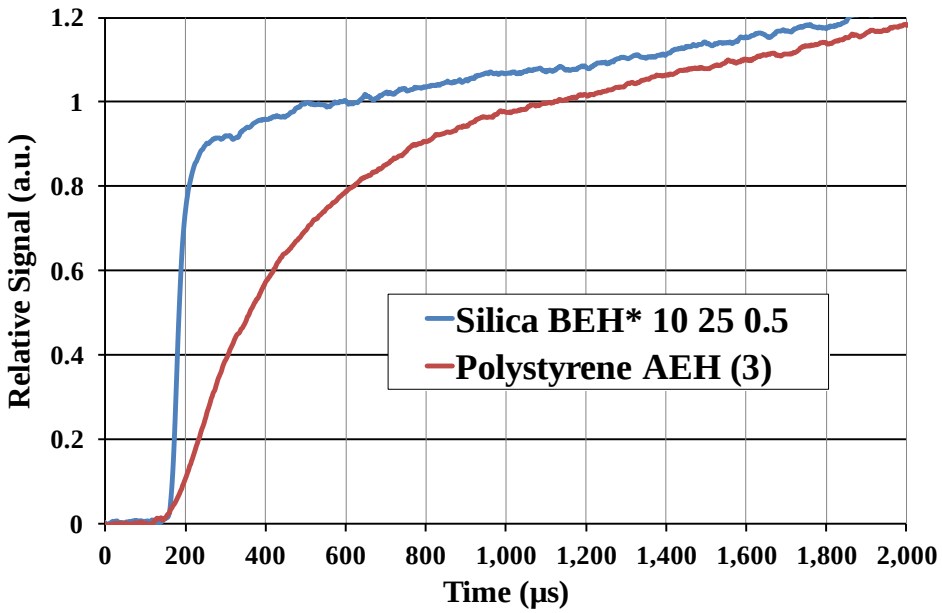


**Figure 2.6. Plot of the response time of a silica two-step fabrication method BEH microbeads test and a polystyrene AEH microbeads test excited with a continuous 405 nm laser light showing significantly slow response time from the polystyrene microbeads.**

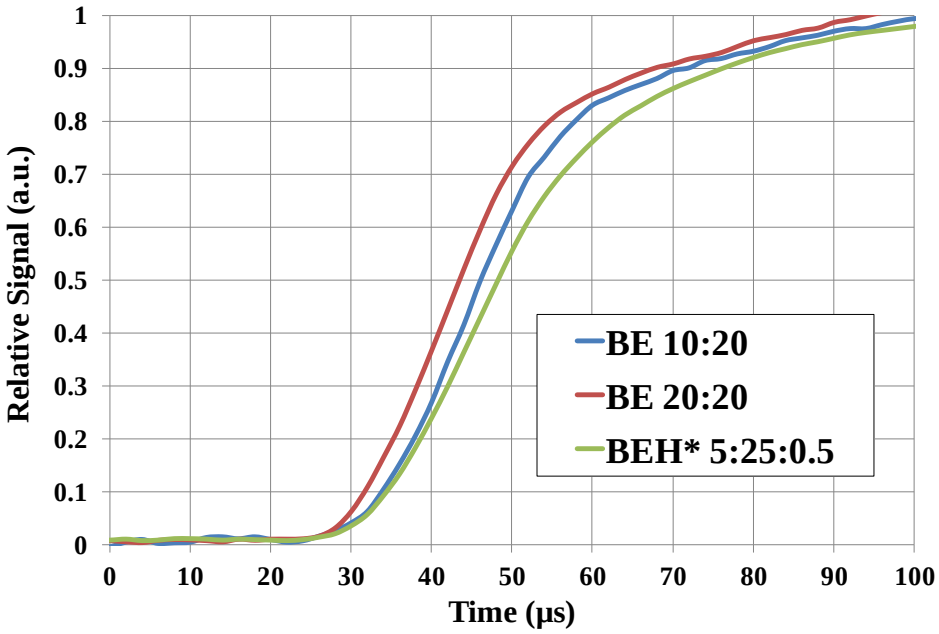


**Figure 2.7. Plot of the response time of fastest BE (two-step) and BEH (two-step) microbeads excited with a continuous 405 nm laser light showing consistency of fast responding two-step fabrication method.**

While Figure 2.6 shows that the two-step fabrication method of the silica microbeads has a faster response time than the polystyrene microbeads, it is also seen in Table 2.1 that the two-step fabrication method consistently demonstrates faster response times than the one-step fabrication method. The BEH* microbeads fabricated using the one-step method has average

(n=4) 63.2% and 90% response time values of 114 µs and 204 µs, respectively, with standard deviations of 69 µs and 117 µs. However, the BEH and BEH* (both commercial silica microbeads and microbeads synthesized during the fabrication process) fabricated using the two-step method has respective averages of 41 µs and 79 µs, with standard deviations of 25 µs and 66 µs. Therefore, the average response time using the two-step fabrication method was approximately a third of that using the one-step method, with significantly lower deviations. Lastly, the silica BE microbeads were the final and best effort to create microbeads using the two-step method and resulted in the fastest response times, with an averaged 63.2% and 90% rise time of 18 µs and 29 µs, respectively, with 2.8 µs and 4.2 µs standard deviations, respectively. A plot of several silica microbeads tests is presented in Figure 2.7, which illustrates the consistency of fast responding microbeads using the two-step fabrication method.

Correspondingly, Figure 2.8 presents a plot of a one-step fabrication method silica microbeads test and a two-step fabrication method test further showing the slow response time of the one-step method compared to that of the two-step method. Furthermore, the microbeads loading did not seem to affect the response time, as Table 2.1 shows no distinct relationship between the dye loading and better response times.

**Table 2.1. Calculated response times for samples of microbeads tested within the shock tube facility.**

| Sample | Fabrication Method | Dyes ratio | Response time (μs) | |
|---|---|---|---|---|
| | | | 63.2% | 90% |
| Silica BEH* | One step[36,22] | BEH* (5:50:0.05) | 20 | 28 |
| Silica BEH* | | BEH* (10:50:0.05) | 180 | 268 |
| Silica BEH* | | BEH* (10:50:0.05) | 144 | 266 |
| Silica BEH* | | BEH* (10:50:0.5) | 112 | 252 |
| Silica BH* | Two steps | BH* (10:0.5) | 26 | 60 |
| Silica BEH | | BEH (5:25:0.5) | 24 | 44 |
| Silica BEH* | | BEH* (5:25:0.5) | 26 | 50 |
| Silica BEH* | | BEH* (10:25:0.5) | 30 | 52 |
| Silica BEH* | | BEH* (10:25:0.5) | 56 | 80 |
| Silica BEH* | | BEH* (5:25:0.25) | 24 | 44 |
| Silica BEH* | | BEH* (10:25:5) | 40 | 84 |
| Silica BEH* | | BEH* (5:25:0.5) | 54 | 78 |
| Silica BEH* | | BEH* (5:10:0.5) | 64 | 90 |
| Silica BEH* | | BEH* (5:15:1) | 28 | 42 |
| Silica BEH | | BEH (15:20:2) | 46 | 78 |
| Silica BEH | | BEH (10:20:20) | 28 | 62 |
| Silica BEH* | | BEH* (5:15:1) | 24 | 52 |
| Silica BEH* | | BEH* (7.5:20:2) | 24 | 52 |
| Silica BEH* | | BEH* (10:20:2) | 30 | 64 |
| Silica BEH | | BEH (10:20:1) | 118 | 310 |
| Silica DJ* | | DJ* (10:1) | 150 | 462 |
| Silica BE | | BE (10:20) | 16 | 26 |
| Silica BE | | BE (20:20) | 20 | 32 |
| Polystyrene AEH | One step[36,22] | AEH | 276 | 507 |
| Polystyrene AEH | | AEH | 716 | 1582 |

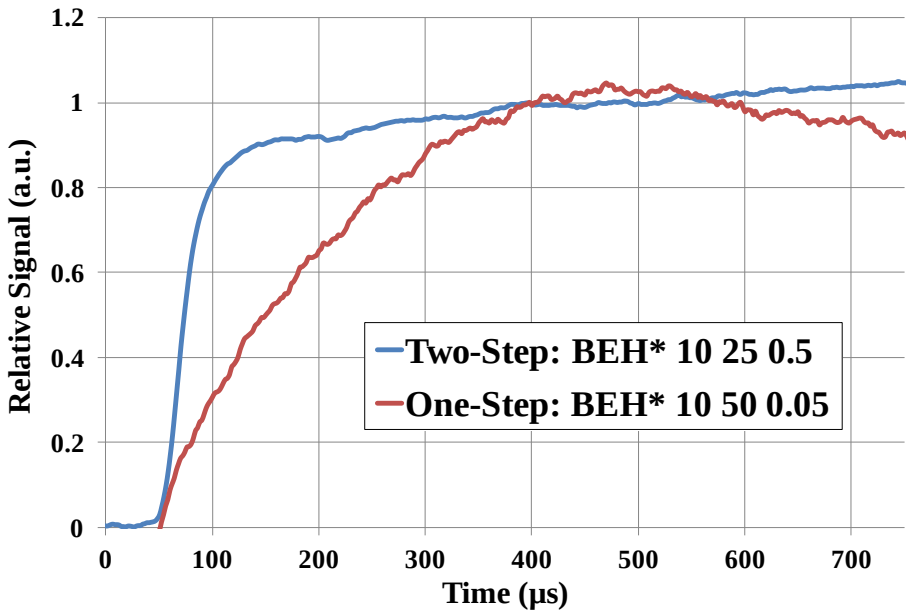


**Figure 2.8. Plot of the response time of a one-step BEH microbeads test and a two-step BEH microbeads test excited with a continuous 405 nm laser light comparing the two different fabrication methods.**

One additional investigation involved testing some of the microbead samples using a different illumination pattern. Instead of illuminating the test sample with a laser spot that ranged from 5 mm to 10 mm in diameter, a 1 mm thick laser line was created, using a cylindrical lens, to illuminate the test sample perpendicular to the direction of the shock propagation. As the shock transit time over the laser line is much quicker than over the laser spot, the motivation for this change was to investigate whether the measured response time would be more precise. The results of these tests did not show improvements in the response time, therefore suggesting that the laser line illumination was not necessary, and that a laser spot was sufficient.

### *2.3.2. New In-House Manufactured Particles*

Following the silica microbeads development, new types of microbeads and pressure-sensitive dye combinations were tested for both pressure sensitivity and response time due to rapid pressure changes. The pressure-sensitive dyes loaded to particular particles were tested for pressure sensitivity by the Stern-Volmer relationship of normalized intensity to pressure. A new experimental setup was utilized to generate the Stern-Volmer plots and achieve intensities for positive pressures, above atmospheric, as well as the pressures down to near-vacuum. With the data obtained from LabVIEW the intensities across the range of pressures were smoothed and

filtered in MATLAB before plotting to reduce noise and random signal variations. An example plot of the normalized intensity and pressure data is shown in Figure 2.9.

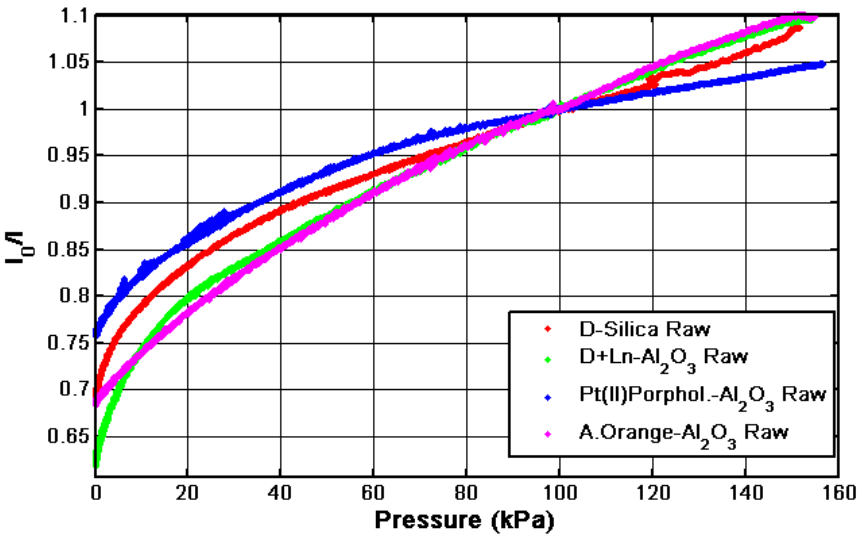


**Figure 2.9. Stern-Volmer chart of several select samples of raw data across the full range of pressures achievable with the syringe chamber**

Since the pressure region around atmospheric is the main focus for eventual wind tunnel application, the processed data from the approximately linear region of the Stern-Volmer plot, between 80kPa and 120kPa were fitted with a linear regression. The slope of the linear regression was used as a comparable measure of pressure sensitivity with regards to the various other sample combinations. An example of the fitted plots from the same samples as in Figure 2.9 is shown in Figure 2.10. The data acquisition was repeated for different samples and the averages of the regression slopes are reported in the summary Table 2.2. The A and B dye samples on aluminum oxide and zinc oxide particles provided quality regression slope values when compared to the calcium carbonate. Zinc oxide provides a unique attribute regarding an emission at 385nm when excited by a shorter wavelength source (i.e. 355nm laser). This emission at 385nm can be absorbed by some of the pressure dyes to provide stronger signal, especially the A and B dye which share a strong absorption peak around 390nm. Furthermore, aluminum oxide proved to be a consistent particle for quality signal to noise. A test was conducted on polystyrene particles loaded with A-dye to compare with the recognized strong signal to noise and pressure sensitivity of the polystyrene particles[Error! Bookmark not defined.]. The ighest Stern-Volmer regression slope, second to the polystyrene test was the A-dye in aluminum oxide, which was just above 50% of the polystyrene slope.

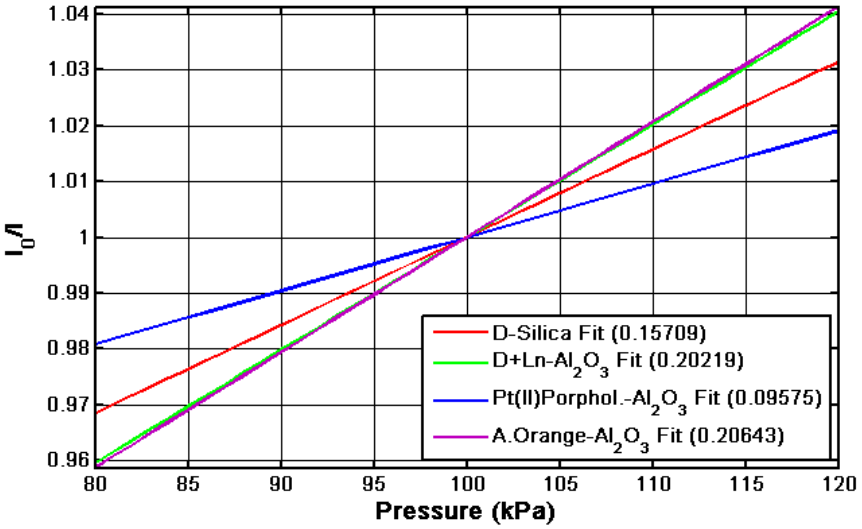


**Figure 2.10. Stern-Volmer chart of several select samples of fitted data, linear regression applied to the 80kPa to 120kPa range of raw data.**

**Table 2.2. Summary table of Stern-Volmer regression slopes (pressure sensitivity) for numerous tested pressure dye and particle combinations**

| Sample (Dye-Particle) | 80-120kPa Regression Slope | | |
|---|---|---|---|
| | Average [per kPa] | STD [per kPa] | (n) |
| Pt(II)Lactone-ZnO | 0.1380 | 0.0065 | (4) |
| A.Orange-ZnO | 0.0473 | 0.0069 | (4) |
| D+Ln-ZnO | 0.0645 | 0.0107 | (5) |
| Ruthenium-ZnO | 0.0552 | 0.0063 | (4) |
| B-$CaCO_3$ | 0.0772 | 0.0112 | (4) |
| B-ZnO | 0.3078 | 0.0376 | (4) |
| B-$Al_2O_3$ | 0.1372 | 0.0106 | (4) |
| A-$Al_2O_3$ | 0.4108 | 0.0250 | (4) |
| A-$CaCO_3$ | 0.1149 | 0.0078 | (4) |
| B-$CaCO_3$ | 0.0765 | 0.0040 | (4) |
| B-ZnO | 0.1650 | 0.0262 | (6) |
| A-Silica | 0.1221 | 0.0236 | (3) |
| B-$Al_2O_3$ | 0.1950 | 0.0019 | (2) |
| B-Silica | 0.0990 | 0.0107 | (2) |
| A-Polystyrene | 0.8133 | N/A | (1) |
| D-Silica | 0.1571 | N/A | (1) |
| D+Ln-$Al_2O_3$ | 0.2022 | N/A | (1) |
| Pt(II)Porphol.-$Al_2O_3$ | 0.0958 | N/A | (1) |
| A.Orange-$Al_2O_3$ | 0.2064 | N/A | (1) |

The response times of the dye and particle combinations with sufficient signal to noise and pressure sensitivity (i.e. Stern-Volmer regression slopes) were tested with the shock tube as in the silica particle testing, but again with the new aluminum foil diaphragm and vacuum air tank. The response times of those samples with quality shock tube results are presented in the summary Table 2.3.

**Table 2.3. Summary table of response times for pressure dye and particle combinations with both sufficient signal and pressure sensitivity**

| Sample (Dye-Particle) | Response Time (sec) |
|---|---|
| D-Silica | 1.75m |
| D+Ln-$Al_2O_3$ | 35µ |
| Pt(II)Porphol.-$Al_2O_3$ | 50µ |
| A.Orange-$Al_2O_3$ | 45µ |
| B-ZnO | 100's µ |
| A-$Al_2O_3$ | 50µ |
| A-Silica | 70µ |
| B-$Al_2O_3$ | 55µ |
| B-Silica | 80µ |

The results of the new particle and pressure-dye testing indicated that the aluminum oxide particle ($Al_2O_3$) provided consistently fast response times and the A or B dye offered the best pressure sensitivity according to the Stern-Volmer linear regression slopes. The silica particle still maintained response times on the order of microseconds, however, the aluminum oxide particle proved to be more beneficial to the pressure sensitivity. Figure 2.11 presents the samples with the quality pressure sensitivity and response time results comparing aluminum oxide to the previous used polystyrene and silica particle and comparing the selected A and B dye for further testing. The zinc oxide particles proved to be very difficult in response times testing as the particles tended to blow away as the shock wave passed over them. The response time of the zinc oxide particle loaded with B dye was obtainable but resulted in response times on the order of a 100’s of microseconds. Further testing of the zinc oxide particle is necessary so that the 385nm emissions benefit can be used for future testing with lower wavelength excitation sources (i.e. 355nm pulsed laser). The Pt(II)Porphol, D+Ln, and A.Orange dyes also proved to be potential candidates for pressure-sensitivity with both sufficient pressure response and response times, when loaded onto aluminum oxide particles. Finally, the aluminum oxide particle with A dye

was selected as the candidate for dual dye loading and progression toward testing with a 532nm pulsed laser source.

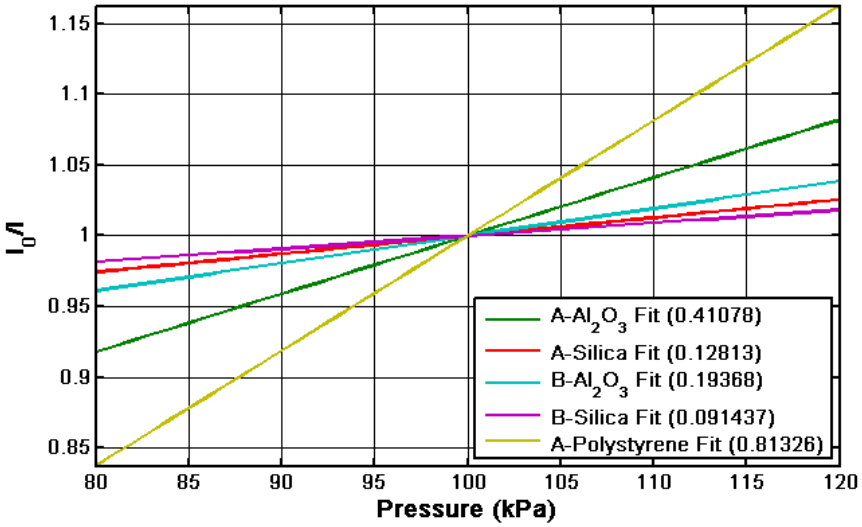


**Figure 2.11. Stern-Volmer of fitted 80-120kPa data comparing A and B dye loaded to aluminum oxide, silica, and polystyrene particles.**

# Chapter 3. EVOLVING SIMULTANEOUS VELOCITY & PRESSURE TECHNIQUE

## *3.1. Wind Tunnel Application Theory*

With the development of a fast responding microbead for eventual wind tunnel testing, the calibration techniques for pressure measurements needed to be investigated. Since the new microbeads had lower pressure sensitive and overall luminescence, the polystyrene microbeads were used to study the calibration process. The polystyrene microbeads possessed higher signal-to-noise and were already fabricated for use in this research. They presented an excellent testing option to develop the pressure measurement techniques in parallel to the new microbead manufacturing and characterization. These polystyrene microbeads were applied to glass slides for initial characterization and stationary calibration before being applied to an aerosolized experiment in order to fully understand the limitations of the test system and behavior of the microbeads.

### *3.1.1. Surface Paint Theory*

In wind tunnel applications, PSP is coated onto a surface of a model and then run through a series of calibration processes. The images are used to develop the calibration curve generally called the Stern-Volmer curve.[24] In order to account for spatial variations the images are normalized to a wind-off image, usually atmospheric. Furthermore, image registration is used to appropriately match pixels for the ratioing when model movement and deformations occur during the tunnel testing. Recently multi-luminophor paints have been used to further account for spatial variations. Khalil *et al*.[24] used a dual-luminophor paint with a pressure-sensitive dye and a temperature sensitive dye as a reference. The TSP helped correct for the temperature variations in the PSP coating. The experimental setup for this study is presented in Figure 3.1, where a two-camera setup was used to image both luminescent dyes. However, the two cameras were offset at different angles, which required image registration to correct for the different field of view. The surface PSP provided the fundamentals for a theoretical adaptation of the pressure-sensitive dyes on microbeads.

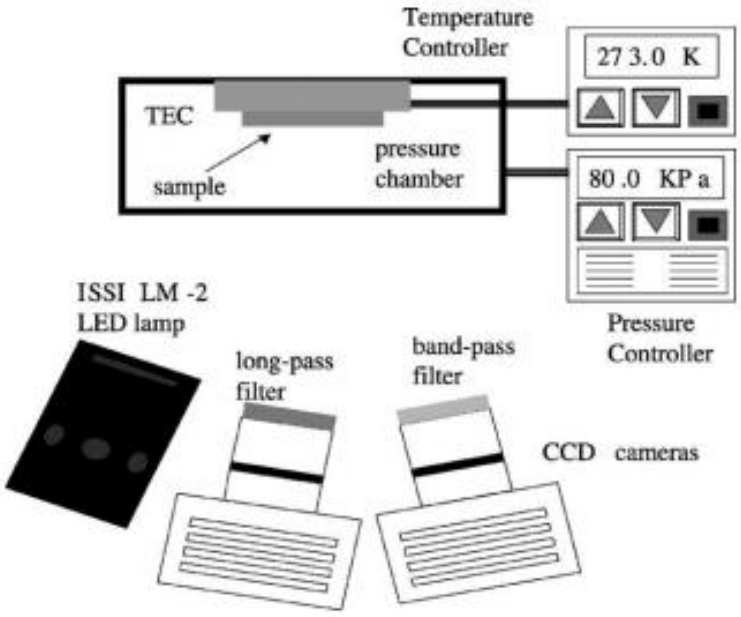


**Figure 3.1. Dual-luminophor pressure sensitive paint experimental setup.**[24]

### *3.1.2. Aerosolized PTSBeads Theory*

With the eventual progression from surface PSP experiments to flow field measurements of pressure, temperature, and velocity, a three-camera system would be required. Unlike surface experiments which have the benefit of stationary experimental models, measuring the flow field properties at specific instances requires simultaneous imaging of the pressure, temperature, and reference signals. As an example, if one image was captured for pressure measurement and then the reference and temperature images were captured at a different point in time, then the flow field properties would have changed, significantly if under turbulent conditions. Therefore, the relationship between the pressure and temperature would be meaningless. It is possible to simply have the three different cameras positioned next to each other and pointed at the same area, and then correct the images with image registration and image transformations. However, this is not desired as it relies too heavily on software and interpolation methods to correct the images. In order to avoid these challenges, the best method for simultaneous imaging involves splitting the light with 45 degree beam splitters, dichroics, or polarizers. Dichroic filters present the best choice for maximizing the light as they separate the light by wavelength rather than polarity. That is, rather than splitting all the wavelengths of emitted light 50% each way, like a polarizer, and having to filter out the other wavelengths before each camera, the dichroic filters can split all the light of a particular wavelength. Figure 3.2 illustrates the implementation of these dichroics

in the theoretical setup for a three camera system with the three separate emissions wavelengths for each of the luminescent dyes.

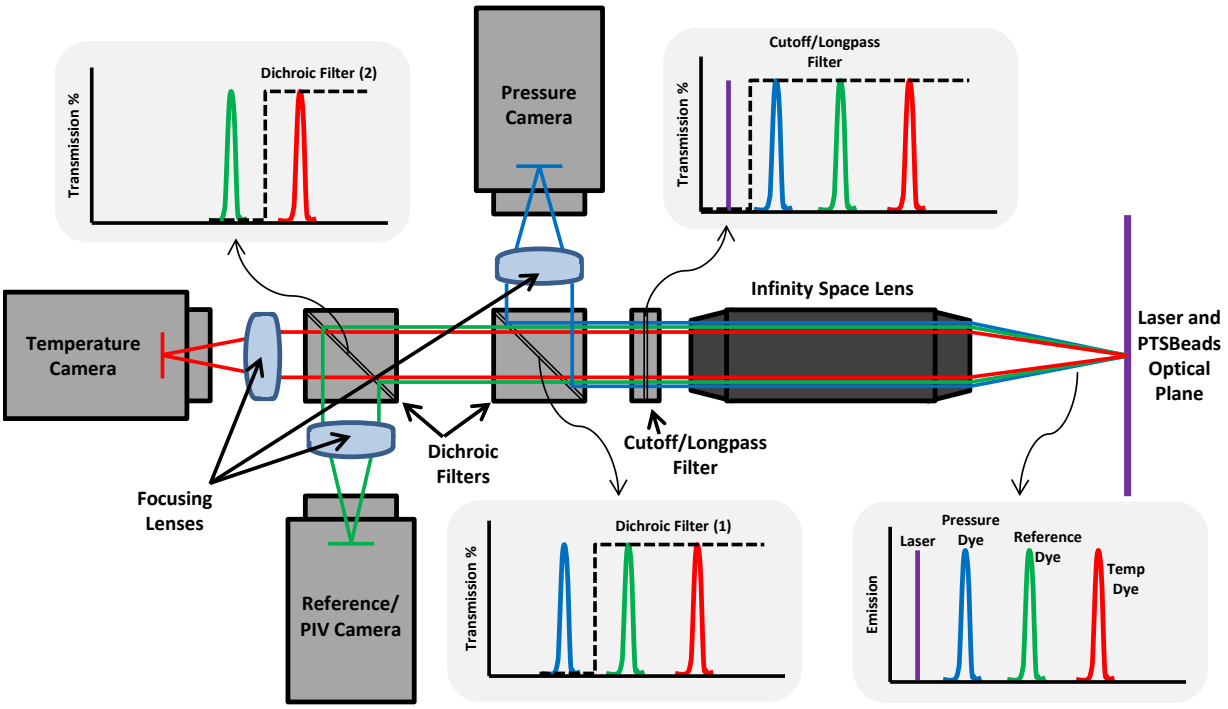


**Figure 3.2. Theoretical setup of 3-camera system for simultaneous pressure, temperature, and velocity.**

In this ideal setup, the laser reflections and emissions peaks would be distinctly divided so that the filters would separate the wavelengths appropriately for each camera. The light from the imaging plane would first transform into infinity space, thereby having parallel rays pass through the filters and optical components before being focused onto the digital camera chips. The first filter in the series would consist of a cutoff filter to block the laser light from reaching the rest of the setup, as seen in Figure 3.2, but still maintain a high transmittance for the rest of the emissions. The first dichroic would reflect the low wavelength luminescent emission and transmit the other two emissions, again with a high transmittance and reflection percentages. In Figure 3.2, this reflected emission is arbitrarily illustrated as the pressure dye emission, shown in blue. Finally, the second dichroic would separate the second and third emissions to their respective cameras, shown as the reference (green) and temperature (red) emissions in this setup. The correct application of the infinity space is crucial in this case to avoid problems with only using a single focusing lens, which would require equidistant cameras. Although this particular setup maximizes the light and avoids software-based image corrections, camera alignment becomes an incredibly challenging and tedious process.

This three camera setup would offer simultaneous pressure, temperature, and reference images, but the velocity calculations require standard PIV[19] methods to be performed on two successive frames with a short difference in time. For this reason, the camera sensitivity is often a tradeoff against frame rate. Since the reference intensity is insensitive to the conditions of the other dyes, it represents the obvious choice for PIV processing. Therefore, the reference camera is the only camera that requires the faster frame rate to capture two consecutive images with a short time difference. As discussed previously, PIV involves a double pulsed laser light source with short pulse widths, within a few nanoseconds, and the pulse separation dictated by the flow velocity. For faster flowing particles, the difference in time between the two laser pulses must obviously be reduced so that the movement between the two frames is in the pixel range for the desired spatial resolution. With higher sensitivity cameras on the pressure and temperature side the readout time is generally significantly longer than the PIV camera. In order to avoid the second pulse from occurring during the readout, the pressure and temperature frames need to be exposed after the first laser pulse as seen in the timing diagram in Figure 3.3.

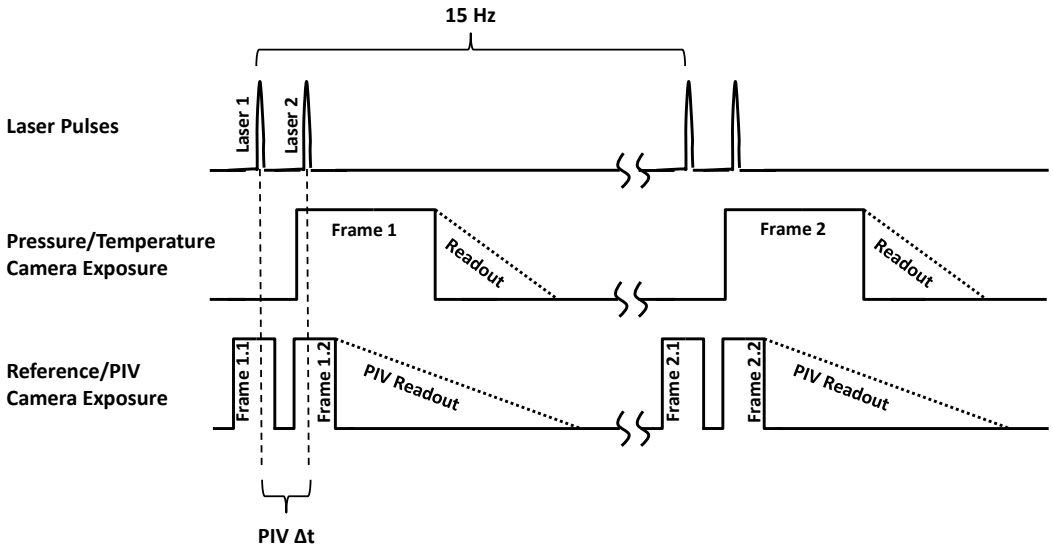


**Figure 3.3. Simultaneous pressure, temperature, and velocity, theoretical timing diagram.**

In this theoretical timing diagram, a double pulsed laser with a standard 15Hz repetition rate would excite the three different luminescent dyes. The PIV camera would capture the reference image frames for both pulses while the pressure and temperature cameras would capture only on the second pulse. As indicated in Figure 3.3, velocity would be calculated from

the two PIV/reference camera frames and the pressure and temperature would be determined from the pressure and temperature images and reference image corresponding to the same laser pulse. The aerosolized particles would act like PIV tracer particles, thus allowing for standard PIV methods and cross correlation techniques to determine the velocity vectors at each interrogation window.

Just as PIV breaks down images into interrogation windows, the pressure and temperature images would be processed using these interrogation windows. Pure pixel by pixel processing would be ideal, however, in practice this become less feasible because of slight misalignment, sub-pixel differences between the images, and even the case of using cameras with different sized pixels, where the imaging area of a pixel would change. In the case of using different sized pixels, the images can be divided into interrogations windows so that the windows between the different images are representative of the same imaging area, as outlined in equation (1). As an example, a PIV camera with 5µm-by-5µm pixels can be processed with 2pixel-by-2pixel interrogation windows and matched to a pressure camera with 12.5µm-by-12.5µm pixels using 5pixel-by-5pixel interrogation windows. In addition to ideally avoiding slight registration errors and better image area matching, the use of interrogation windows on the pressure and temperature processing allows for consistency in the spatial resolution of the pressure and temperature to that of the PIV calculated velocity vectors.

$$\frac{Camera\ 1\ Pixel\ Size}{Camera\ 2\ Pixel\ Size} = \frac{Interrogation\ Window\ Size\ Camera\ 2}{Interrogation\ Window\ Size\ Camera\ 1} \tag{1}$$

$$\text{Example: } \frac{5\mu m}{12.5\mu m} = \frac{2pixels}{5pixels}, or\ \frac{4pixels}{10pixels}, or\ \frac{16pixels}{40pixels}, etc$$

With each of the three images, pressure, temperature, and reference, separated into smaller interrogation windows for processing, the primary method implemented with the intensity values is the ratio-metric method, just as in the surface PSP experiments. The concept behind this method is to again simply ratio the different intensities for each interrogation window to determine the pressure and temperature fields. As the temperature luminophor provides a sensor insensitive to pressure the temperature to reference ratio will back out the temperature distribution. Consequently, as the pressure luminophor is sensitive to both pressure and temperature, the ratio-metric combination of all three intensities must be used to determine pressures, with the correction for temperature. With the aerosolized particles moving freely

through the flow field, background subtraction and different thresholding of pixels are implemented to better ratio the pressure and temperature intensities. Ignoring background subtraction may introduce significant error in the ratio data since the background signal can saturate the desired signal. It is obvious to subtract the particular camera base noise level but additional background from the experimental setup may be beneficial in further improving the signal to noise. Equation (2) presents how the ratio is calculated with background subtraction, where the camera noise level is subtracted in addition to any other background, such as the laser firing into an empty experimental testing chamber with no PTSBeads.

$$\frac{I_{sensor} - Background_{camera\ noise} - Background_{other}}{I_{reference} - Background_{camera\ noise} - Background_{other}} \quad (2)$$

In this flow field sense, ideally each of the aerosolized particles would emit with the same ratio of sensor, whether that was temperature or pressure, to reference, with the background and noise removed, for constant conditions. In other words, for uniform temperature and pressure, the ratio of the pressure emissions or temperature emissions to the reference emissions would remain constant. Therefore, a series of initial calibration images would suffice for determining a calibration curve to back out pressure and a curve to back out temperature. Imaging the aerosolized PTSBeads at constant pressure and varying uniform temperature and then constant temperature with varying uniform pressure would build the calibration curves. Obviously following this would be wind tunnel testing where the PTSBeads would respond to the flow and the simultaneous imaging would be used to back-calculate the pressure and temperature, in conjunction with the velocity from PIV. The fundamentals of this concept drove the investigation into this technique for an initial, two-camera setup which focused on pressure and velocity. Testing of this system began with stationary PTSBeads on slides before progressing to an aerosolized PTSBead experiment.

## *3.2. Experimental Setup & Methodology*

### *3.2.1. Stationary PTSBeads Experimentation*

The microbeads used in this experiment were polystyrene microbeads[22,36] with a mean diameter of 1.3μm. Two different sets of dyes were loaded onto the polystyrene particles. The first included A-dye as the pressure-sensitive dye, E-dye as the temperature-sensitive dye and H-

dye as the reference dye (AEH PTSBeads). The second consisted of A-dye as the pressure-sensitive dye, and silicon porphyrin (SiOEP) as the reference dye, with no temperature dye (A-SiOEP PSBeads). Again, the maximum emission wavelength is around 650nm for A-dye, 615nm for E-dye, 530nm for H-dye, and 580nm for SiOEP. Further detail on the microbead synthesis can be found in literature.[22,36] To obtain the spectral response of these microbeads, samples were placed onto a microscope slide. The experimental setup for acquiring spectral data from these slides is shown in Figure 3.4 and involved the same aluminum chamber as in the Stern-Volmer pressure sensitivity experiments.

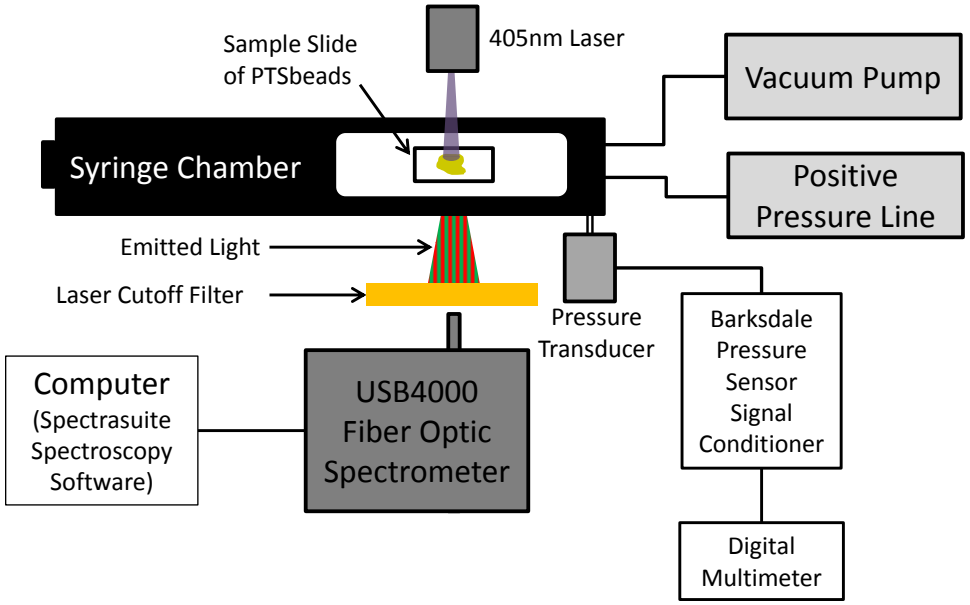


**Figure 3.4. Schematic of stationary PTSBeads in the test chamber with the spectrometer.**

For initial spectral characterization, two lasers were used as the light sources in conjugation with the two different microbeads. A continuous 405 nm wavelength diode pumped solid state (DPSS) laser directed at the sample was used as the excitation source for the AEH PTSbeads, and a 532nm laser pointer was used with the A-SiOEP PSBeads. The spectral behavior of these microbeads was determined with a miniature fiber optic spectrometer (USB4000, Ocean Optics, Dunedin, FL), and in turn, processed through the Spectrasuite Spectroscopy Software (Ocean Optics, Dunedin, FL). A simple color glass cutoff filter was positioned in front of the spectrometer to block the light from the light source but allow the dye emissions to pass through. A 450nm cutoff filter was used with the AEH PTSBeads to remove the 405nm laser light and a 550nm cutoff filter was used with the A-SiOEP PSBeads to remove the light from the 532nm laser pointer. The spectral response of a sample of polystyrene AEH

PTSBeads excited by the continuous 405nm wavelength laser is shown in Figure 3.5, with a pressure range from atmospheric to near-vacuum. It can be seen, that the emission intensity of the pressure sensitive dye is in fact a function of pressure (650 nm), while the reference intensity stays constant (530 nm) as has been previously reported by Kimura *et al.*[37] and the concept similarly demonstrated by Meier *et al.*[38] and Zhu *et al.*[36] Figure 3.5 also shows that the intensity change of the pressure-sensitive dye is not a linear function of pressure, as the Stern-Volmer plots also showed (New In-House Manufactured Particles). The spectral response of the A-SiOEP PSBeads excited by a 532nm laser is presented in Figure 3.6, however, with a pressure range from atmospheric to only 50kPa. Additionally, the spectral response of the A-SiOEP PSBeads excited by a 405nm laser is demonstrated in Figure 3.7 to better show the SiOEP emission. This experiment confirms that the dyes emit light in the expected wavelengths and verifies the proper spectral behaviors of these dyes within microbeads as has been previously reported.[36-37]

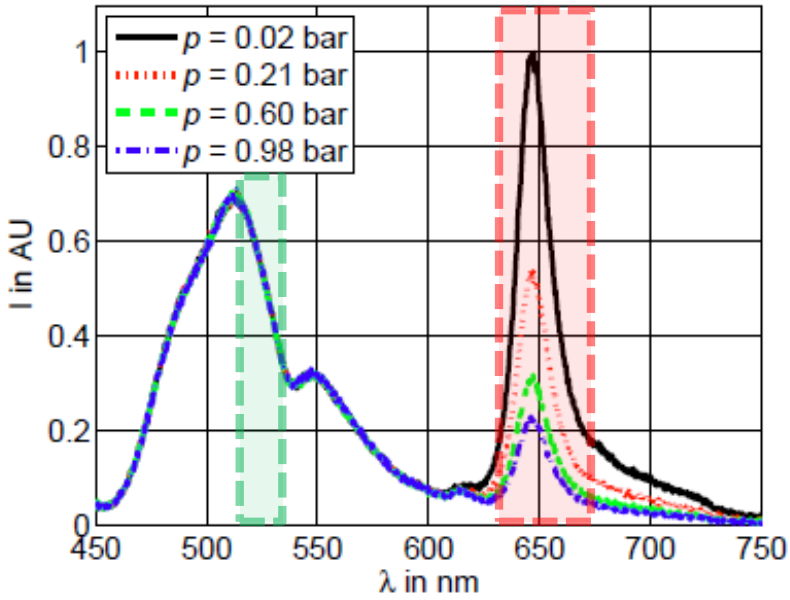


**Figure 3.5. Fluorescent emission of a pressure and temperature sensitive PTSBead sample at constant temperature and varying pressure. (reference max: 530nm, pressure max: 650nm). Highlighted regions show the range of wavelengths associated with the bandpass filters used in the aerosolized testing.**

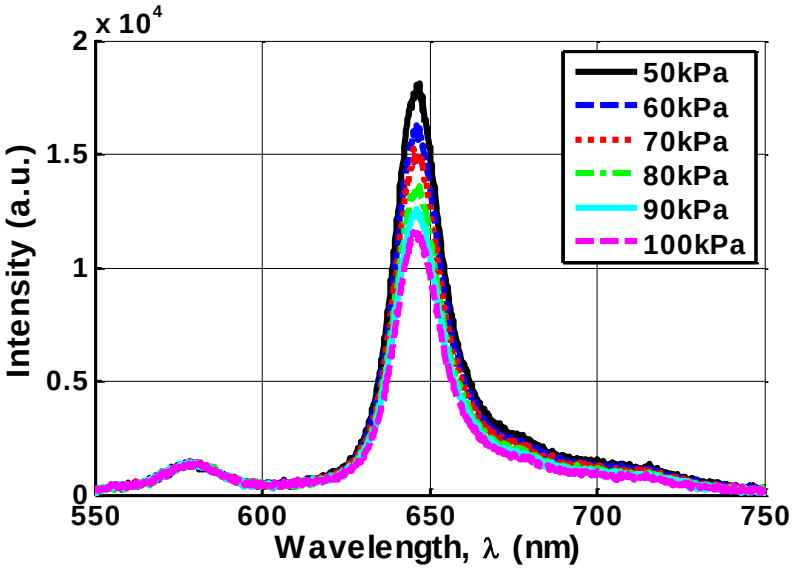


**Figure 3.6. Emission of the dual-luminophor polystyrene microbead at constant temperature and varying pressure, excited by a 532nm laser. Reference (SiOEP) peak: 580nm. Pressure (PtOEP) peak: 650nm.**

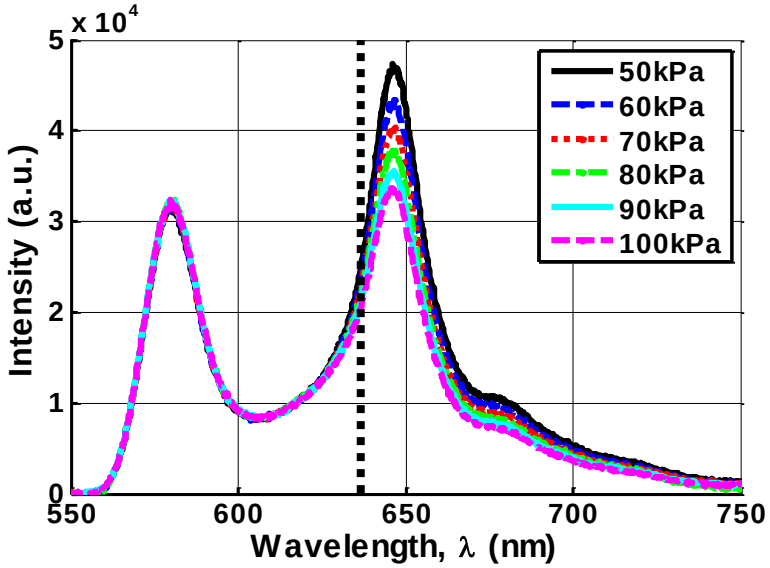


**Figure 3.7 Emission of the dual-luminophor polystyrene microbead at constant temperature and varying pressure, excited by a 405nm laser to better illustrate the reference peak. Reference (SiOEP) peak: 580nm. Pressure (PtOEP) peak: 650nm. (dashed line at 635nm representing chosen dichroic)**

The same pressure transducer from the pressure sensitivity tests was used to monitor the pressure throughout the experiments with the syringe chamber. The signal from this transducer was sent to a Barksdale pressure sensor signal conditioner and monitored with a digital multimeter. Since the signal conditioner was adapted for use with this pressure transducer, it was not necessary to perform a calibration before each experiment. The vacuum pump was again

used to reach pressures down to approximately 0kPa, however, for positive pressures above atmospheric, a positive air pressure line was used, as illustrated in Figure 3.4.

Since the spectrometer offered intensity measurements of the PTSBeads on a slide across the wide range of wavelengths, this setup was used for initial PTSBead characterizations. Along with the spectral response of the PTSBead samples for varying pressure, the intensity changes of the pressure and reference dyes were measured with respect to the changing laser power. This was to characterize the effect of different excitation intensity on each dye. Since the reference intensity emits based on the excitation intensity and is insensitive to pressure and temperature, it is analogous to the laser power. The response of the pressure and reference dyes for varying excitation intensity could therefore be analyzed by simply comparing the ratio of pressure to reference against varying reference intensities. With the PTSBeads sample in the chamber the pressure was varied from atmospheric to near-vacuum and at each pressure, the laser power was varied to create ratio vs. reference intensity curves. The pressure in the chamber was varied between approximately 10kpa and 100kpa in increments of 10kpa. The spectral data of the PTSBeads sample were recorded while manually changing the voltage to the laser after the pressure in the chamber was stabilized. The overall power of the laser was kept low as to not saturate the intensity determined from the spectrometer as well as to eliminate the possibility of photo-degradation.

The spectrometer presents a useful tool for characterization in the absence of spatial concerns. However, since the focus of this testing was to evolve the pressure measurements of 2-D fields using cameras, the setup of the stationary microbeads was tested under a two-camera system. Unlike the spectrometer's acquisition of single location intensities, digital cameras allow for intensity measurement across a certain field of view. The digital camera, however, measures the light integrated across the wide range of wavelengths rather than distinguishing the different wavelengths. Similar to the description of the theoretical three-camera system (Aerosolized PTSBeads Theory) a two-camera system for pressure measurement was implemented. A CCD camera (Hamamatsu CCD camera, model C9100-13, 512 x 512), was used to image the pressure sensitive luminophor. Alternatively, a sCMOS camera (PCO edge 4.2, 2048 x 2048) was used to image the reference dye. These two cameras simultaneously imaged the slide sample of microbeads through the front window of the test section using a 45deg. dichroic filter/beamsplitter. The dichroic and optical filters were chosen based on the microbead sample.

For the AEH PTSBeads testing a 45deg. red dichroic filter (Edmund Optics 35mm Square 45 Deg. Red Dichroic Filter, 49-471) was used. A bandpass filter was attached to the front of each camera, allowing only the wavelength of the pressure or reference dye's luminescent light to pass and blocking the laser and temperature dye emission. The filter on the reference camera was a 527nm fluorescence bandpass with a 20nm bandpass (Edmund Optics 527nm Bandpass Filter, 20nm Bandpass, OD6 Blocking, 25mm Dia, 84-098) while the filter on the pressure camera was a 655nm fluorescence bandpass with a 40nm bandpass (Edmund Optics 655nm Bandpass Filter, 40nm Bandpass, OD6 Blocking, 25mm Dia, 67-037). The bandpass filters are illustrated in the highlighted region of the spectral plot, Figure 3.5. Furthermore, Figure 3.8 shows the normalized emission of the different dyes in reference to the laser as well as the selected bandpass filters and dichroic mirror used to separate the bands to each camera. Note that the H-dye bandpass filter only took a small range of green light and the A-dye bandpass filter cutoff the emission passed approximately 675nm, both of which did not maximize the luminescence signal. However, the H-dye reference signal and A-dye pressure signal were sufficiently high with the 405nm laser and loaded on the polystyrene PTSBeads. The primary purpose of the bandpass filters in this case was to block both the laser and unwanted dye emission given the imperfect transmittance and reflectance of the dichroic filter.

The continuous 405nm wavelength laser was again used as an excitation source for the AEH PTSBeads and pulsed on and off at 10Hz with an output energy of 70mW. The laser beam in conjunction with cylindrical lenses created a two-dimensional sheet of light, just as in PIV, that passed through the top and bottom quartz windows and through the glass slide of PSBeads. The laser sheet was aligned slightly off parallel to the glass slide sample to maximize the sheets illumination of the PSBeads. The experimental schematic of the testing of stationary AEH PTSBeads is illustrated in Figure 3.9.

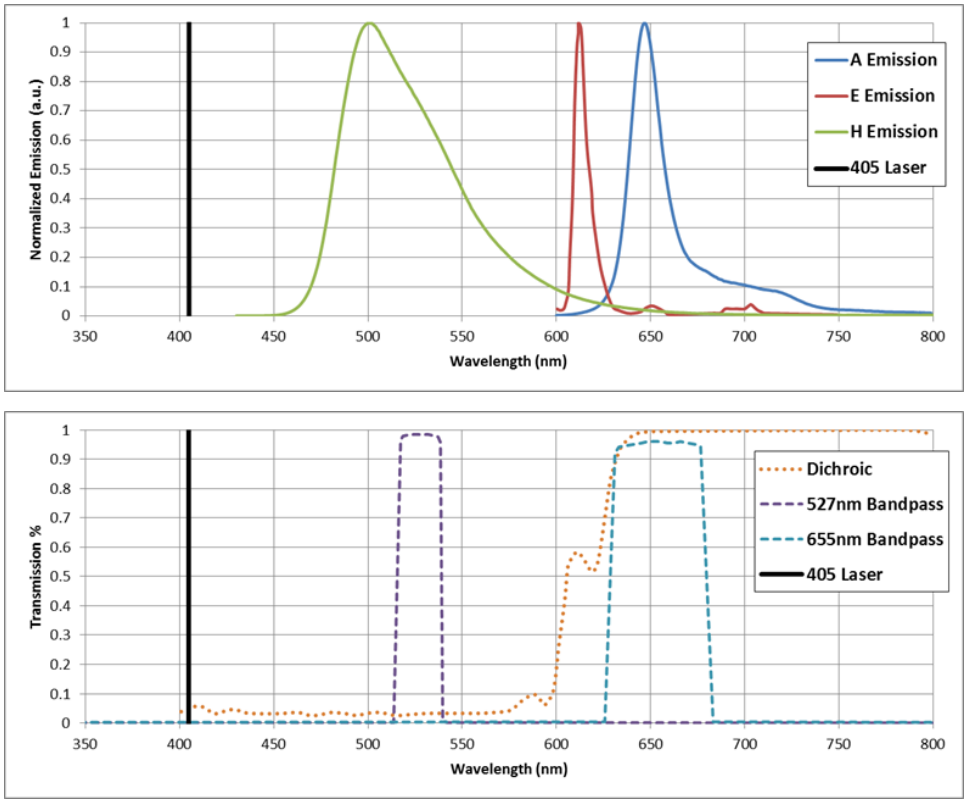


**Figure 3.8. Normalized Emissions for A, E, and H dyes (top) and optical filters and dichroic transmittance for two-camera setup with 405nm laser excitation source (bottom).**

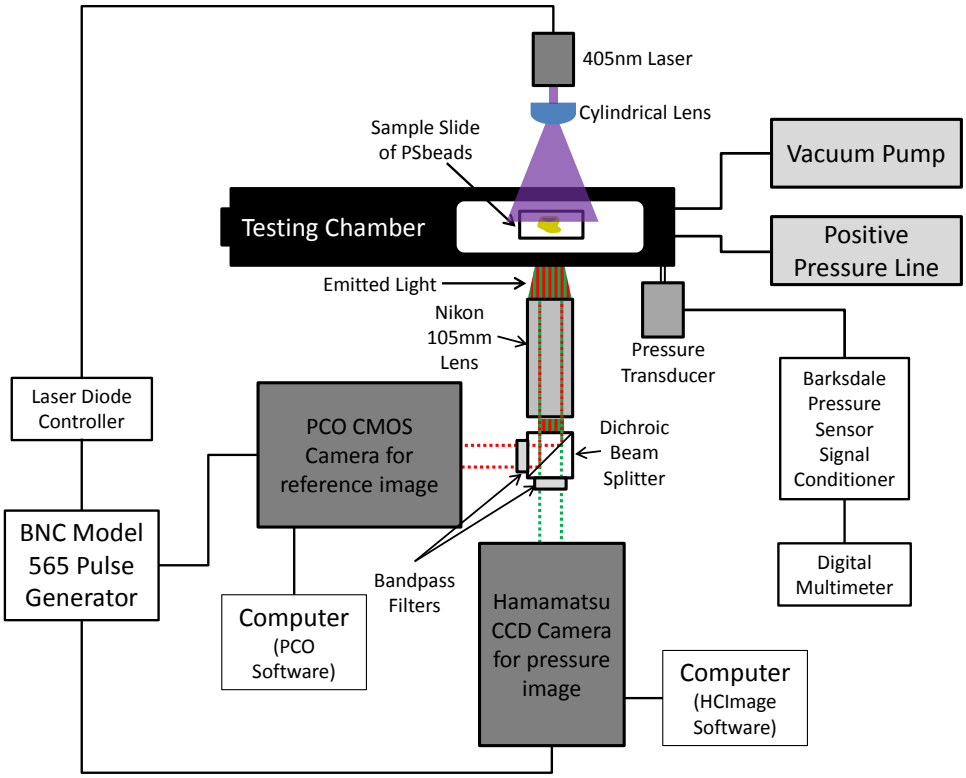


**Figure 3.9. Experimental schematic of two-camera setup for stationary multi-luminophor AEH microbeads on a slide, excited by a 405nm laser.**

The A-SiOEP PSBeads testing with a 532nm laser consisted of different optical filters, with the same intention of blocking the laser and separating the luminescent light of the pressure and reference dyes. The normalized emissions and optical filters used in reference to the 532nm laser are presented in Figure 3.10. Rather than using two bandpass filters between the cameras and dichroic filter, a high quality fluorescence 550nm cutoff filter (Edmund Optics 550nm High Performance Longpass Filter 25mm Dia, 62-984) was placed in front of the dichroic splitter, between the lens and dichroic. In this effort, the laser reflections were cutoff immediately rather than separately after the light passes through the dichroic cube. The dichroic filter was a 635nm edge filter (Shemrock 635nm edge BrightLine dichroic beamsplitter, FF635-Di01) and was selected to best separate the A and SiOEP emissions between the two cameras as illustrated in Figure 3.10. The dichroic allowed the wavelengths of light above 635nm to transmit straight through to the pressure camera while reflecting and turning the wavelengths below 635nm to the reference camera.

A pulsed 532nm wavelength dual Nd:YAG laser (New Wave Research, Solo PIV) was used as the excitation source for these PSBeads. 532nm laser line dichroic mirrors (Thorlabs,

NB1-J12) were used to steer the beam and direct it straight down through the middle of the chamber test section. The laser beam in conjunction with cylindrical lenses was again created into a two-dimensional light sheet as in AEH PTSBeads testing with the 405nm laser. The experimental schematic of the testing of stationary A-SiOEP PSBeads is illustrated in Figure 3.11.

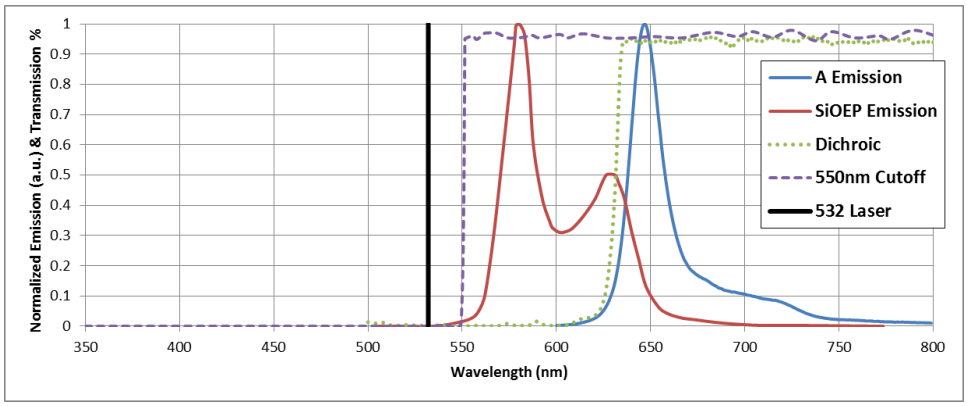


**Figure 3.10. Normalized Emissions for A and SiOEP dyes and 550nm cutoff filter and dichroic mirror for 532nm pulsed laser excitation source.**

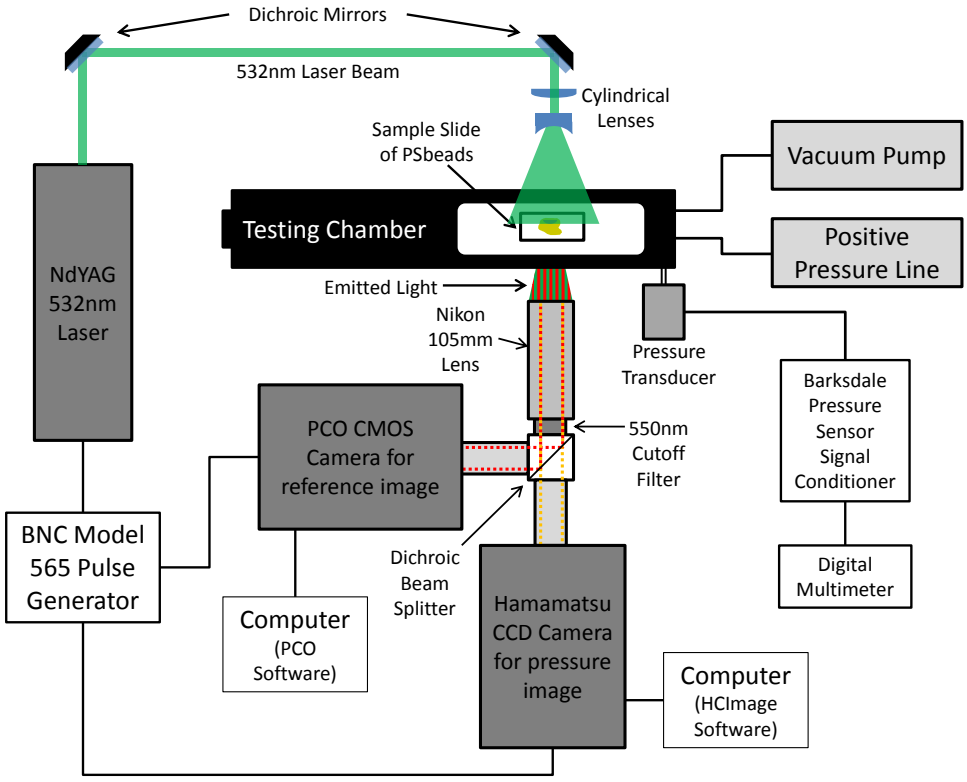


**Figure 3.11. Experimental schematic of two-camera setup for stationary dual-luminophor A-SiOEP microbeads on a slide, excited by a 532nm laser.**

The cameras and optical filters were used in conjunction with a Nikon 105mm lens, resulting in a field of view of approximately 0.65 x 0.65 cm². Although the theoretical system would make use of infinity space for alignment and focusing this system avoided this with the two cameras only needing to be equidistant to the dichroic. Alignment between the two cameras was achievable with translation stages, rotation stages, and mounts.

The glass slide samples of microbeads for experimentation were secured inside the middle of the test section parallel to the front facing window. Special care was taken for distributing the microbeads on the slide in an even and uniform manner. The uniformity of surface pressure sensitive paints has become a crucial component for pressure measurements as previous research supports.[8,39] In previous experiments, determining pressures requires a wind-off reference image of each particular fluorescent dye wavelength to account for spatial, excitation, and coating variations. Most of these variations are accounted for using the reference dye and wind-off normalizing, however, variations can still persist and cause higher uncertainties.

Although the calibration process can account for different variations, reducing these variations prior to actual experimentation has been proven to improve the quality of the measurement techniques. Minimizing the variation in sample thickness has proved to be a key concept for accurate pressure measurement. Problems can arise from inconsistent thicknesses in the samples of surface paints caused by such things as self-quenching or absorption and emission interference between the luminophors.[6] Differences in thickness can be a particular problem for SiOEP, for example, since part of the emission around 580nm can be re-absorbed. To avoid these possible issues, uniform coating techniques of microbeads on glass slides were explored. Following a simplified version of coating technique performed by Prevo and Velev,[40] a thin, uniform layer was created on glass slides by first dropping a dilute solution of microbeads on a glass slide. Another glass slide was then used to carefully squeeze the microbeads solution into a uniform film as the solvent evaporated. This process is illustrated in Figure 3.12 below.

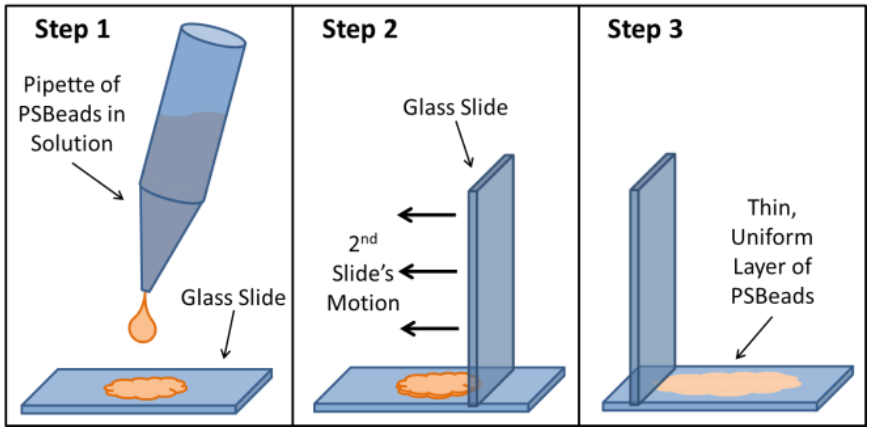


**Figure 3.12 Creating thin uniform slide samples of PSBeads for dual-luminophor image testing.**

With the uniform sample of microbeads secured in the chamber, the glass windows were sealed. The pressure was precisely controlled through a series of regulator valves and piping between the chamber valves and the vacuum pump and positive pressure line. Therefore small pressure changes could be generated and monitored in the chamber. The ability of the chamber to hold a particular pressure was verified by increasing and decreasing the pressure to the maximum and minimum levels and monitoring the pressure to ensure the chamber has no significant leaks.

A BNC model 565 pulse generator was used to synchronize the cameras exposures, and the pulsing of the laser when testing the A-SiOEP. The BNC was used as the master controller to make sure that the laser firing at 10Hz matched the image capturing. The cameras were operated by the Hamamatsu HCImage and PCO CamWare64 software, respectively. Both cameras were set in the external edge trigger mode, with an exposure time based off of the BNC's trigger signal and the time of the laser pulse. In this mode, the limiting factor for image capturing was the repetition rate of the laser. The AEH testing was set to 10Hz to be consistent although the 405nm laser diode was a continuous excitation source.

With the timing of each component established the chamber pressure was reduced to the minimum of 50kPa and then sealed by closing the valves along the vacuum pump and positive pressure lines. The appropriate gain and sensitivity settings of the cameras were determined to achieve the best signal-to-noise ratio and maximize the use of the pixel depth without pixel saturation. The pressure sensitive dye emits with higher intensities at lower pressures. Therefore, the pressure in the chamber was reduced to 50kPa before adjusting the camera settings. Furthermore, for the A-SiOEP testing, the highest laser energy of 260mJ was used by double

firing the PIV laser in a single exposure of the two cameras. For the AEH testing with the 405nm laser the laser diode was set to its maximum power as well via the laser diode controller.

To perform the pressure imaging tests, the laser illuminated the sample at each pressure increment from the 50kPa condition to 150kPa. For each pressure increment, 100 simultaneous pressure and reference images were captured. With the continuous 405nm laser and AEH PTSBeads, the laser was only turned on when the pressure had stabilized and the images were ready to be captured. When using the pulsed laser for the A-SiOEP tests, the 100 images were captured after the laser power had stabilized (approximately 100 pulses from start). The pressure was adjusted in increments of 10kPa until a total of 1100 images were captured for both pressure and reference cameras. Upon laser excitation, the microbeads will produce distinct emission wavelengths. The dyes have common absorption at the laser wavelength, however the absorptivity (extinction coefficient) of the dyes as well as the luminescence efficiency (quantum yield) are different. This dissimilarity can produce different relative emission intensities at lower laser power settings. This is created by a photon limited condition such that the total number of dye molecules in the microbead is larger than the laser photons available for excitation. The dependency of the intensities ratio of the pressure and reference emission bands as function of the laser energy was evaluated to determine the energy level for sufficient excitation. With constant camera settings the A-SiOEP testing was repeated for different laser energies: 130mJ achieved by only firing one laser in an exposure, and 65mJ and 35mJ, achieved by adjusting the laser's Flashlamp to Q-Switch delay.[41]

Afterwards, 100 background images were taken with the same camera sensitivity settings. The entire sequence of pressure images, reference images, and background images for both cameras were processed in order to establish the calibration techniques for a highly accurate, precise, and robust method for pressure measurements from these microbeads.

Regarding the spectral characterization of the PTSBeads, the intensity ratios of the emitted light ($R=I_p/I_{ref}$) were calculated from the spectrums captured with the spectrometer. For each pressure, the spectrum was captured at different reference intensities, by varying the reference laser power levels. To calculate the intensity ratios for each of the spectrum, the intensity values between 517 nm and 537 nm, and 635 and 675 nm were integrated (see highlighted regions in Figure 3.5), since each of these ranges corresponded to the bandpass filter range used to image the reference and pressure luminescence, respectively (see Figure 3.8).

Prior to the intensity integration, however, the spectrometer background signal baseline was subtracted and the spectrum noise was smoothed out using a weighted moving mean filter. The ratio of the resulting two integrated intensity values was then calculated for each pressure, at different reference intensities. The data from the varying pressure testing at the stronger reference intensities were used to fit an exponential calibration curve (2-D calibration).[3] The ratios, normalized with respect to the atmospheric ratios ($R/R_0$), were fitted using a dual-exponential fit in MATLAB, given by equation (3) below, where $p$ is the pressure:

$$\frac{R}{R_0} = a \cdot e^{(b \cdot p)} + c \cdot e^{(d \cdot p)}, \tag{3}$$

The set of data from the slide stationary PTSBeads testing at varying pressures and reference intensities was also processed in a similar manner. The characterized ratio vs. reference intensity data were also fitted using dual-exponential fits in MATLAB, given by equation (4) below, with different coefficients for each pressure:

$$R = a \cdot e^{(b \cdot I_{ref})} + c \cdot e^{(d \cdot I_{ref})}, \tag{4}$$

These curves were used to determine a 3-dimensional surface fit that represented the calibration surface. From the given reference intensity and ratio data, the surface could be used to back-calculate pressure and account for photon deficiency in the polystyrene microbeads. The feasibility of this surface fitting from the spectrometer stationary PTSBeads testing was determined in order to apply such a method to the aerosolized PTSBeads testing in the situation of being photon-deficient. The benefit of the surface fitting to a single two-dimensional curve is that it takes into account the different variations of dye luminescence for varying excitation intensities. Therefore, this can be thought of as an extended calibration plot. The calibration techniques from the spectrometer results of the stationary PTSBeads act as a good reference of the behavior of particular samples but lacks in that it is a single-point method. In order to develop the calibration techniques, which account for spatial variations, the two-camera system processing presented the next stage of the experiment.

For determining pressures the images collected from the experiment are processed in MATLAB to define the calibration and then calculate pressures for the 2-D plane of microbeads. First, each series of 100 pressure and reference images were averaged in time. This temporal averaging served to reduce the effects of the laser fluctuations and some of the camera shot

noise. The set of 100 background images and 100 images captured at each pressure step were averaged for both the pressure camera and reference camera. The averaged background images were then subtracted from each of the new, averaged images, again for both pressure and reference images.

The different cameras presented a unique problem for the pressure and reference ratioing. As the Hamamatsu (pressure luminophor) camera had a 512 x 512 pixel CCD with 16μm (square) pixels and the PCO (reference luminophor) camera had a 2048 x 2048 pixel sCMOS with 6.5μm pixels, pure pixel ratioing was not possible. As discussed in Aerosolized PTSBeads Theory, the images are broken down into smaller interrogation windows which can be used to successfully match the intensities for the different pixel size images. The ratio of pixel sizes is used to indicate the dimensions of the interrogation windows between the pressure and reference images as outlined in Equation (1), so that the interrogation windows between the pressure and reference images are matching the same area of the viewing plane. The pixel size ratio as a fraction of two integers provides the interrogation window sizes. That is, the pixel ratio of 16/6.5 results in pressure image interrogation windows of 13 x 13 pixels and reference image interrogation windows of 32 x 32 pixels.

With 13 pixel interrogation windows in the pressure images, the full sized images were cropped to a multiple of 13: 507 x 507 pixels (39 x 39 interrogation windows). Consequently, the reference images were cropped to the same number of interrogation windows, corresponding to an image size of 1248 x 1248 pixels. The location of the reference image cropping was determined using image cross correlation techniques.

The preprocessed images were divided into these smaller interrogation windows where the pixel intensities were averaged to obtain intensity values, $I_p$ and $I_{ref}$, for each interrogation window, according to Equation (5). $I_p$ and $I_{ref}$ were defined as the arithmetic mean of the intensity values in each interrogation window ($k$th row and $l$th column) for each of the pressure and reference images ($n$ = number of pixels per row, $m$ = number of pixels per column). A standard cross-correlation method was also applied between the pressure and reference images to account for any misalignment in order to best match the pixels used in the interrogation windows for the later ratios.

$$\bar{I}(k,l) = \frac{1}{mn}\sum_{i=1}^{n}\sum_{j=1}^{m} I(i,j) \tag{5}$$

The intensity ratios of the emitted light ($R=I_p/I_{ref}$) were calculated for each interrogation window. With the intensity ratios across the interrogation windows and at different pressures, the ideal calibration technique would involve a simple curve that back-calculates pressure from the ratio values. However, this single calibration curve results in radical errors when back-calculating the pressure as the pressure and reference ratios for a constant pressure image are not equal.

As discussed earlier, the reference luminophor should theoretically account for all spatial variations and result in uniform ratios but it does not remove all variations due to differences in sample thickness and excitation source illumination. Therefore, a second ratio ($R/R_0$) is implemented that normalizes the pressure and reference ratio at a particular pressure to the pressure and reference ratio at a set condition, in this case atmospheric, as shown in Equation (6). This is known as the ratio-of-ratios and has been proven to account for the spatial variations.[8,24]

$$\frac{\frac{I_p}{I_{ref}}}{\frac{I_{p_{100kPa}}}{I_{ref_{100kPa}}}} = \frac{\frac{P}{Ref}}{\frac{P_0}{Ref_0}} = \frac{R}{R_0} \tag{6}$$

The ratio-of-ratio data across the entire area (all interrogation windows) for each pressure are generally used to determine the coefficients for a single calibration curve, Equation (7) (a, b, c, and d are coefficients). This curve is then used to back-calculate the pressures. The accuracy in pressure calculation and spread of the pressures, due to uncertainties and sources of errors still existent in the ratio-of-ratios values was evaluated. To further reduce the uncertainties in the pressure measurements and push the calibration technique to its maximum potential, calibration curves were determined at every interrogation window similar to pixel-by-pixel calibration curves demonstrated in Huang *et al.*[42] These curves were determined using MATLAB's curve fitting toolbox and the equation coefficients were stored for later back-calculations of pressures.

$$Pressure = a \cdot e^{\left(b\cdot\frac{R}{R_0}\right)} + c \cdot e^{\left(d\cdot\frac{R}{R_0}\right)}, \tag{7}$$

This processing was also performed without the use of the reference images since the pressure images normalized with the atmospheric condition and the use of calibration curves per

window takes care of most spatial variations. Without the use of the reference images, a purely pixel by pixel calibration curves could be performed. Pixel by pixel processing was adapted to compare with the interrogation window averaging although this is usually avoided because slight misalignment and sub-pixel shifting or vibrations can substantially influence the error. The quality of the data and calibration technique were analyzed based on the accuracy and standard deviation of the pressures in each processed image pair.

### *3.2.1. Aerosolized PTSBeads Experimentation*

With the established stationary microbeads techniques and processing methods, the next phase of testing could progress to aerosolized AEH PTSBeads. The experimental set up for the aerosolized beads is shown in Figure 3.13 and Figure 3.14. This setup included the syringe chamber, 405nm laser diode, and most of the other experimental equipment used in testing of the stationary PTSBeads on a glass slide. However, the reference camera was switched to another CCD camera (Hamamatsu CCD camera, model C9100-13, 512 x 512) to be consistent with the pressure camera for this particular study. The vacuum pump and positive pressure line were disconnected causing all pressure variations to be control via the syringe plunger alone. The valves at the end of the syringe chamber were then connected to the components required to aerosolize the PTSBeads. The PTSBeads in a solution of isopropyl alcohol were aerosolized using a medical nebulizer and pressurized air. The aerosolized solution then passed through a de-moisturizer, which seeded the air in the chamber with dry particles. The exit valve was connected to an air filter so that the particle filled air could escape during the pumping process but excess aerosolized PTSBeads did not leave the chamber and piping system. This method created a steady stream of PTSBeads passing through the chamber, which was maintained until the maximum possible density of PTSBeads inside the chamber was achieved. The chamber was then manually sealed by closing the inlet and outlet valves before changing the pressure with the syringe.

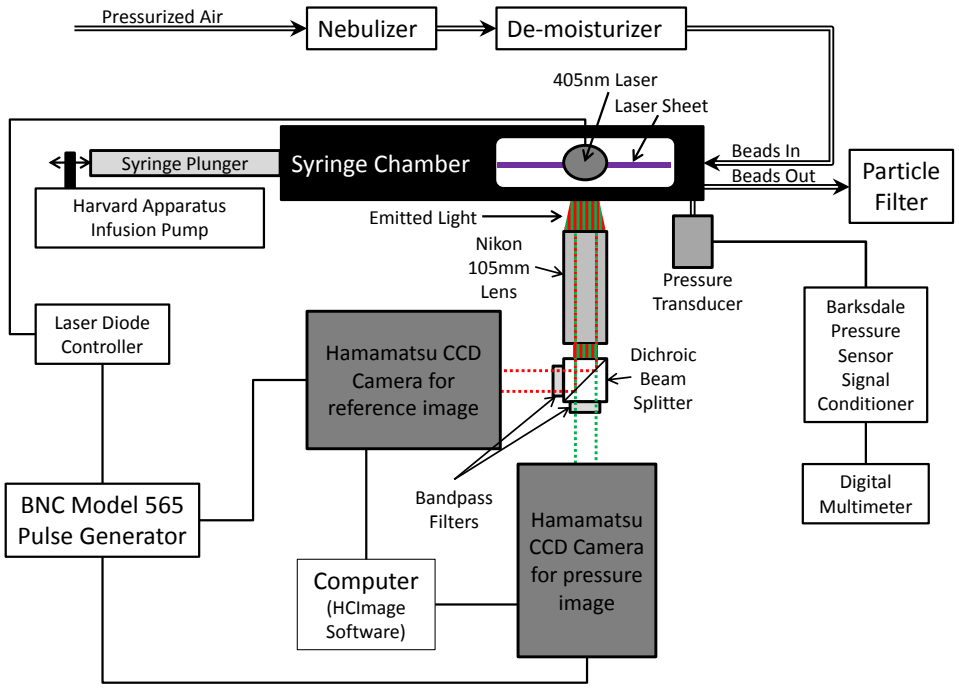


**Figure 3.13. Schematic of aerosolized PTSBeads experimental set up (top view).**

After pumping the PTSBeads in and sealing the chamber, the PTSBeads were allowed to settle in an aerosolized state, in order to avoid significant streaking due to the long exposure time and limited pulsing ability of the continuous laser. However, if too much time elapsed, the aerosolized particles would settle on the bottom of the chamber test section and the density of PTSBeads would be lost. This would result in a number of significant problems such as lower signal per pixel and PTSBeads covering the bottom glass window. With the PTSBeads settling on the bottom window, some laser light would scatter and reflect back up with a strong background signal from those excited PTSBeads from the bottom of the test section. Additionally, with the laser constantly hitting the layer of particles on the glass window the test chamber would heat up and demonstrate a strong convective flow motion of the particles, usually leading to upward motion streaking.

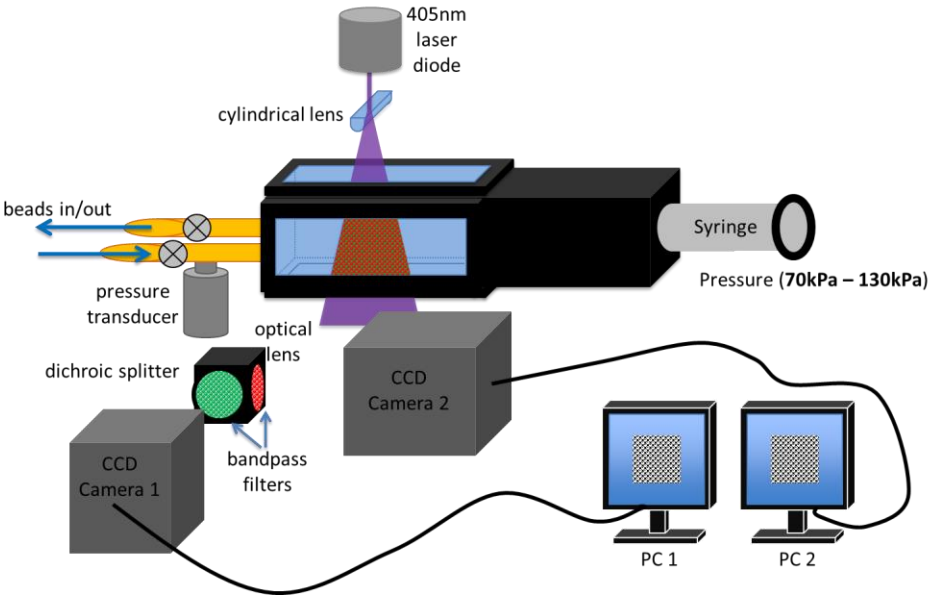


**Figure 3.14. Experimental setup of two camera system for aerosolized PTSBeads**

The 405 laser sheet was aligned vertically so that the illumination plane was parallel with the optical plane that the cameras imaged, as illustrated in Figure 3.14. Furthermore, the laser sheet was aligned horizontally so that the centerline of the beam passed through the center of the viewing area, since the laser sheet still possessed a Gaussian profile. With the cameras imaging the strongest part of the laser, for the highest signal-to-noise, the camera settings were adjusted to again maximize the pixel well depth.

After the gain and sensitivity gain were set at the lowest pressure condition, the chamber was returned to atmospheric pressure and 50 images were taken. The syringe was moved in until the next pressure step was reached and another 50 images were taken. This procedure was repeated until the pressure of 130kPa (1.3bar) was reached. With the syringe plug pushed inside, the valves were opened, restoring atmospheric pressure in the chamber, and then resealed. The plug was then pulled out and at each pressure step from 100kPa (1bar) to 70kPa (0.7bar), 50 images were again captured, resulting in an overall number of 350 images. Afterwards, 50 background images were taken once the PTSBeads were cleared from the chamber at the particular sensitivity and gain settings, which were subtracted from the data images to account for noise. Finally, these data were also processed, based on the techniques and knowledge established with the stationary PTSBead testing, in order to obtain the calibration plots.

For each image pair (pressure and reference) the mean ratio was calculated using the arithmetic mean of the ratios in each interrogation window. The average ratios at each pressure

were normalized with respect to the average ratio of the atmospheric image and fitted using the same method as in the initial slide stationary PTSBeads testing, equation (3). In order to back-calculate the pressure of each interrogation window for each image pair, the ratios where again normalized to the average atmospheric ratio. The normalized ratios were then applied back into the Stern-Volmer calibration curve, equation (3), to determine pressures for each of the ratio values. Since the PTSBeads are aerosolized and constantly moving the ratio-of-ratios cannot be applied and therefore the spatial variations cannot be removed with the atmospheric condition. The calibration curves per window (or pixel) could not be performed since the windows (or pixels) do not maintain the same microbeads, removing another option for spatial variation accounting. Nonetheless, the calibration curve and standard deviations of the ratios in the images were analyzed for varying interrogation window sizes. In addition, several threshold methods were also applied to exclude pixels in the interrogation windows below certain intensities. Furthermore, for the calibration process a series of cutoff studies were conducted to remove interrogation windows that produced low signal-to-noise.

Along with the single calibration curve, an extended calibration surface method was investigated for the aerosolized PTSBeads processing. The ratios of $I_p/I_{ref}$ at each interrogation window were plotted against the respective reference intensity values for each pressure to account for the varying excitation intensity, as in the spectrometer stationary PTSBeads data processing. This was necessary because although the laser was formed into a thin sheet, it still maintained its Gaussian-like profile, creating a spatially varying light sheet and photon-deficient conditions for the PTSBeads. The data from the images were fitted to dual-exponential curves using the same MATLAB fitting tool as the spectrometer stationary PTSBeads surface fitting, (4). The fitted exponential curves were used to generate data points along the full range of reference intensities and assigned their respective pressures as the third dimension. With the range of reference intensities, the ratios from the fitted curves and the corresponding pressures, a surface was calculated using the MATLAB fitting toolbox. Once this calibration surface was defined, the reference intensity and ratio for each interrogation window were inputted into the surface equation to back-calculate pressure. The quality of the data and calibration surface were analyzed based on the accuracy and standard deviation of the pressures in each image pair.

## *3.3. Result*

### *3.3.1. Stationary PTSBeads*

Initial tests were performed to characterize the ratio-of-ratios across a large pressure range with a spectrometer. These tests revealed that calibration curve has a dual exponential trend, as seen in Figure 3.15, unlike the usual Stern-Volmer linear estimation used for simplicity.[35] The data in Figure 3.15 shows that the decay is strictly non-linear with a much higher sensitivity in the low pressure region and follows the dual-exponential model with coefficients annotated on the chart. A similar behavior was already shown by Kimura *et al.*,[21] which confirms that the intensity ratio method is feasible for capturing pressure changes using these PTSBeads.

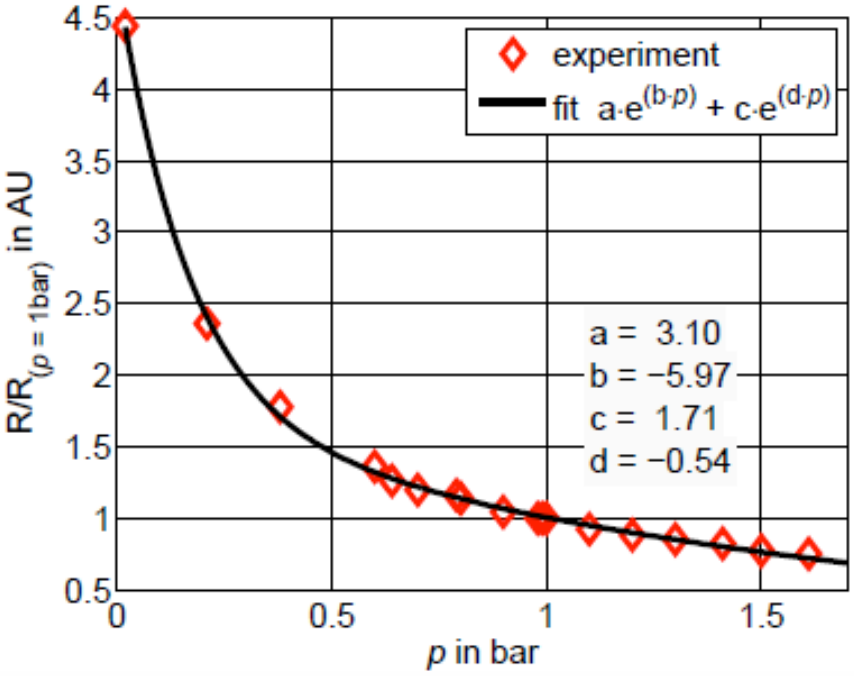


**Figure 3.15 Normalized ratios of emission intensity of the pressure and reference-dye for varying pressure from the stationary PTSBeads tests. The data are normalized with the atmospheric data.**

Following the procedure described in Stationary PTSBeads Experimentation, to characterize the behavior of the AEH PTSBeads with the spectrometer, the intensity ratios versus pressure were plotted and shown in Figure 3.16. This figure shows a plot of the intensity ratio as a function of the reference intensity, where the curves are fitted to exponential decays. The changes of the ratio values are much more evident at the lower laser power and more pronounced

at the lower pressure values. The plot illustrates the non-linear behavior of the ratio as a function of increasing reference intensities.

An extended calibration surface was generated using a surface fitting toolbox in MATLAB (a 43-polynomial, 4 degrees in the x-axis, reference intensity; 3 degrees in the y-axis, intensity ratio) and calculated as the best match to the curves. The surface and exponential fitted curves are shown in Figure 3.17. Given the values of the reference intensity and calculated ratio, the calibration surface estimated the pressure of the stationary microbeads slide samples accurately to within 1kpa. The calibration methodology used to obtain the calibration curve was also used to determine the calibration surface. As the stationary PTSBeads offers an easily controlled experiment, it represents an excellent method for testing microbeads with various reference intensities for varying pressures. With this understanding, we pursue an imaging-based calibration method that would incorporate a dual-exponential calibration procedure.

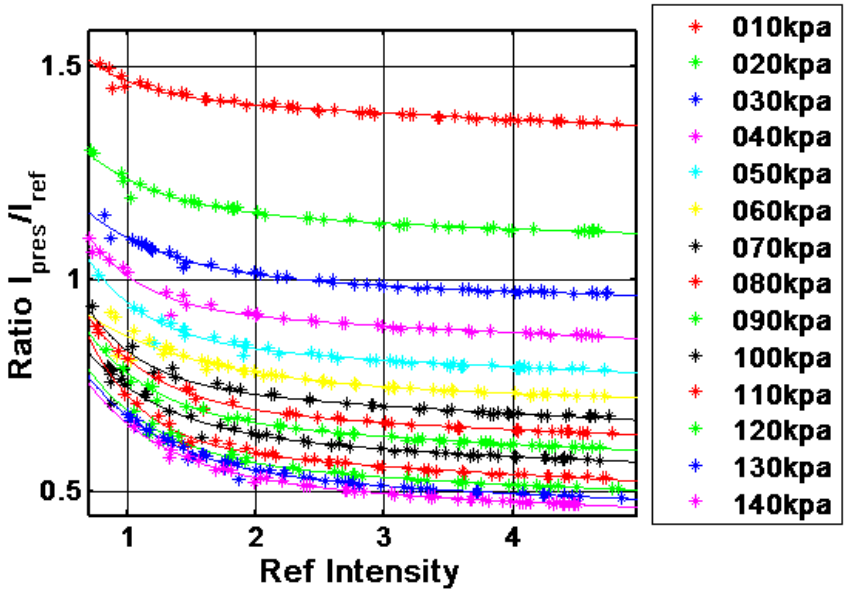


**Figure 3.16 Plots of the ratios vs. reference intensities as a function of pressure.**

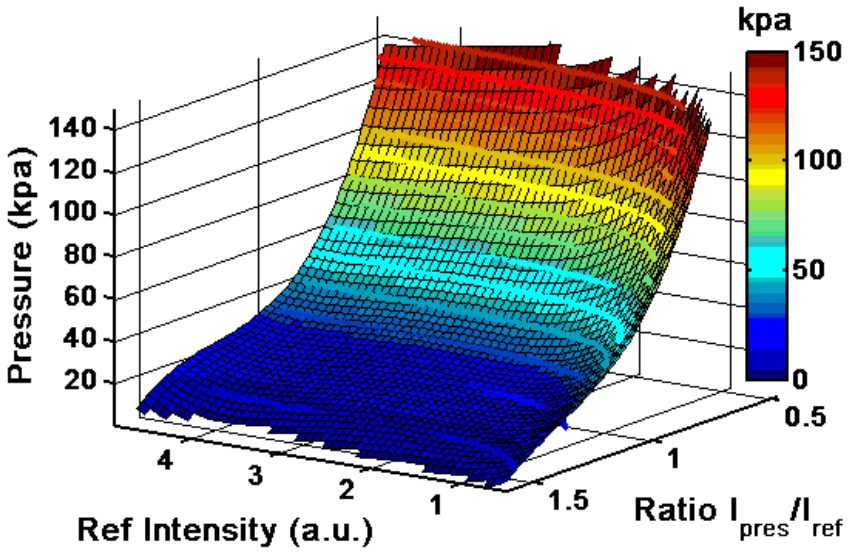


**Figure 3.17 Calibration surface and individual exponential curve fits from the raw stationary PTSBeads data (z and color axes are pressure).**

The slide samples of polystyrene microbeads were tested with the digital cameras, also using ratio-metric methods. The processing code for the stationary sample ratioing and pressure calculations was established to determine pressures from the series of calibration images. Efforts to best match existing pressure-sensitive paint results were taken through a number of different samples and processing techniques. Wind-off referencing (referencing images to an image at a selected pressure) proved to be the most effective method in reducing the standard deviation of the calculated pressures. Furthermore, individual calibration curves (pixel by pixel or window by window) provided much more accurate pressure calculations as well as lower full field pressure standard deviations.

An example image of an AEH PTSBeads slide test is shown in Figure 3.18. This particular test was processed without the reference images but still applying the atmospheric normalizing. With just the pressure images of these stationary PTSBeads, the calibration process was conducted for pixel by pixel and varying interrogation window sizes in order to quantify the effects of the interrogation window pixel averaging. The AEH PTSBeads test processed for 16 x 16 interrogation windows and individual calibration curves per window is provided in Figure 3.19. Figure 3.19 presents the back-calculated pressure for the entire field of view across the pressure range from 70kPa to 130kPa. The calibration processing for this case resulted in accurate pressures with an average standard deviation in the pressures of 167Pa. Since the pressure in the chamber is theoretically constant when the calibration images are captured, back-

calculated pressures should be uniform across the image. The slight differences in the back-calculated pressures are uncertainties in the system and calibration techniques.

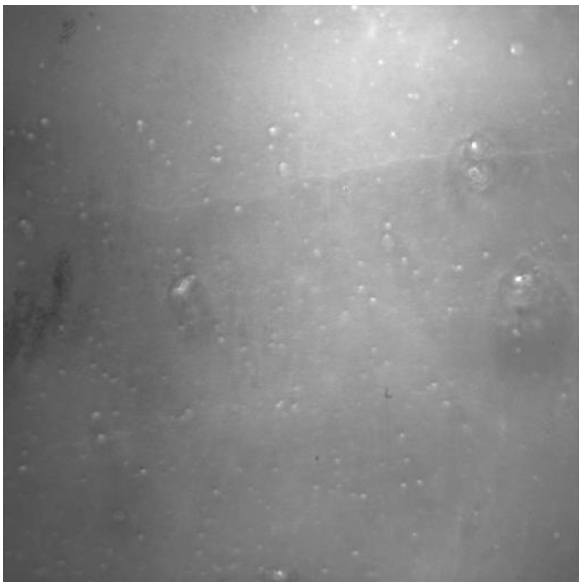

**Figure 3.18. Pressure image of slide sample of AEH PTSBeads at 70kPa**

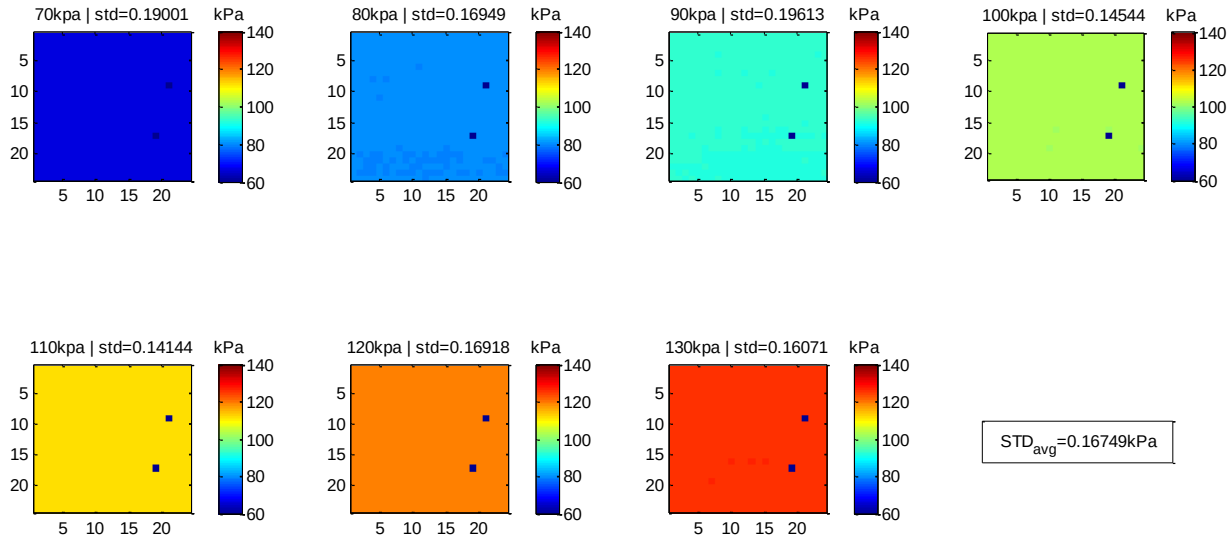


**Figure 3.19. Slide sample test of AEH PTSBeads with images processed without reference images for 16 x 16 pixel interrogation windows (dark blue represents removed saturated pixels)**

The average standard deviations of back-calculated pressures from the AEH PTSBeads stationary slide testing are summarized below in Table 3.1. The calibration processes were performed without the references images in order to compare different sized interrogation windows. The spatial variations were mostly accounted for with the ratio of the pressure images

against the atmospheric image. In Table 3.1, pixel by pixel processing was performed on the AEH PTSBeads test with strong 405nm laser power. The different sized interrogation windows, 64 x 64, 32 x 32, 16 x 16, and 8 x 8, were performed on both the strong excitation and low excitation power. As the interrogation windows are a spatial averaging the larger the windows the more the standard deviations in the back-calculated pressures are reduced. However, with larger interrogation windows the spatial resolution decreases. Additionally the order of processing was switched so that the interrogation window averaging was performed after the image ratioing and showed that there was no difference in the pressure calculations. The single calibration curve processing was also presented. The results proved that the additional calibration curves decrease the standard deviations of pressures since the more curves in turn takes care of the remaining spatial variations. Finally, the lower excitation source power generally resulted in higher pressure uncertainties, as expected because of the lower signal-to-noise ratios.

**Table 3.1. Average standard deviations for AEH PTSBeads testing with different interrogation window sizes (excluding reference images) and calibration techniques.**

| | | | **Interrogation Window Size (pixels x pixels)** | | | | |
|---|---|---|---|---|---|---|---|
| | | | **64x64** | **32x32** | **16x16** | **8x8** | **1x1** |
| **AEH PTSBeads w/ Strong Excitation Power (**Figure 3.18**)** | **averaging across windows, then ratioing** | **Single Calibration Curve** | 0.461 kPa | 0.499 kPa | 0.532 kPa | 0.607 kPa | 1.844 kPa |
| | | **Calibration Curve per window** | 0.140 kPa | 0.149 kPa | 0.167 kPa | 0.213 kPa | 1.007 kPa |
| | **pixel by pixel ratioing, then window averaging** | **Single Calibration Curve** | 0.463 kPa | 0.500 kPa | 0.532 kPa | 0.606 kPa | N/A |
| | | **Calibration Curve per window** | 0.140 kPa | 0.149 kPa | 0.167 kPa | 0.213 kPa | N/A |
| **AEH PTSBeads w/ Low Excitation Power** | **averaging across windows, then ratioing** | **Single Calibration Curve** | 0.678 kPa | 0.720 kPa | 0.768 kPa | 0.900 kPa | N/A |
| | | **Calibration Curve per window** | 0.092 kPa | 0.112 kPa | 0.160 kPa | 0.262 kPa | N/A |

Figure 6 below, presents a pair of A-SiOEP PSBeads images at 100kPa contrasted to better show the closely uniform distribution of particles.

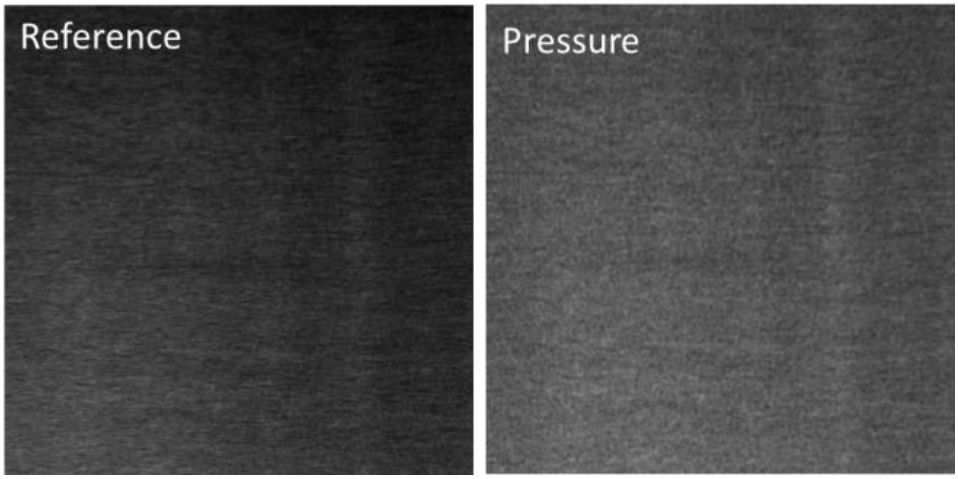


**Figure 3.20 A pair of scaled and contrasted images of A-SiOEP PSBeads, reference (left) and pressure (right), at 100kPa.**

Initial processing of these images revealed that the reference images had a slight dependency on the pressure although they should remain constant, since the reference dye is insensitive to pressure changes. This phenomenon was discovered to be the result of the optical equipment chosen. It can be seen in Figure 3.10 that the dichroic transmits the pressure dye's emission from 635nm and up and therefore, reflects the emissions from 550nm (lower wavelengths cutoff by the longpass filter) to 635nm. Furthermore, the emission from the A has a tail end that extends slightly below the 635nm chosen separation wavelength. The SiOEP emission of these PSBeads from a 532nm light source is substantially low compared to the A emission, as obviously seen in Figure 3.6 and Figure 3.7. Therefore, the tail of the A emission (below 635nm) is reflected along with the SiOEP and causes the pressure dependency in the reference images. In order to remove this dependency a simple spectral overlap correction was applied to the reference images. This correction is shown in Equation (8), where *X* is the percentage of the pressure intensity to be subtracted from the raw reference intensity, and *k* and *l* are the interrogation window indices. The percentage of pressure intensity to subtract was determined empirically and was generally around 0.9%.

$$I_{ref_{cor}}(k,l) = I_{ref}(k,l) - X\% * I_p(k,l) \tag{8}$$

From these corrected images, the processing was performed on individual interrogation windows to generate the calibration curves per window. Figure 3.21 presents an example of three

interrogation window calibration curves. Note that Figure 3.21 presents the pressure on the vertical axis with the ratio values on the horizontal axis, contrary to Figure 3.15 and the conventional Stern-Volmer plot.[35] This was chosen based on the calibration curve fitting so that the pressure calculations can be quickly determined from the ratios. This shows the necessity for individual calibration curves in further accounting for slight variations from a single, averaged calibration curve on the ratio-of-ratios.

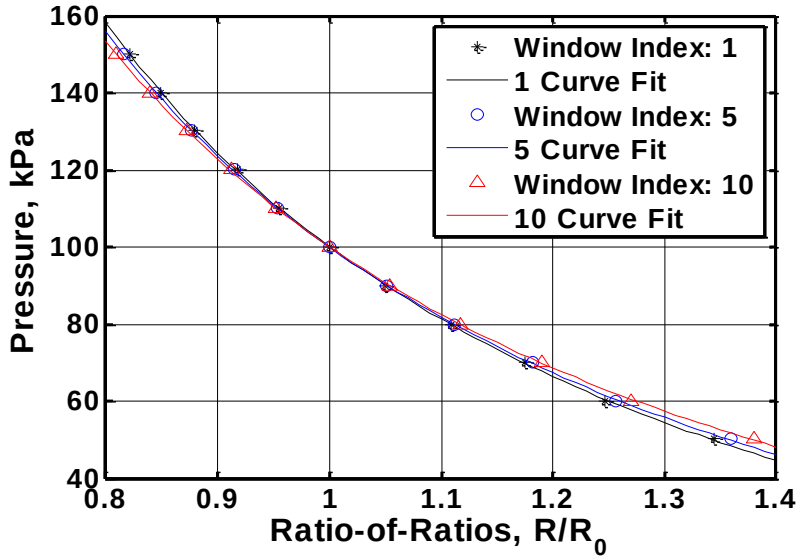


**Figure 3.21 Example of three arbitrarily chosen interrogation window calibration curves from the A-SiOEP PSBeads tests showing the slight variation between window locations.**

With the calibration curves calculated for each interrogation window the processed images were used to back-calculate the pressures in order to determine the quality of this calibration process. With the processing involving the use of interrogation windows and the pixel averaging in these windows, the spatial resolution was dependent on the interrogation window size. In this particular setup the 0.65 x 0.65 $cm^2$ field of view and selected interrogation window sizes resulted in a spatial resolution of 165µm x 165µm. Pressures could be resolved every 165µm x 165µm (each interrogation window).

In PIV, the velocity field of the investigated flow is obtained by dividing the acquired images into smaller interrogation windows and calculating the average particle displacement and thus determining one velocity vector for each window. Since the eventual processing technique will involve aerosolized particles and combining pressure measurement with velocity, this method of image sectioning was investigated. The motivation for developing the pressure

measurement techniques and the different camera matching compelled the use of interrogation windows.

This calibration technique resulted in highly accurate pressures with significantly low deviations from the measured pressure, from the test chamber pressure transducer.
The precision of the calibration was determined by finding the standard deviation, σ, of the pressure calculations across the processed images (each interrogation window). A perfect set of data would result in uniform pressures with no deviations at the constant pressure steps from 50kPa to 150kPa since the pressure in the chamber was constant for each image sequence. The standard deviations at each pressure were averaged for the varying laser energy test sets. The results of these deviations are presented in Table 3.2, where the two columns of calibration methods are the ratio-of-ratios (right column) as described in this paper and the processing performed without the reference images (left column). The wind-off referencing and calibration curves per window allow for the pressure measurement with the single A-dye images, since spatial variations are account for. Table 3.2 shows however, that including the reference emissions improves the pressure measurements for the different laser energies as has been previously reported in Khalil *et al*.[24] In the case of the highest laser energy level, however, the reference emissions do not improve the precision of the pressure measurements. This is possibly attributed to the calibration technique reaching its maximum potential for this particular experiment and the error sources that come from combining the images. In an aerosolized application, the reference dye is crucial to account for the spatial variations since the microbeads are constantly moving around in the imaging field of view.

**Table 3.2. Average standard deviation of back-calculated pressures (in Pa) from A-SiOEP PSBeads testing for different laser pulse energies (in mJ) and calibration method (including and excluding reference-luminophor images).**

| | **Calibration Method Pressure Standard Deviation, σ** | |
|---|---|---|
| **Laser Pulse Energy** | $P/P_0$ | $\left(P/Ref\right)/\left(P_0/Ref_0\right)$ |
| **260mJ** | 74 Pa | 106 Pa |
| **130mJ** | 137 Pa | 111 Pa |
| **65mJ** | 159 Pa | 128 Pa |
| **38mJ** | 278 Pa | 181 Pa |

The standard deviation obviously decreases with increasing laser energy because of the higher signal-to-noise. With the lowest energy level of 38mJ, this pressure calibration technique was still able to accurately back-calculate the pressures, with an average standard deviation of 181Pa. The highest laser energy of 260mJ (double pulsing) resulted in a ratio-of-ratios calibration standard deviation of 106Pa. The back-calculated pressures for this particular case are presented in Figure 3.22, which illustrates the uniformity of pressure measurements. Additionally, the single calibration curve back-calculation of this particular case is shown in Figure 3.23, which shows the spatial variations still evident in the ratio-of-ratios. Clearly the calibration curves per window help account for the persistent spatial variations, when comparing the pressures from Figure 3.22 and Figure 3.23.

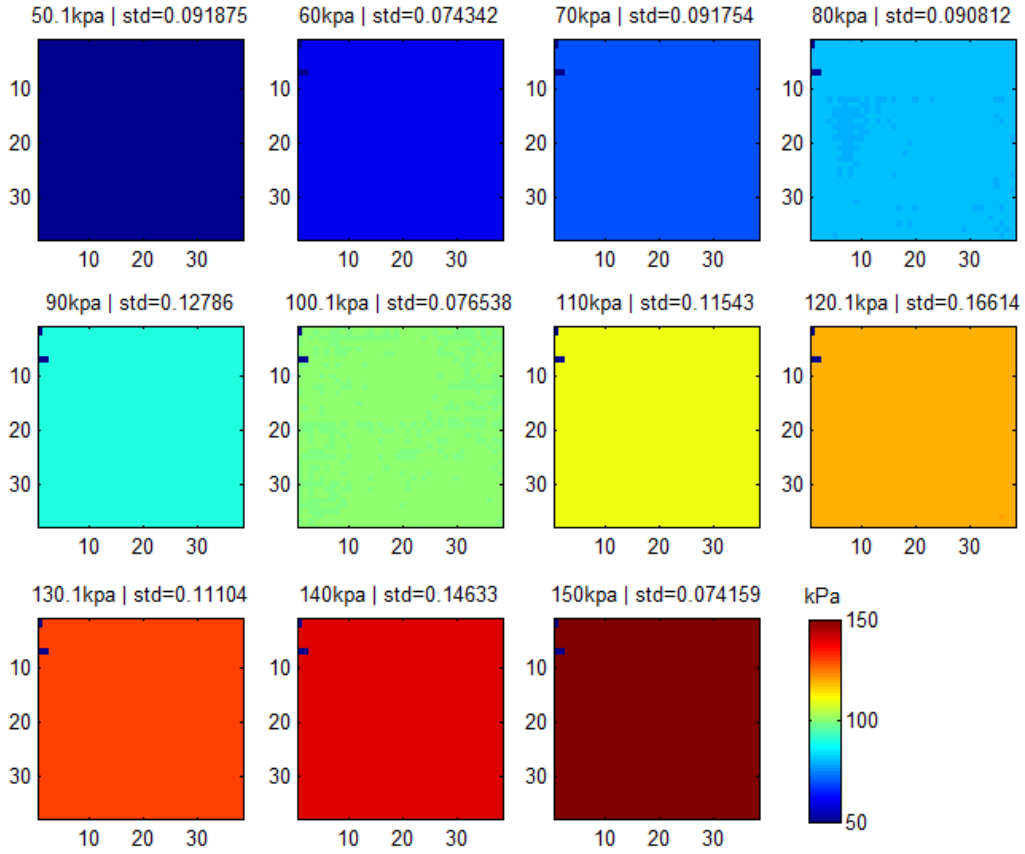


**Figure 3.22 Back-calculated pressure using a calibration curves for every window of stationary A-SiOEP PSBeads from constant pressure images.**

The average standard deviation of pressures for this calibration method is significantly below what has been previously reported. Kose *et al.*[26,27] reported an intensity-based approach with standard deviations from 414Pa to 830Pa, but reduced those in a principal component

analysis processing technique to 207Pa to 345Pa. Khalil *et al*.[24] reported pressure errors on the order of 414Pa with an image smoothing technique reducing that to 140Pa. Clearly the calibration curve per window technique demonstrates a new highly precise calibration process based on a ratio-metric method.

It is critical to understand and develop the calibration technique to its maximum potential so that the knowledge and experience can be applied to the calibration of aerosolized testing. Kimura *et al*.[21] and Abe *et al*.[20] demonstrated the use of aerosolized PSBeads for flow field pressure measurements but with significant uncertainty in the pressures. Through extensive testing the level of uncertainty in these pressure measurements with this calibration process is reaching its maximum potential. The persistent uncertainties ($10^2$Pa) could be from a number of different sources of error, including, but not limited to, camera shot noise proportional to the actual pixel counts, sub-pixel movement, spatial variations not removed by the calibration process, and even actual slight pressure variations in the test section.

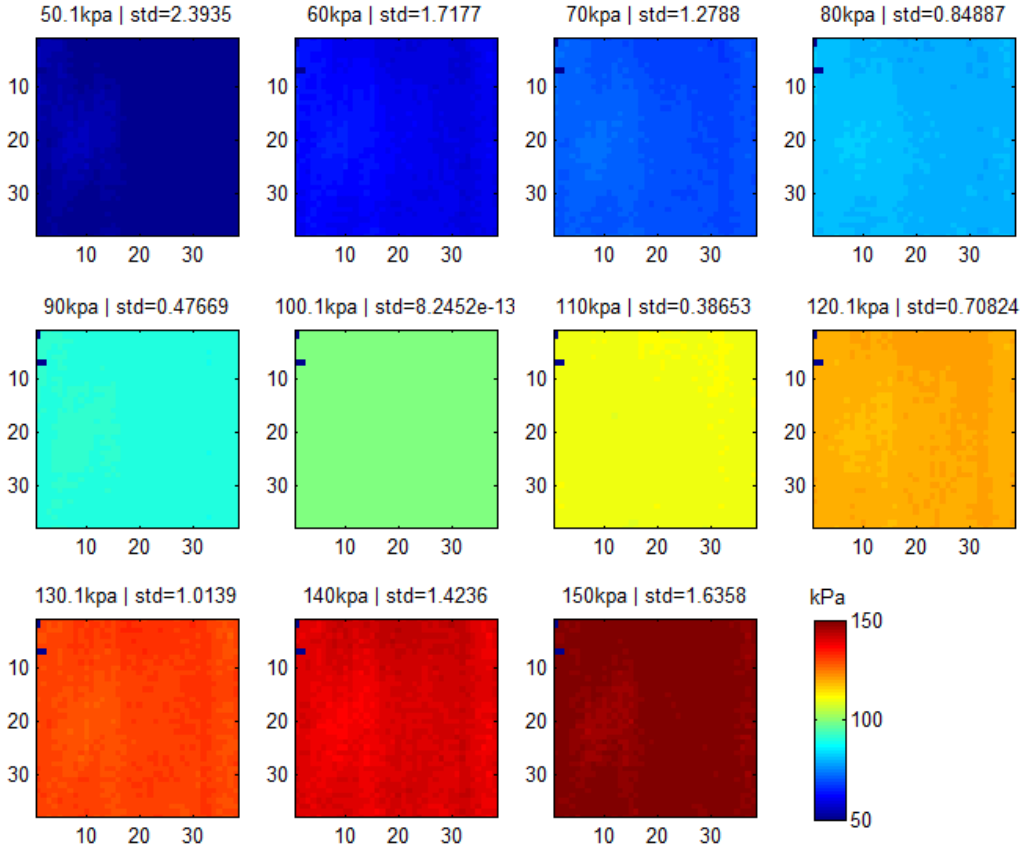


**Figure 3.23. Back-calculated pressure using a single calibration curve of stationary A-SiOEP PTSBeads from constant pressure images.**

### *3.3.2. Aerosolized PTSBeads*

Intensity measurements of airborne PTSBeads were obtained using a two camera system, where each of the cameras simultaneously and separately captured the pressure-sensitive PTSBead and the reference PTSBead images. Figure 3.24 presents a pair of raw images contrasted to better illustrate the high density of PTSBeads' existence in the chamber during the tests. The particles were subjected to a pressure range of 70-130kPa and 50 images were taken at each pressure step of 10kPa.

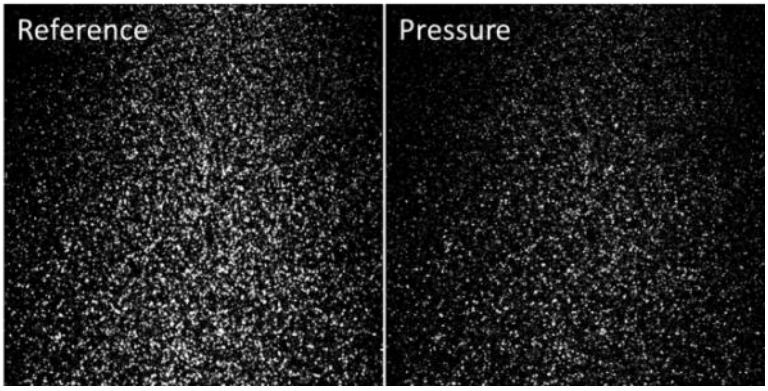


**Figure 3.24. A pair of raw images, reference (left) and pressure (right), at 70kPa, contrasted to make the PTSBeads more visible**

With the processed images and intensity ratios calculated, several studies were performed in order to properly calibrate the PTSBeads. The first of such studies involved processing the data with varying threshold intensities in the raw images (pixels below the threshold were ignored in interrogation window intensity averages). The interrogation windows were 16x16 pixels. Figure 3.25 shows this particular study and the distinct trend with regards to these thresholds.

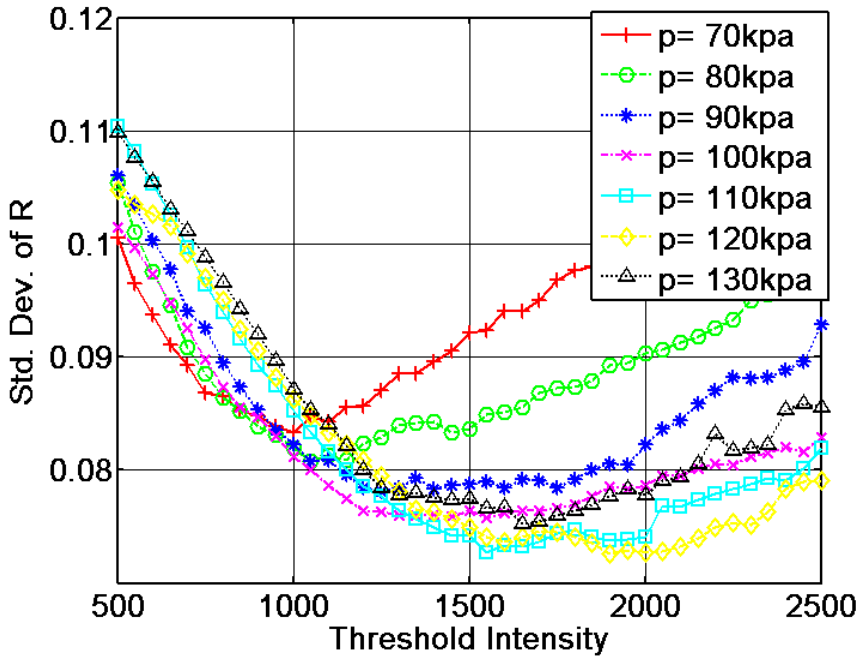


**Figure 3.25. Standard deviation of the ratios at each pressure for various processing threshold intensities.**

The chart clearly presents processing threshold intensities corresponding to minimum standard deviations. Additionally, these minimums appear to be shifting to higher threshold intensity values for higher pressures, while lowering the values of the minimums as well. However, when the minimum standard deviation thresholds were plotted against pressure, an alternative trend became apparent. Figure 3.26 shows the threshold intensities plotted against pressure for the reference image data (blue) and the pressure image data (red), for both pre- and post-processed data.

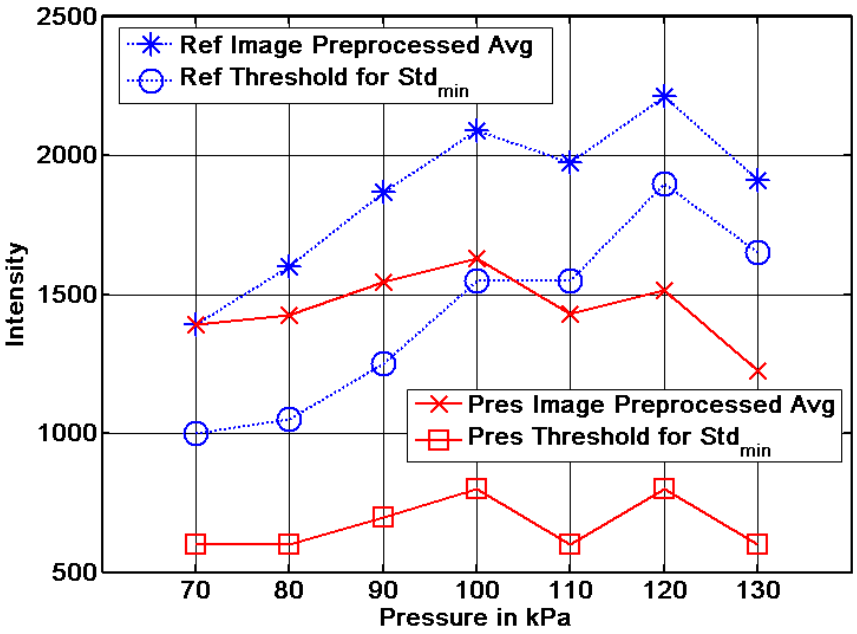


**Figure 3.26. Threshold intensities for minimum standard deviation and raw, preprocessed image averages against pressure showing similar trends between preprocessed average intensity and the minimum standard deviation threshold.**

The two reference plots share a similar trend and therefore, the threshold intensities to use during the image processing can be determined based on the raw reference images. To further investigate these patterns and reduce the standard deviations, the same study was performed on the pressure images' threshold while using the reference thresholds found in the previous study (blue). Again, the results are also shown in Figure 3.26 (red).

With the processed data still demonstrating high standard deviations (See Figure 3.27, left; 7.1% to 8.8%, 16 x 16 interrogation windows), two further investigations were performed. The first analysis involved looking back at the raw images, and cropping one third of the images on both sides, in order to eliminate the dark regions in these areas that are evident in Figure 3.24. This approach reduced the standard deviation, in this particular case, from 0.06 to 0.045 (See Figure 3.27, middle).

The second investigation was performed involving a detailed analysis of the distribution of ratios per interrogation window (also 16 x 16 pixels) and the corresponding parameters associated with the low and high end outliers, such as raw image average intensities or percentage of pixels ignored in the interrogation window processing. Often in the processed images, the interrogation windows with outlier ratios had a low average intensity in either the reference or pressure image or a significant number of pixels ignored (due to thresholding), both

of which resulted in erroneous ratios. In an attempt to remove these outliers, an analysis of various cutoffs was performed. The first involved adjusting an intensity cutoff so that interrogation windows with average intensities below the cutoff were ignored on the basis of being too dim for quality signal-to-noise. Similarly, the second cutoff involved ignoring interrogation windows where the averages were calculated with less than a prescribed percentage of pixels/window. The final values for these cutoffs were determined based on what cutoff values would reduce those erroneous ratios. An example of this cutoff study is shown in Figure 3.27 (right), which drops the standard deviation in a similar magnitude as the cropping study.

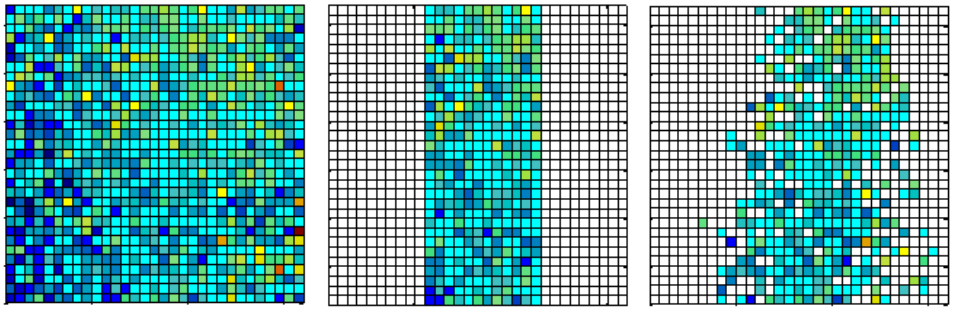

**Figure 3.27. Example of ratios for an image pair at 90kPa without any cutoffs (left), with side cropping (middle), and with intensity and pixel percentage cutoffs (right).**

Using this last approach, Figure 3.28 shows the mean intensity ratio normalized with the ratio at 100kPa, for an interrogation window size of 16 x 16 pixels. This interrogation window size results in 1024 ratio values per image. The average ratio per image and standard deviation are again averaged over the 50 images per pressure, and then plotted. The error bars represent the standard deviation for each pressure. The improved standard deviations now range from 5.6% to 6.8% (16 x 16 interrogation windows).

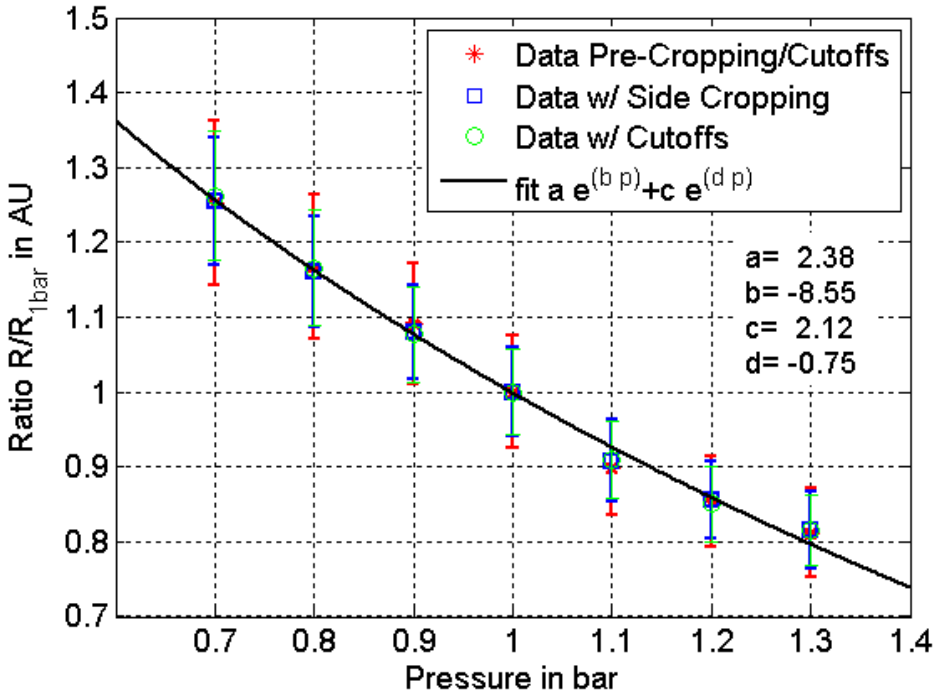


**Figure 3.28. Normalized mean ratios of emission intensity of the pressure and reference dye over varying pressure for 16 x 16 pixel interogation windows**

As described, the mean ratios and standard deviation were calculated for different interrogation window sizes. Table 3.3 summarizes the average standard deviation over all pressures obtained for each interrogation window size. The standard deviation increases with decreasing interrogation window size. A standard deviation of <10% was regarded as tolerable by Kimura *et al.*[21] and could be easily reached with a 16 x 16 pixels interrogation window size. Table 3.3 also shows the reduction in standard deviation for each of the three studies performed on the data described earlier. However, these uncertainties in the pressures are unacceptably high for eventual wind tunnel applications.

**Table 3.3. Standard Deviation in percent for different interrogation windows**

| | 8 x 8 pixels | 16 x 16 pixels | 32 x 32 pixels | 64 x 64 pixels |
|---|---|---|---|---|
| **Pre-Thresholds** | 20.8 % | 9.3 % | 6.3% | 5.6 % |
| **Pre-Cropping / Cutoffs** | 15.8% | 7.6% | 4.5% | 3.5% |
| **Side Cropping** | 12.7% | 6.2% | 3.5% | 2.6% |
| **Cutoffs** | 11.8% | 6.1% | 3.6% | 2.7% |

With the data processing and various investigations into the standard deviations for developing the 2-D calibration curve complete, the focus moved on to the calibration surface. As described above, processed images were used to plot the ratios against reference intensities for each interrogation window and for each image pair (pressure step), as seen in Figure 3.29 (top). The data were fitted to dual-exponential curves, shown in Figure 3.29 (bottom), which was consistent with the methods outlined during the stationary PTSBeads tests processing.

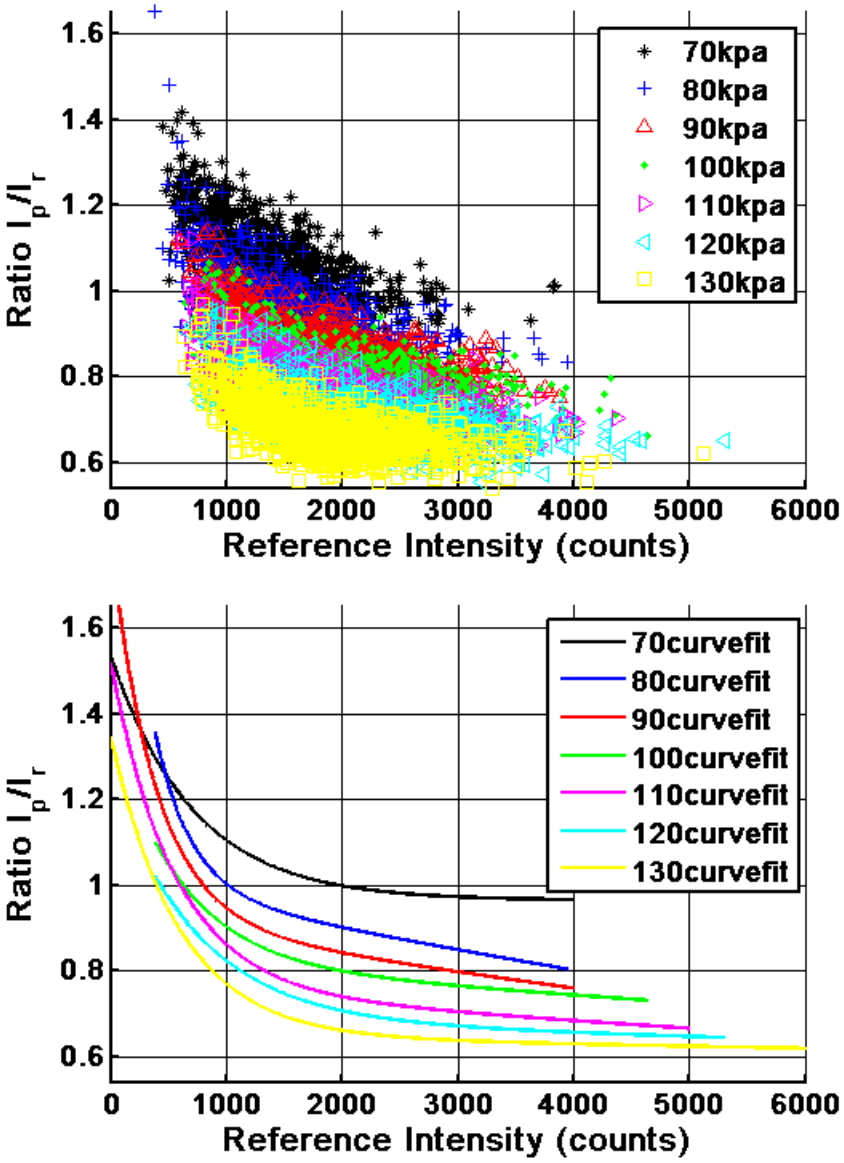


**Figure 3.29. Plot of intensity ratios vs. reference intensities for each interrogation window (16 x 16 pixels) in the first image pairs at each pressure (top) and the associated fitted curves (bottom)**

Again, just as in the stationary PTSBeads test processing to characterize the effects of different laser power, the individual curve fits were assigned their pressure values as the third dimension before using the MATLAB fitting tool to generate a 43-polynomial surface fit. The calibration surface and individual curve fits of 16 x 16 pixels interrogation windows is presented in Figure 3.30. This calibration surface was used to calculate pressures for the image pairs. The average pressures per image pair were accurately calculated by the surface to within 1kpa. The average standard deviation of these calculated pressures is given in Table 3.4. The spread of pressures for 16 x 16 pixels interrogation windows was still just under 10kPA. An ideal set of

data, similar to the stationary PTSBeads testing, would result in constant pressures for the calibration images with low standard deviations. Similar threshold studies from the single calibration curve processing were performed with no improvement to the standard deviation. Contrary to expectations, using thresholds on the interrogation windows decreased the sensitivity and accuracy of the surface calibration method. This is expected since this method takes even the low signal pixels and interrogation windows into account to generate the calibration surface.

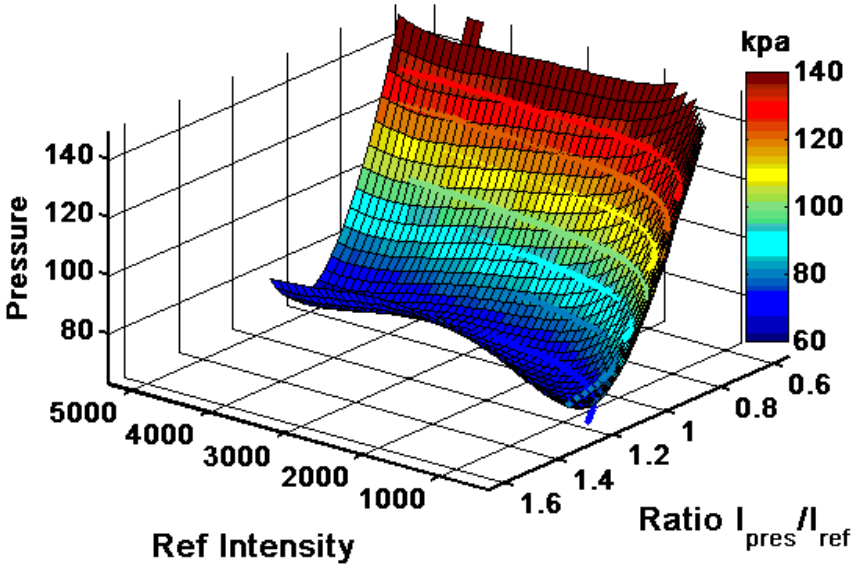


**Figure 3.30. Calibration surface and individual fitted curves from the first image pairs of the aerosolized tests**

**Table 3.4. Average standard deviation of pressures for varying interrogation window sizes**

| 8 x 8 pixels | 16 x 16 pixels | 32 x 32 pixels | 64 x 64 pixels |
|---|---|---|---|
| 19.90 kPa | 9.49 kPa | 5.61 kPa | 4.21 kPa |

Since the eventual progression of this experiment is to test in wind tunnels for the determination of velocity and pressure, PIV was performed on the data. With a pair of pressure and reference images, the pressure ratios can obviously be determined and from two consecutive reference images in time, the velocity field can be determined. Figure 3.31 shows an example of PIV performed on two reference images as well as the corresponding pressure ratios, using the 2-D calibration curve. The velocity field along with the pressure from these aerosolized PTSBeads are coupled together to resolve pressure and velocity simultaneously at each point associated

with the size of the interrogation windows. That is, for smaller interrogation windows, the pressure and velocity values can be determined at more points in space (higher resolution).

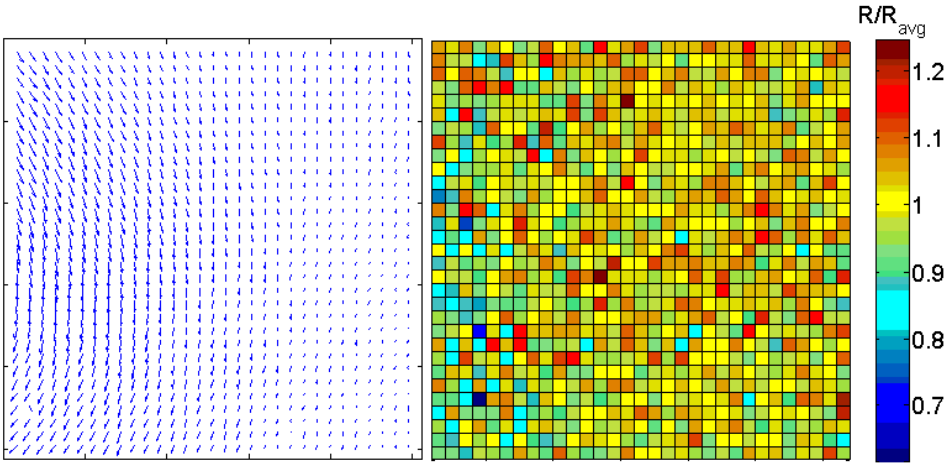


**Figure 3.31. Example of a PIV determined velocity field and the corresponding intensity ratio contour plot at 100kpa (R/Ravg in this case is equivalent to R/R100kpa)**

For this particular experiment the consecutive reference images were taken at 10Hz, which corresponded to a 100ms time difference (Δt). Since the aerosolized PTSBeads were simply free-floating in the chamber at very slow speeds, the PIV had to be performed with a large Δt. With faster flowing PTSBeads, such as in a wind tunnel, the continuous laser and/or long exposure time of the camera would cause streaking in the images. To alleviate this, a pulsed laser, such as the 532nm Nd:YAG, would be required to keep the light emitted by the PTSBeads brief but with enough energy for the camera to pick up the light. As in standard PIV methods, a double pulse would be used to shorten the Δt to achieve two consecutive images for PIV calculations. With these short Δt, a high frame rate camera would be needed for the reference dye imaging without sacrificing sensitivity. However, the camera to capture the pressure dye in the PTSBeads would not need the high frame rate as the pressure images would be matched to every other reference image.

# Chapter 4. CONCLUSIONS

The response times of different pressure-sensitive multi-dyed microbeads to passing shock waves were measured. The silica-based microbeads exhibited response times ranging between 26 μs and 462 μs. The majority of the silica-based samples showed adequate response times for use in unsteady flow investigations. The particular microbeads tested exhibited high signal-to-noise ratios as well as high sensitivity while maintaining their fast response times. The data revealed that the most significant contribution to response time is the fabrication method of the microbeads, particularly since the two steps method of fabrication consistently produced fast responding microbeads. The dye loading of the microbeads showed no correlation to the response times. Therefore, the fabrication and method of incorporating the dyes into the microbeads is the underlying contributor to the response time, not the amount of each dye. Further characterization of different particle and pressure-sensitive dye combinations presented additional options for fast-responding particles including aluminum oxide and zinc oxide particles. Dye A was chosen as the primary candidate for future multi-dye testing with fast-responding microbeads to replace the polystyrene microbeads. Future work will report on temperature response time measurement methods as well as their results.

The intensity ratio method has been investigated regarding it's feasibility for simultaneous velocity and pressure measurements using both PTSBeads, doped with a pressure-sensitive dye, a temperature-sensitive dye and a pressure and temperature insensitive reference dye and PSBeads, coated with pressure-sensitive dye and reference dye. The stationary PTSBeads characterization showed the expected exponential decay in intensity ratio with increasing pressure due to oxygen quenching and outlined the intensity ratio’s dependency on laser energy, which could be account for with a surface calibration curve. The new calibration technique for pressure measurements using a ratio-metric method of multi-luminophor stationary PSBeads was developed. The calibration process resulted in accurate pressure measurements with novel standard deviations in the pressures, as low as 74Pa to 106Pa, with the pressure dye alone and ratio-of-ratios method, respectively.

The pressure standard deviations in this new calibration method of stationary PSBeads decreased to improved levels. Preliminary aerosolized microbead testing was conducted to

develop the calibration for 2-D fluid flow pressure measurements. With the employment of this new process to aerosolized microbeads, the measurements can be combined with PIV to determine simultaneous pressure and velocity. The data from these experiments proved that both the single calibration curve and the calibration surface methods could be applied to calculate the pressure for the aerosolized PTSBeads. However, the aerosolized pressure calculations showed high standard deviations rather than uniform pressures as determined from the stationary calibration technique.

This work presents a new measurement technique for simultaneous pressure and velocity using an intensity-based ratio metric method of multi-dye luminescent PTSBeads. Future research of this group will concentrate on utilizing the calibration technique with aerosolized microbeads and develop a precise measurement system of flow field pressures and velocities. The primary goal of this will be on reducing the uncertainties from aerosolized calibration and testing. Aerosolized testing of the new fast-responding microbeads will be implemented for eventual testing in wind tunnel and turbulence conditions. Additionally, PSBeads will be tested with a pulsed 355nm Nd:YAG laser which will allow for a broader range of luminescent dyes and avoid any spectral overlap issues. Finally, the implementation of a three-camera system for simultaneous velocity, pressure, and temperature measurements using PTSBeads would further motivate the development of this measurement technique.

# BIBLIOGRAPHY


[1] Khalil G, Crafton J, Fonov S, Goss L, Dabiri D, Luminescent Method for Pressure Measurement (2013) Handbook of measurement in science and engineering, Vol. 1, 567-614, Kutz M, Ed., Wiley, Hoboken, New Jersey, USA

[2] Childs Peter R N, Temperature Measurement (2013) Handbook of measurement in science and engineering, Vol. 1, Kutz M, Ed., Wiley, Hoboken, New Jersey, USA pp 483-525

[3] Kavandi J, Callis J B, Gouterman M, Khalil G E, Wright D A, Green E, Burns D H, McLachlan B, (1990) Luminescent barometry in wind tunnels. Rev. Sci. Instrum. 61, 3340–3347

[4] Gouterman M, J. Chem. Educ. 74, 697 (1997).

[5] Bell J H, Schairer E T, Hand L A, & Mehta R D (2001) Surface Pressure Measurements Using Luminescent Coatings 1. Annu. Rev. Flu. Mech., 33(1), 155-206

[6] Liu T, Sullivan J P (2005) Pressure and temperature sensitive paints, Springer, New York, USA

[7] Demas J N, DeGraff B A, and Coleman P, Anal. Chem. 71, 793A (1999).

[8] Innovative Scientific Solutions, Inc, Dayton, OH 45440. http://www.psp-tsp.com/

[9] Vollan A, and Alati L, International Congress on Instrumentation in Aerospace Simulation Facilities Record, International Congress on Instrumentation in Aerospace Simulation Facilities, 1991 (unpublished), p. 10.

[10] Ruyten W, Sellers M (2004) On-Line Processing of Pressure-Sensitive Paint Images. Journal of Aerospace Computing, Information, and Communication, Vol. 1 no. 9 pp 372-382

[11] Vardaki E, Stokes N, Fonov S D, Crafton J, (2010) Pressure Sensitive Paint Measurements at the ARA Transonic Wind Tunnel, AIAA-2010-4796

[12] Mosharov V E, Radchenko V N, & Fonov S D (1998) Luminescent Pressure Sensors in Aerodynamics. Central Aerodynamic Institute (TsAGI), Moscow

[13] Engler R, Fey U, Henne U, Klein C, & Sachs W (2005) Quantitative Wind Tunnel Studies Using Pressure- and Temperature Sensitive Paints. Journal of Visualization, Vol. 8, pp. 277-284

[14] Bencic T J, (1998) Rotating pressure and temperature measurements on scale-model fans using luminescent paints

[15] Gregory J W, Asai K, Kameda M, Liu T, and Sullivan J P, (2008) *J. Aerospace. Eng.*, **222**, 249

[16] Aerospaceweb.org http://www.aerospaceweb.org/design/psp/characteristics.shtml

[17] Dabiri D (2006) Cross-Correlation Digital Particle Image Velocimetry – A Review. in Turbulência, Ed. Freire, A.S., Iiha A., Breidenthal B., Associação Brasileira de Engenharia e Ciências Mecânicas (ABCM),.

[18] Keane, R. D., & Adrian, R. J. (1991). Optimization of particle image velocimeters: II. Multiple pulsed systems. Measurement science and technology, 2(10), 963.

[19] Raffel, Markus, Christian E. Willert, and Jürgen Kompenhans. Particle Image Velocimetry: A Practical Guide; with 24 Tables. Springer, 1998.

[20] Abe S, Okamoto K, and Madarame H (2004) The development of PIV=PSP hybrid system using pressure sensitive particles. Meas. Sci. Tech. 15, 1153

[21] Kimura F, McCann J, Khalil GE, Dabiri D, Xia Y, Callis JB (2010) Simultaneous velocity and pressure measurements using luminescent microspheres. Rev Sci Instrum 81:064101, DOI 10.1063/1.3422324

[22] Im S H, Khalil G E, Callis J, Ahn B H, and Xia Y (2005) Synthesis of polystyrene beads loaded with dual luminophors for self referenced oxygen sensing. Talanta, 67(3), 492-497

[23] Kimura F, Khalil G, Zettsu N, Xia Y, Callis J, Gouterman M, Dalton L, Dabiri D, and Rodriguez M, (2006) Meas. Sci. Technol. 17, 1254

[24] Khalil G E, Costin C, Crafton J, Grenoble S., Gouterman M., Callis J B, & Dalton L R (2004) Dual Luminophor Pressure Sensitive Paint I: Ratio of Reference to Sensor Giving a Small Temperature Dependency. Sensors and Actuators B: Chemical, 97(1), 13-21

[25] Gouterman M, Callis J B, Dalton L R, Khalil G, Mébarki Y, Cooper K R, & Grenier M (2004) Dual Luminophor Pressure Sensitive Paint III: Application to Automotive Model Testing. Measurement Science and Technology, 15(10), 1986

[26] Kose ME, Carroll BF, Schanze KS (2005a) Preparation and spectroscopic properties of multiluminophore luminescent oxygen and temperature sensor films, Langmuir, 21, 20, 9121-9129

[27] Kose ME, Crutchley RJ, DeRosa MC, Ananthakrishnan N, Reynolds JR, Schanze KS (2005b) Morphology and oxygen sensor response of luminescent Ir-labeled poly(dimethylsiloxane)/polystyrene polymer blend films, Langmuir, 21, 18, 8255-8262
[28] Kimura F, Rodriguez M, McCann J, Carlson B, Dabiri D, Khalil G, Callis J B, Xia Y, and Gouterman M (2008) Development and characterization of fast responding pressure sensitive microspheres, Rev. Sci. Instrum. 79, 074102
[29] O. C. Brown (2000) Low-Speed Pressure Measurements Using a Luminescent Coating System, Stanford University Doctoral Thesis
[30] Winslow N A, Carroll B F, and Kurdila A J (2001) AIAA Journal 39, 660
[31] Carslaw H S, Jaeger J C, Conduction of Heat in Solids, Clarendon Press, 1959, Sec. 9.3.
[32] Saad M A (1993) *Compressible Fluid Flow* (2nd ed.). Englewood Cliffs, New Jersey: Prentice Hall. P. 187.
[33] Gregory J W, Sullivan J P, (2006) Effect of Quenching Kinetics on Unsteady Response of Pressure-Sensitive Paint, AIAA Journal, Vol. 44, No. 3
[34] Hirotaka Sakaue, Katsuaki Morita, Yoshimi Iijima, Yoshitaka Sakamura, (2013) Response time scales of anodized-aluminum pressure-sensitive paints, Sensors and Actuators A: Physical
[35] Stern O, Volmer M (1919) Phys. Z. 20
[36] Zhu C, Deng R, Khalil G E, Dabiri D, Gu Z, Xia Y, (2013) Synthesis and Characterization of Pressure and Temperature Dual-responsive Polystyrene Microbeads, Particle & Particle Systems Characterization, accepted for publication
[37] Kimura, F (2009) Novel measurement techniques for the study of unsteady flow phenomena: shear sensitive paint and pressure sensitive microspheres. Ph.D. Dissertation, University of Washington
[38] Meier R J, Fischer L H, Wolfbeis O S, & Schaeferling M (2013) Referenced luminescent sensing and imaging with digital color cameras: A comparative study. Sensors and Actuators B-Chemical, 177, 500-506
[39] Goss L P, Crafton J W, Jones E G, & Forlines R A (2007) Lifetime based pressure sensitive paint systems: issues and solutions. In Instrumentation in Aerospace Simulation Facilities, 2007. ICIASF 2007. 22nd International Congress on (pp. 1-12). IEEE.
[40] Prevo B G, Velev O D (2004) Controlled, Rapid Deposition of Structured Coatings from Micro- and Nanoparticle Suspensions. Langmuir, 20, 2099-2107
[41] Hecht, J (1992) The laser guidebook. Tab Books
[42] Huang C Y, Lai C M, & Li J-S, (2012) Applications of Pixel-by-Pixel Calibration Method in Microscale Measurements with Pressure-Sensitive Paint. J. Microelectromech. Syst., vol. 21, no. 5, Oct

# APPENDIX

Appendix 1

# Stern-Volmer Tutorial and Guide

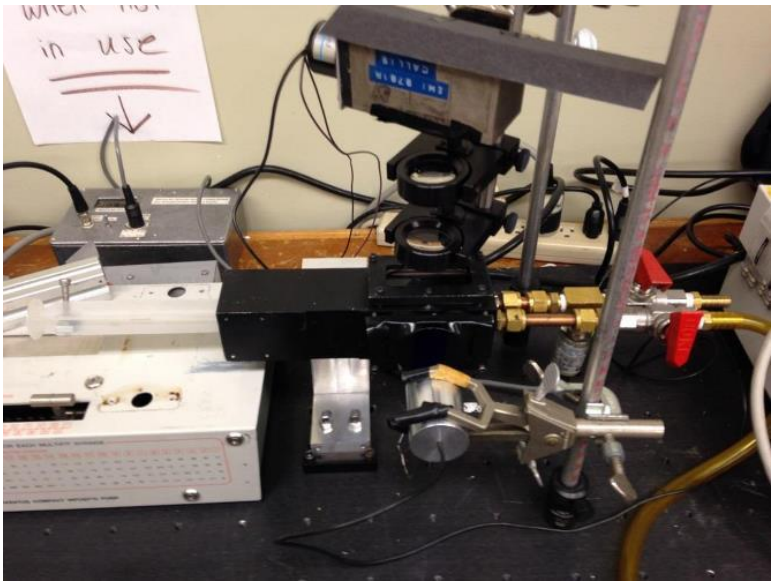


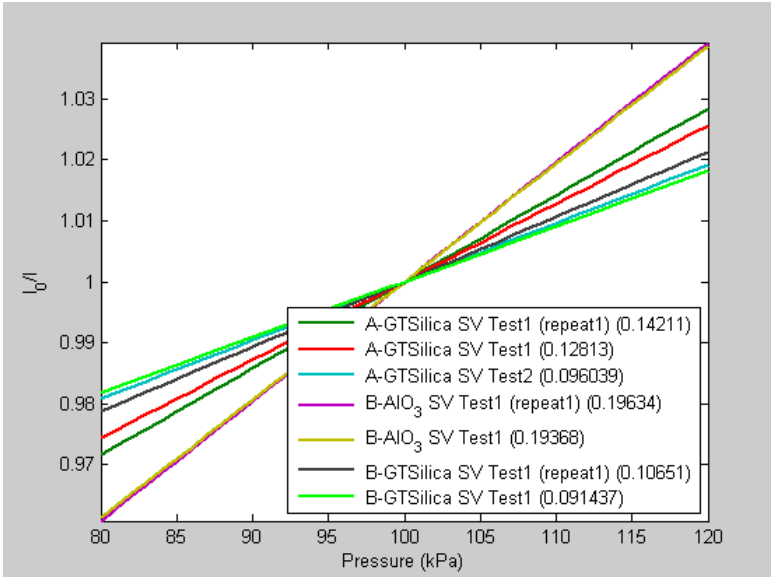


**By Daniel Lacroix**
**Master's Student**
**Dept. of Aeronautics and Astronautics**
**University of Washington**

**January 2014**

**Note to reader: This document is intended as a tutorial for determining the Stern-Volmer curves for pressure-sensitive particles in the Digital Luminescent lab. Read this entire document before proceeding through the steps to produce the Stern-Volmer plots.*

## Contents



**Supplementary files:**

…\Tutorial (Sup files)\NAMEMATRIX.mat
…\Tutorial (Sup files)\Data\132 SV Redo1.txt
…\Tutorial (Sup files)\Data\sv_132 SV Redo1.mat
…\Tutorial (Sup files)\Data\ sv_132 SV Redo1.fig
…\Tutorial (Sup files)\Data\SV_all.fig
…\Tutorial (Sup files)\Data\SV_all_fitted.fig
…\Tutorial (Sup files)\Data\Infomatrix.mat

Appendix 3

## I. SETUP

**WARNING: Always use laser goggles when operating and aligning laser light sources.**

1. Mount the pressure chamber onto an appropriate surface with enough space for the laser light source, PMT box, and additional power supply and control boxes.
2. Attach a narrow bandpass filter for the appropriate light source range to the side window of the chamber as shown in Figure 1. (i.e. use the 405nm narrow bandpass filter with the 405nm laser diode)
3. Clamp the light source in front of the side window and bandpass filter in order for the light to go straight through the filter into the chamber as seen in Figure 1. (i.e. point 405nm laser straight through the 405nm filter into the center of the chamber) CAUTION: When using a laser, keep the beam defocused and divergent so that a focused beam does not cause burn damage to the sample or inner walls of the chamber.

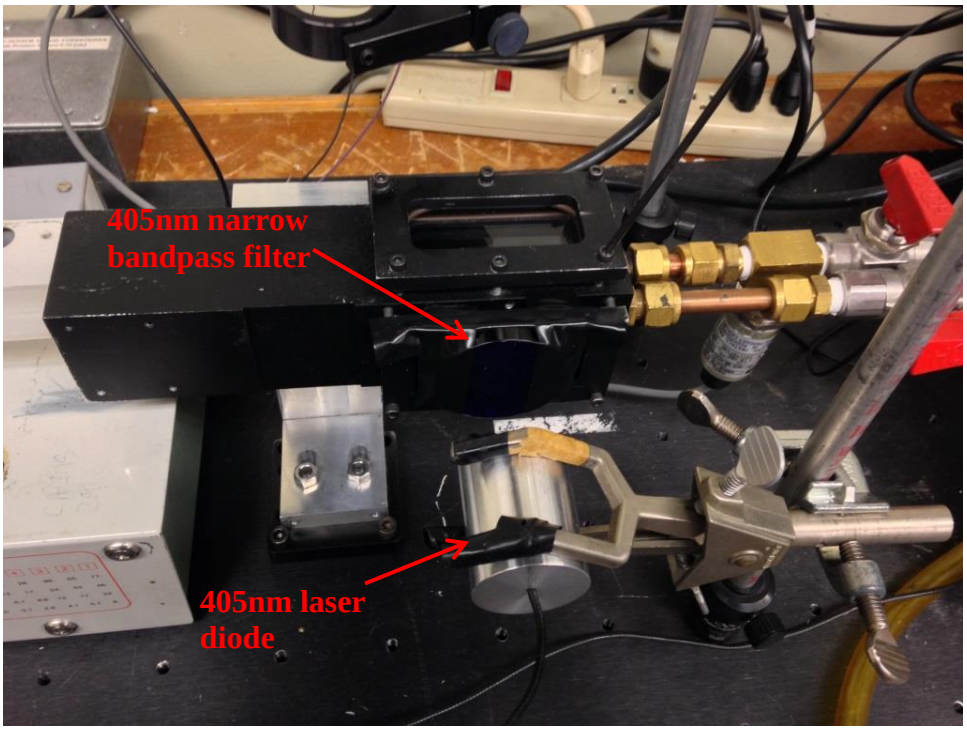


**Figure 1: Pressure chamber and laser light source setup**

4. Unscrew the top window plate, carefully remove the glass window, and place the pressure-sensitive sample in the chamber in line with the light source and at a slight tilt as shown in Figure 2. (Tape slide sample to smaller glass piece for easier access and handling)

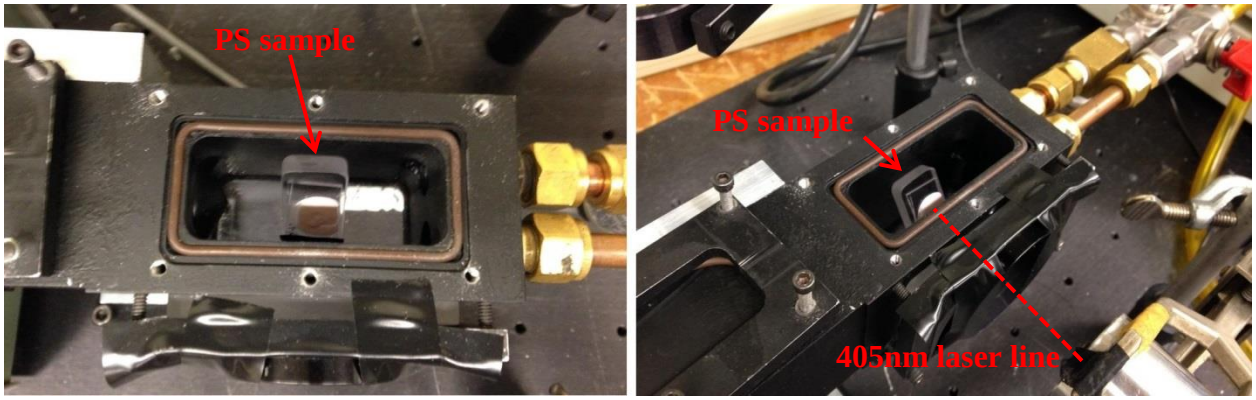


**Figure 2: Pressure-sensitive sample set in pressure chamber in line with light source**

5. Place the glass window back on the O-ring and then screw the top window plate back onto the chamber with a second O-ring between the glass and plate as shown in Figure 3. Carefully, screw the plate onto the chamber so that the glass window has a tight and flat seal against the O-rings being mindful not to over tighten. (screws do not necessarily have to be tight just the pressure of the plate and O-ring against the window) CAUTION: Screwing the plates back on the chamber against the glass without the second O-ring and/or unevenly will damage the glass and may cause it to crack.

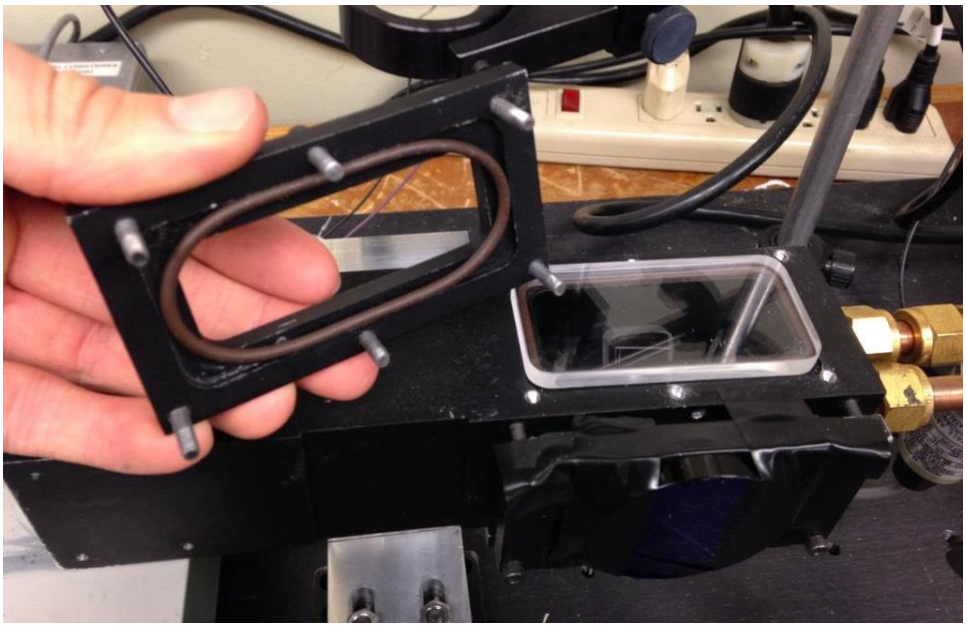

**Figure 3: Reattaching the glass window and top window plate to the chamber**

6. Attach a cutoff or bandpass filter to the PMT for the appropriate pressure-sensitive sample luminescence and to cutout the light source wavelength. (i.e. use around a 650 bandpass filter or cutoff filter in conjunction with A dye and a 405 laser)
7. Mount the PMT and focusing lenses above the top window in order to capture the light emitted by the pressure-sensitive sample as shown in Figure 4.

Appendix 5

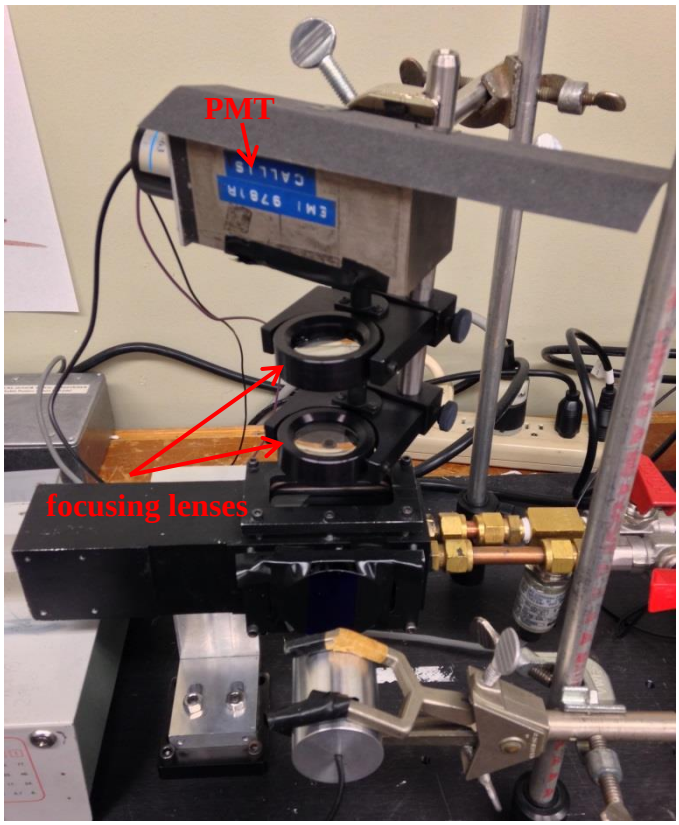


**Figure 4: PMT setup**

8. Close off one of the two pipe connector switches on the chamber and then connect the other to an easily variable valve whose other end will be connected to the vacuum pump as shown in Figure 5.

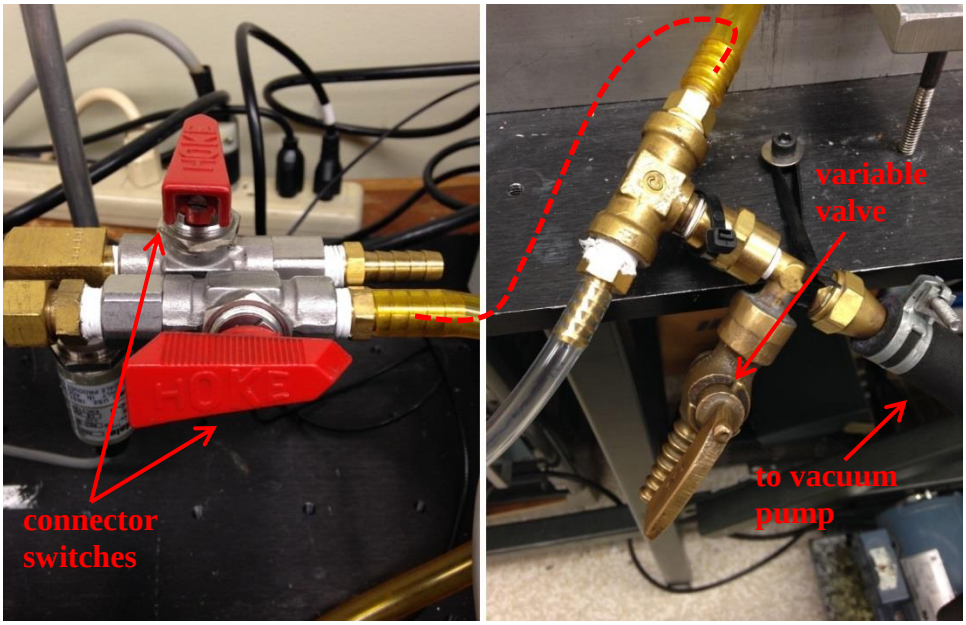


**Figure 5: Chamber pipe connector switches (left) and variable valve connected to vacuum pump (right)**

9. Make sure that the PMT gain box power supply, light source power supply (i.e. laser diode controller), and chamber pressure transducer power supply are all connected and ready (keep pressure transducer power supply off when not in use as it is powered by batteries) as shown in Figure 6.


**Figure 6: PMT gain box power supply (left); laser diode controller (middle); pressure transducer power supply (right)**

10. With the laser on a low power setting and the lights off, align the PMT and focusing lenses so that the luminescent light hits the center of the PMT opening and filter as seen in Figure 7.

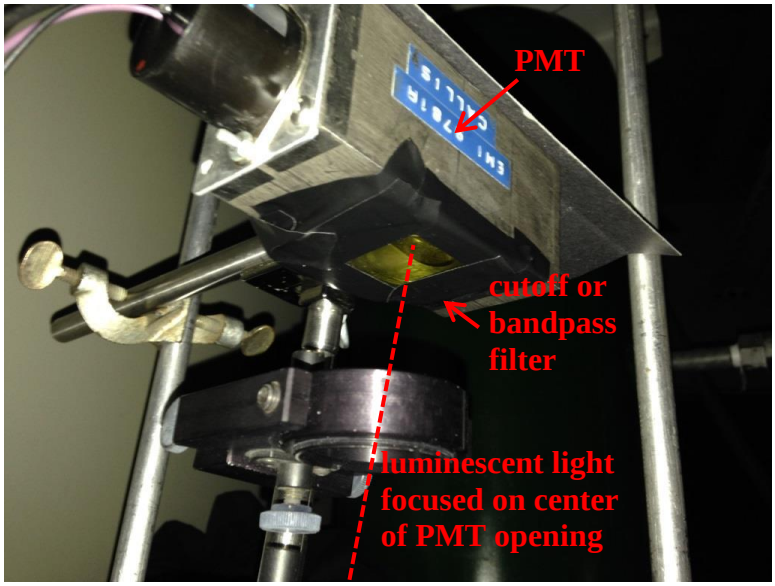


**Figure 7: View of bottom of PMT and filter attached**

11. Connect the pressure transducer power supply BNC cable to the National Instruments board *AI 1* port and the PMT gain box BNC cable to the *AI 3* port. (The absolute pressure transducer connected to the vacuum pump line and *AI 0* port is optional)
12. Start the LabVIEW test project called "SternVolmer Test Project" located in *C:\Users\Dana\Desktop\Dan\SternVolmer Test Project.seproj*.
13. With "Record While Running" set to off, click on the "Run" icon at the top left of the window to display the live signals. Verify that the pressure transducer is reading atmospheric pressure (i.e. 100kPa).
14. With the laser on and at an appropriate power level (i.e. 75-100), turn on the PMT power supply, turn the high voltage switch from "HV off" to "0" and adjust the voltage settings,

as shown in Figure 8, so that the PMT signal on the LabVIEW project is around -1 (i.e. voltage set to 270V).

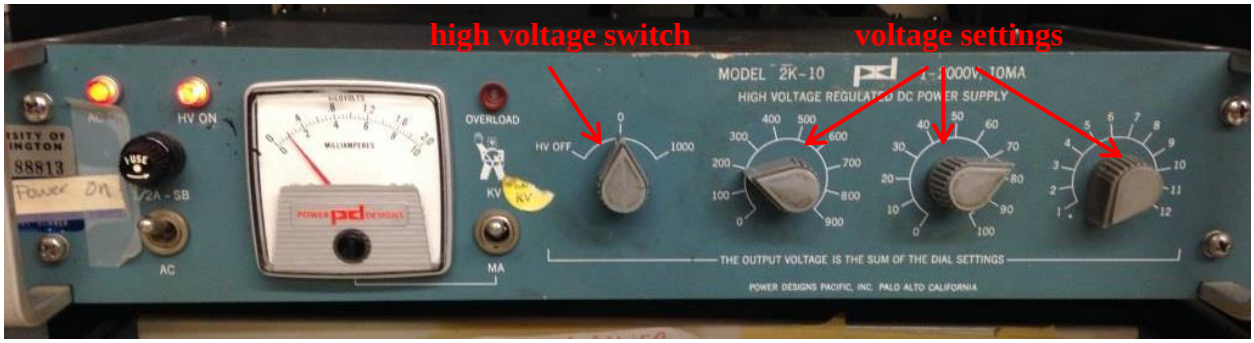


**Figure 8: PMT power supply**

15. Fine tune the alignment of the PMT and focusing lenses to maximize the PMT signal given constant settings.

## II. RUNNING

1. Pull the syringe out of the chamber so that it is just inside the chamber's syringe tube section. Close the connector switch leading to the vacuum pump.
2. Click on "Record While Running" to begin recording the pressure transducer and PMT signals. LabVIEW will first prompt the user for a filename and description as shown in Figure 9.

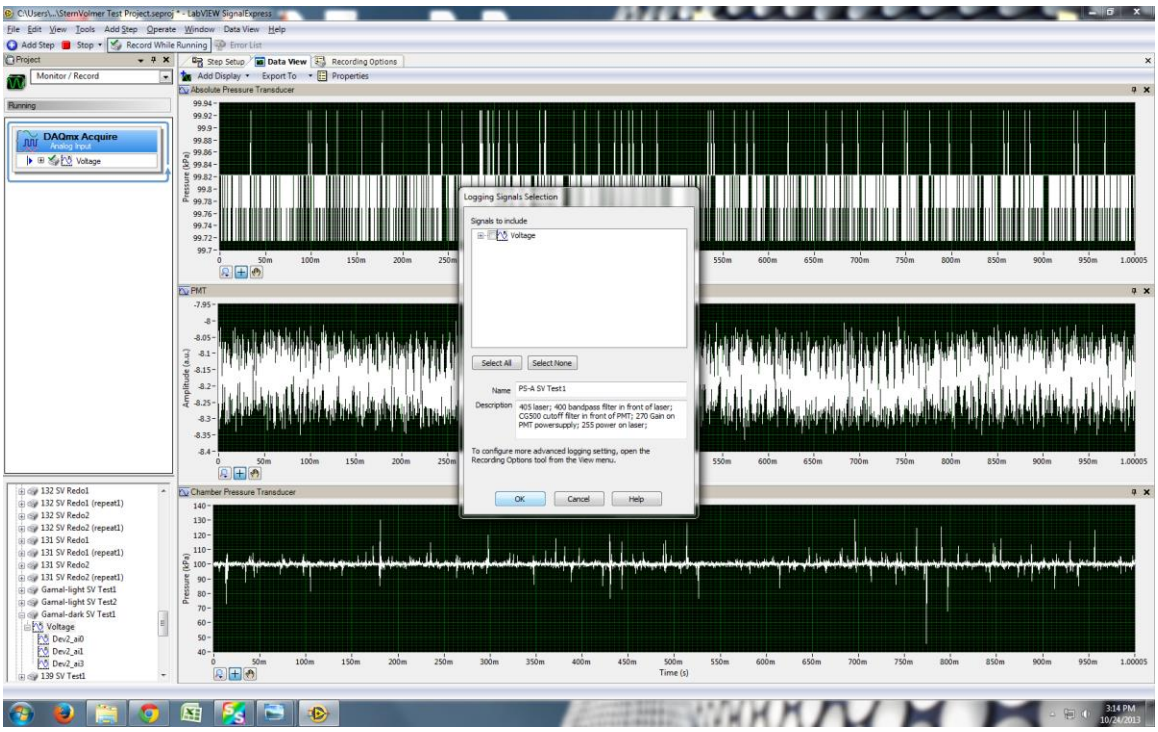


**Figure 9: LabVIEW of Stern-Volmer test pre-recording**

3. Immediately, but steadily push the syringe into the chamber to its full extent and then release to generate the positive pressure range of the test. Open the connector switch to the vacuum pump and then turn on the vacuum pump. Steadily turn the variable valve from fully open to fully closed to generate a careful decrease in pressure down to vacuum.

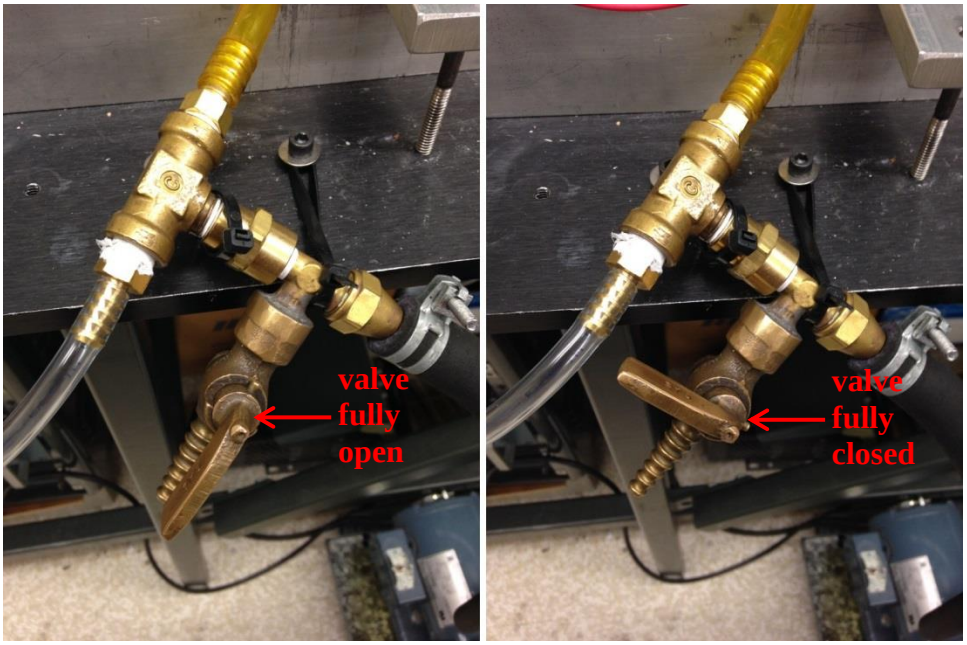


**Figure 10: Variable valve open and closed positions to vacuum pressures in chamber**

4. When both the pressure transducer signal and PMT signal reach a minimum click on the "Record While Running" again to stop the test run.
5. Turn off the vacuum pump.

## III. PROCESSING

1. The test run log will appear in the bottom left of the screen. Expand the log and open the signals. Check that the pressure transducer signal starts from atmospheric and increases to around 150kPa and then later drops down to near-vacuum as seen in Figure 11 and Figure 12. Verify that the PMT signal matches the pressure transducer signal, also shown in Figure 11 and Figure 12. (Note that Figure 11 shows a test run without any significant degradation in the pressure-sensitive signal while Figure 12 shows a test run with significant degradation in the signal)

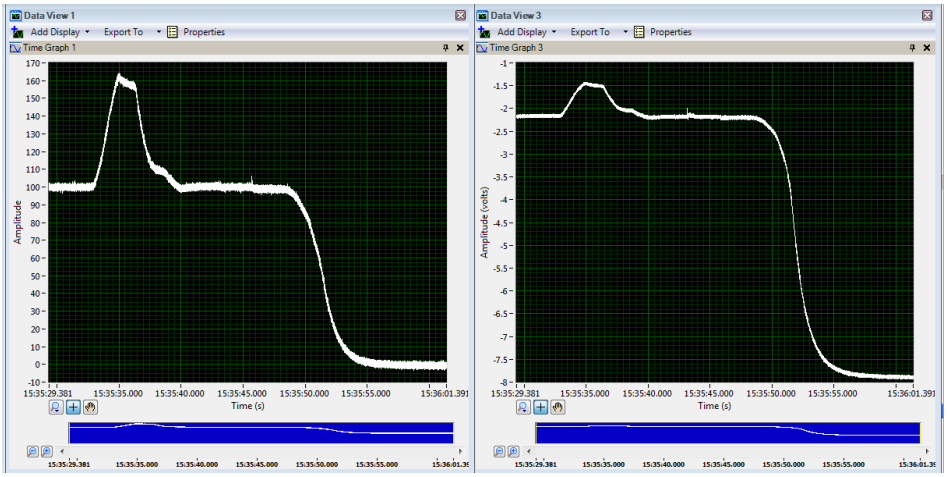


**Figure 11: Chamber pressure transducer (left); PMT signal (right) without degradation in the pressure-sensitive luminophor**

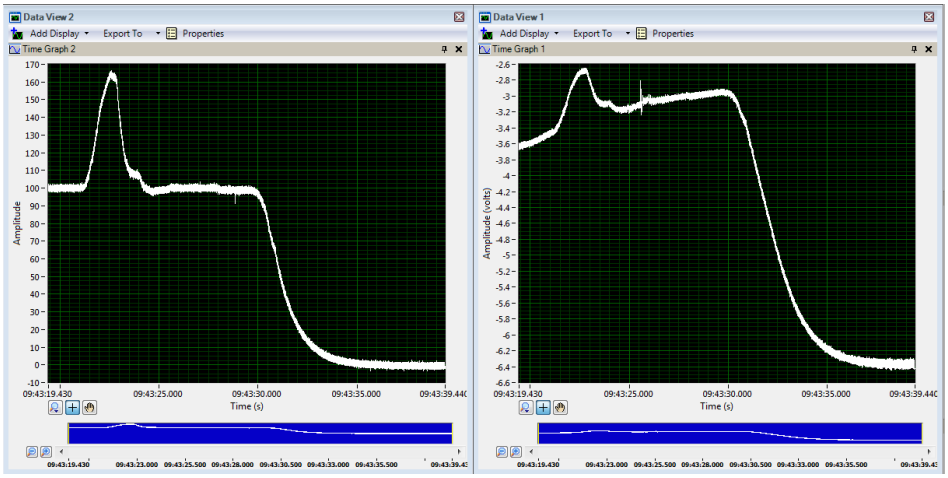


**Figure 12: Chamber pressure transducer (left); PMT signal (right) with degradation in the pressure-sensitive luminophor**

2. Right click on the "Voltage" subsection of the log and click on "Convert to Text" in order to output the data for processing, as shown in Figure 13. (Do not change the name or location of the text file in LabVIEW, instead save the text file and then rename and move in the windows explorer)

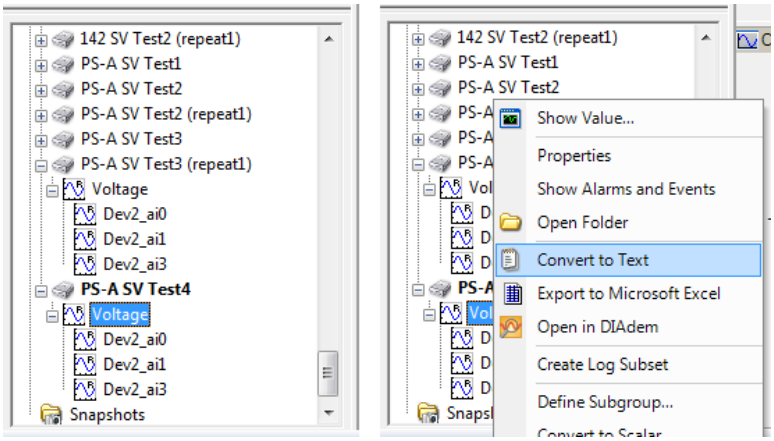


**Figure 13: Exporting signal data to text file**

3. Open MATLAB and the script “Stern_Volmer_v02.m”.
4. In the beginning section of the script declare the root directory where the text files of the log data are saved. Change the options if needed to plot intermediate and/or final figures, save the figures and/or .mat files, and/or take into account degradation of the pressure-sensitive signal as seen in the screenshot shown in Figure 14.

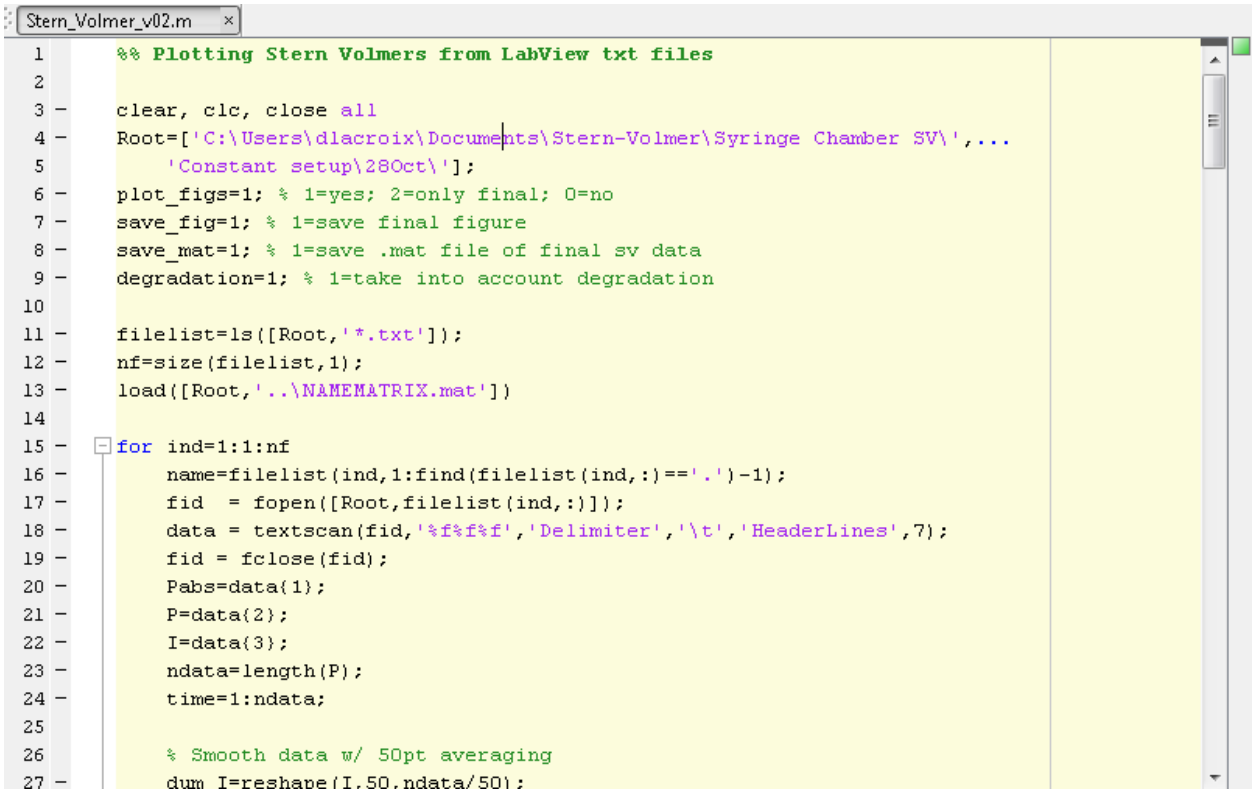


**Figure 14: Screenshot of the first lines of the Stern_Volmer_v02.m script**

5. If the text files were saved with a number representation of the full name, load the “NAMEMATRIX.mat”, open the “Namematrix” array, and manually input the shorthand number and the full name as shown in Figure 15.
6. Save the updated “Namematrix” array to the .mat file and return to the processing script.
7. Run the script by clicking on “Ctrl + Enter”.
8. If the degradation option was used then the first chart will prompt the user to select the location for calculating the average degradation. Select anywhere in the y-direction on either subplots but make sure to click on an x-direction location where the pressure is atmospheric pressure. (i.e. the last atmospheric pressure before the vacuum pressures is generally a good place to click as shown in Figure 16) (Note that the code takes the PMT signal at the selected location and the PMT signal at the first point in time, determines the linear fit of these two points, and then linearly de-trends the entire PMT data from this estimated linear degradation)

Namematrix ×

Namematrix <16x2 cell>

| | 1 | 2 |
|---|---|---|
| 1 | 121 | D-GT Partic... |
| 2 | 125 | D+Ln-AL_2... |
| 3 | 126 | Pt(II)Porph... |
| 4 | 127 | A.Orange-A... |
| 5 | 131 | B-CaCO_3 |
| 6 | 132 | B-ZnO |
| 7 | 133 | B-AL_2O_3 |
| 8 | 134 | A-AL_2O_3 |
| 9 | 135 | A-CaCO_3 |
| 10 | 136 | B-CaCO_3 |
| 11 | 137 | A-ZnO |
| 12 | 138 | B-ZnO |
| 13 | 139 | Pt(II)Lacton... |
| 14 | 140 | A.Orange-Z... |
| 15 | 141 | D+Ln-ZnO |
| 16 | 142 | Ruthenium... |
| 17 | | |

**Figure 15: Namematrix arrary with shorthand number designation on the left column and full name on the right column**

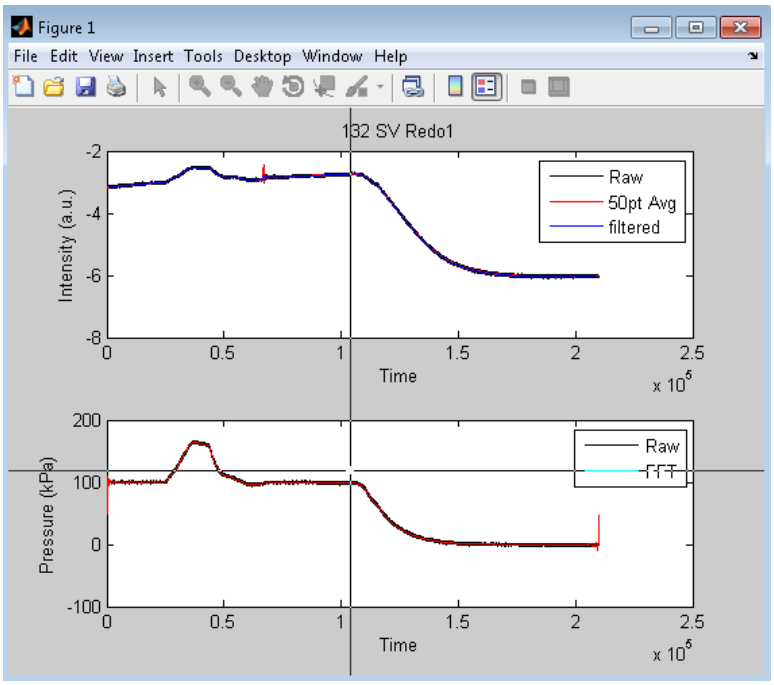


**Figure 16: Selecting the degradation calculation point**

9. If degradation was taken into account then the next chart will show the two subplots (PMT intensity and pressure) with the degradation section highlighted and the new de-trended data which should indicate better matching to the pressure, as in Figure 17.

10. If the de-trending was a success, select “Yes” on the “Degradation Removal” prompt, or else select “No” to continue without taking into account degradation for the particular test run or “Cancel” to break the processing.

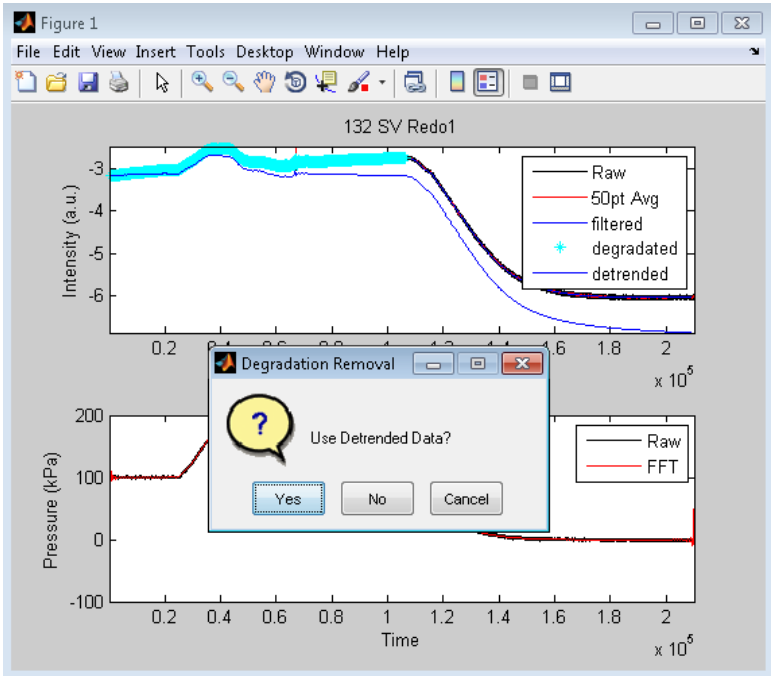


**Figure 17: Degradation section, new de-trended data, and degradation removal prompt**

11. When the two-y-axis chart of pressure and intensity appears select the ranges of positive and negative pressures that correspond to the steady increase with the syringe and steady decrease with the vacuum: Click the point at atmospheric pressure right before the increase, then click the peak pressure point, then the atmospheric pressure just before the vacuum decrease, and finally the vacuum pressure point as indicated in Figure 18 (vertical location of click does not matter).
12. One of the two final charts will show the processed data with the specified ranges highlighted. Verify that the desired ranges were correctly selected, as shown in Figure 19.
13. Verify that the final Stern-Volmer curve is smooth without any breaks, as shown in Figure 20.
14. Click “Yes” when prompted to continue processing the remaining test runs.
15. Repeat steps 8 through 14 until all text files are processed.

Appendix 13

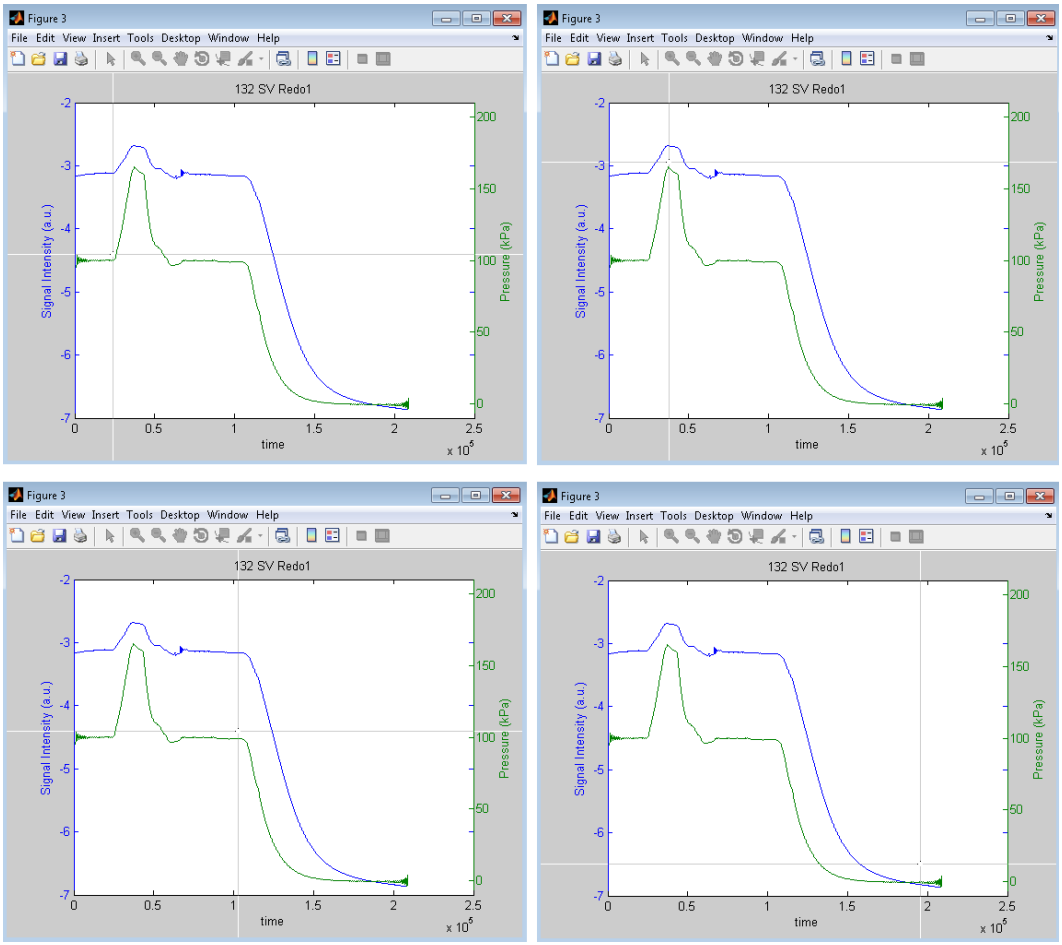


**Figure 18: First click (top left); second click (top right); third click (bottom left); fourth click (bottom right)**

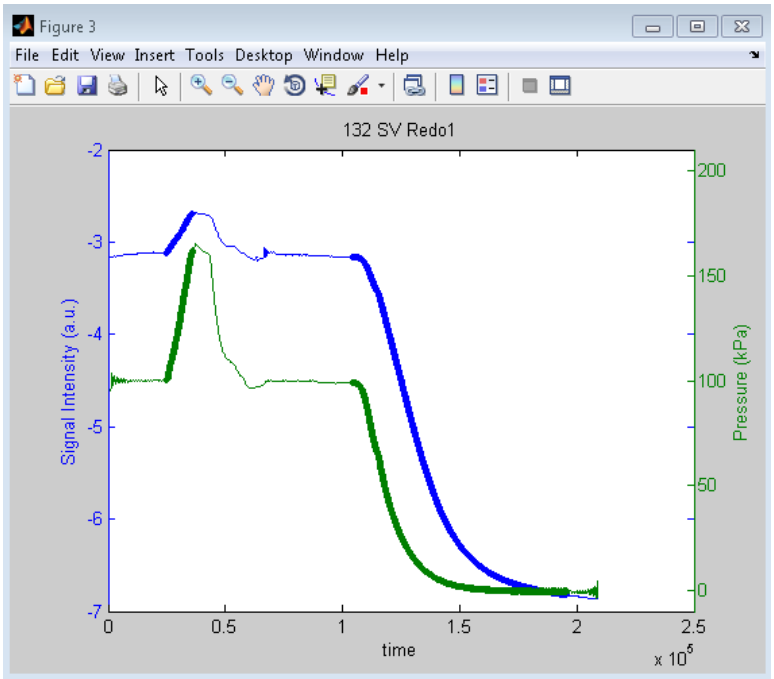


**Figure 19: Final selection of data for Stern-Volmer plot**

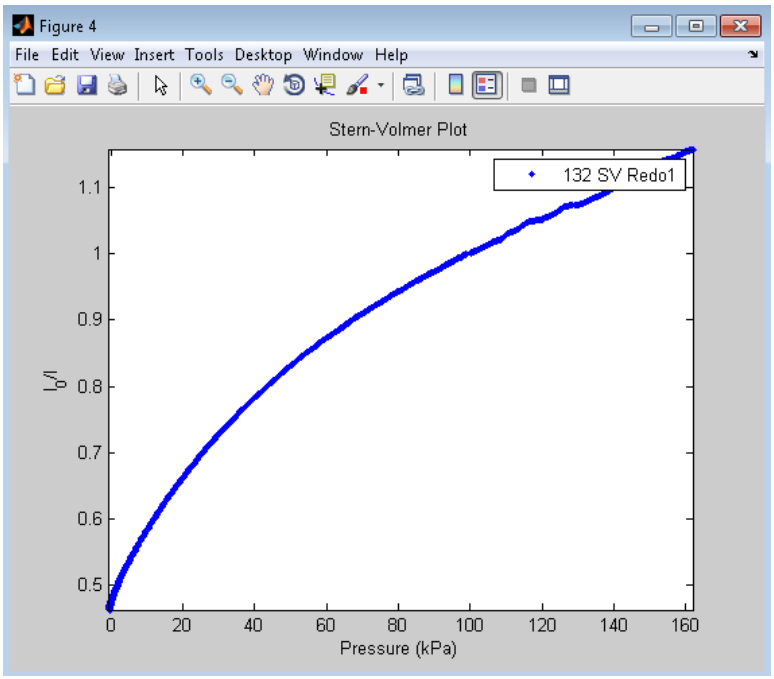


**Figure 20: Final Stern-Volmer plot for full range of pressures**

16. Once all test runs are processed advance to the next section of the "Stern_Volmer_v02.m" script.
17. Specify the root directory where the processed Stern-Volmer data are saved and change the save option if needed, as shown in Figure 21.

Stern_Volmer_v02.m

```
140     %% Plot all SV's together
141
142 -   clear, clc, close all
143 -   colors=['-k';'-r';'-g';'-b';'-m';'-c';'-y'];
144 -   clrs=[get(0,'DefaultAxesColorOrder');0 1 0];
145
146 -   saveall=1;
147     % namestr={'D-GT Particles';'D+Ln-AL_2O_3';'Pt(II)Porphol.-AL_2O_3';...
148     %     'A.Orange-AL_2O_3';'B-CaCO_3';'B-ZnO';'B-AL_2O_3';'A-AL_2O_3'};
149     % namestr={'A-CaCO_3';'A-CaCO_3 (thick)';'B-CaCO_3';...
150     %     'B-CaCO_3 (thick)';'B-ZnO'};
151
152 -   Root=['C:\Users\dlacroix\Documents\Stern-Volmer\',...
153         'Syringe Chamber SV\Constant setup\28Oct\'];
154 -   matlist=ls([Root,'sv_*.mat']);
155 -   nmat=size(matlist,1);
156 -   legendstr=cell(nmat,1); m=zeros(nmat,1); lgdstr=legendstr; namestr=lgdstr;
157 -   load([Root,'..\NAMEMATRIX.mat']) % names corresponding to sample #'s
158
```

**Figure 21: Screenshot of the first few lines of the second section of the Stern_Volmer_v02.m script**

18. Run this section of the script by clicking on "Ctrl + Enter" to plot all of the Stern-Volmer curves together for comparison. Verify that the curves were plotted together correctly in one of the final charts, as seen in Figure 22.

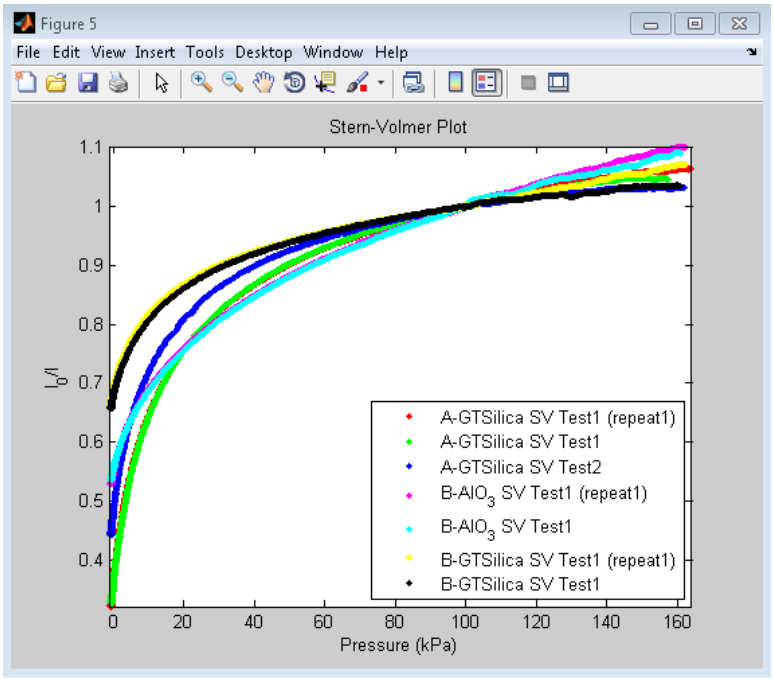


**Figure 22: Stern-Volmer curves plotted together across full pressure range**

19. The second of the two final charts estimates the near-atmospheric range (80kPa to 120kPa) of the Stern-Volmer curves as linear and determines the estimated slopes for comparison. Verify that the linear fits were calculated correctly, as in Figure 23.

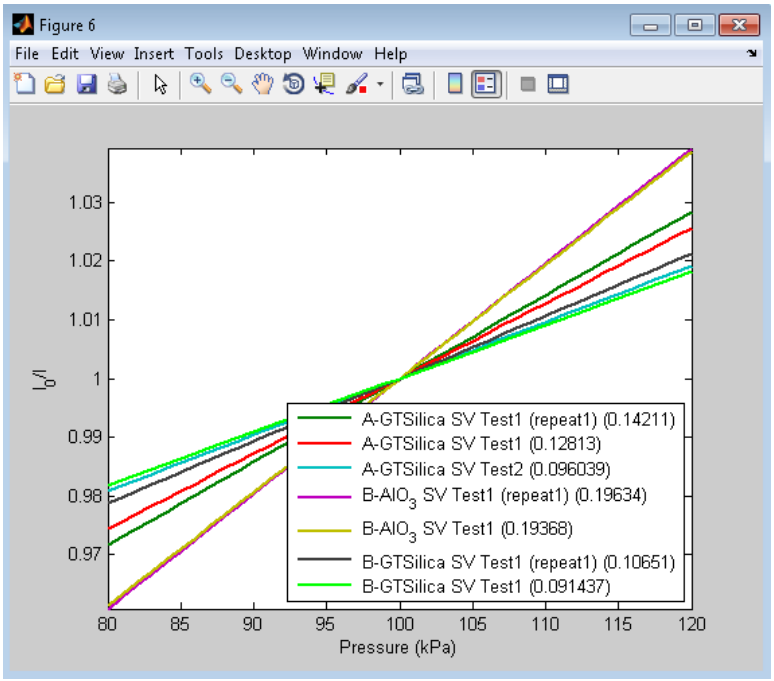


**Figure 23: Estimated linear fits of near-atmospheric range of Stern-Volmer curves**

20. Finally, verify that the saved "Infomatrix.mat" tabulated the test runs and calculated linear fit slopes correctly, as shown in Figure 24.

Appendix 16

Infomatrix | Infomatrix.labels | Infomatrix.mtrx

Infomatrix <1x1 struct>

| Field | Value | Min | Max |
|---|---|---|---|
| mtrx | <1x3 cell> | | |
| labels | <1x3 cell> | | |

Infomatrix | Infomatrix.labels | Infomatrix.mtrx

Infomatrix.labels <1x3 cell>

| | 1 | 2 | 3 | 4 |
|---|---|---|---|---|
| 1 | file name | sample name | 80-120 regression slope | |
| 2 | | | | |

Infomatrix | Infomatrix.labels | Infomatrix.mtrx

Infomatrix.mtrx <1x3 cell>

| | 1 | 2 | 3 | 4 |
|---|---|---|---|---|
| 1 | '132 SV Red... | 'B-ZnO' | 0.2716 | |
| 2 | | | | |

**Figure 24: Infomatrix.mat with test runs and calculated linear slopes**

Appendix 17

# Quantel YAG Laser Abridged Operating Procedures, Instructions and Maintenance



**By Daniel Lacroix**
**Master's Student**
**Dept. of Aeronautics and Astronautics**
**University of Washington**

**January 2013**

**Note to reader: This document is intended as a reference for basic operating of the Quantel YAG laser at the University of Washington and as an informational tool for a basic understanding of the maintenance processes of this system. It is in no way a complete guide nor does it substitute the official Quantel manuals. Actually following this guide through the maintenance procedures without professional aid and proper training is not recommended. For additional and detailed information see the Quantel Twins Brilliant and Brilliant b Instruction Manuals or contact Quantel customer service.*

## Contents

# Basic Operating Procedures

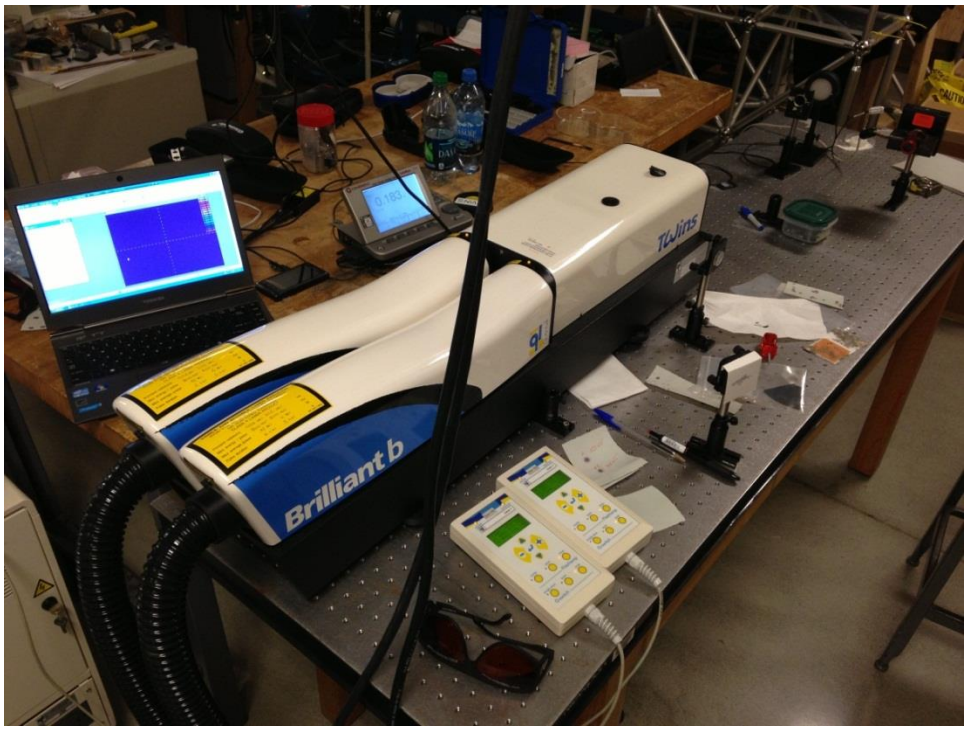


1. Wear safety goggles, appropriate for 532nm and/or 1064nm laser light, and display any lab "laser in use" warnings.
2. For initial startup, make sure the water cooling system and chiller are both on. (See *Operating and Maintenance of Water Cooling System* section for detailed information)
3. Setup a power or energy meter at the output of the laser in order to hone the output energy of each laser to the required 400mJ. Offset the meter at a slight angle so that the reflection from the face of the meter does not travel back through the laser. (WARNING: Always be conscientious of surface reflections of the laser and scattered laser light as even small percentages of reflection can cause damage and/or injury)
4. Turn on the flashlamps by simply hitting the "ready" and then "start" buttons on the remote boxes. Check that the temperature on the cooling system does not exceed 38 degrees C. (The flashlamps should by run with the water cooling system once a week at least in order to keep clean water cycled through the system)
5. Make sure that the output shutter is open and begin Q-switching by pushing the Q-switch "start" button on the remote box. (WARNING: Be aware of any reflected/scatter beam and if a significant audible snapping occurs somewhere other than the laser, a beam may be impacting an unwanted surface)
6. See *Reassembly* section for detailed information on testing the beam profile and maximizing energy if not at 400mJ for each laser.

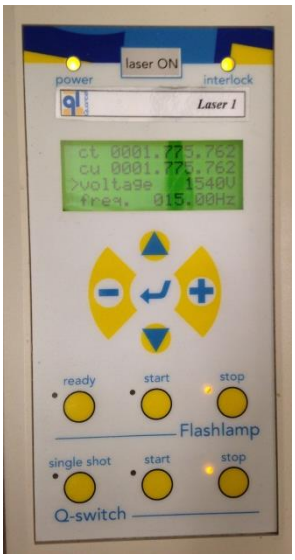

# Routine Cleaning and Maintenance of Laser Components

(Disassembly and maintenance of laser components not recommended without proper training and Quantel support)

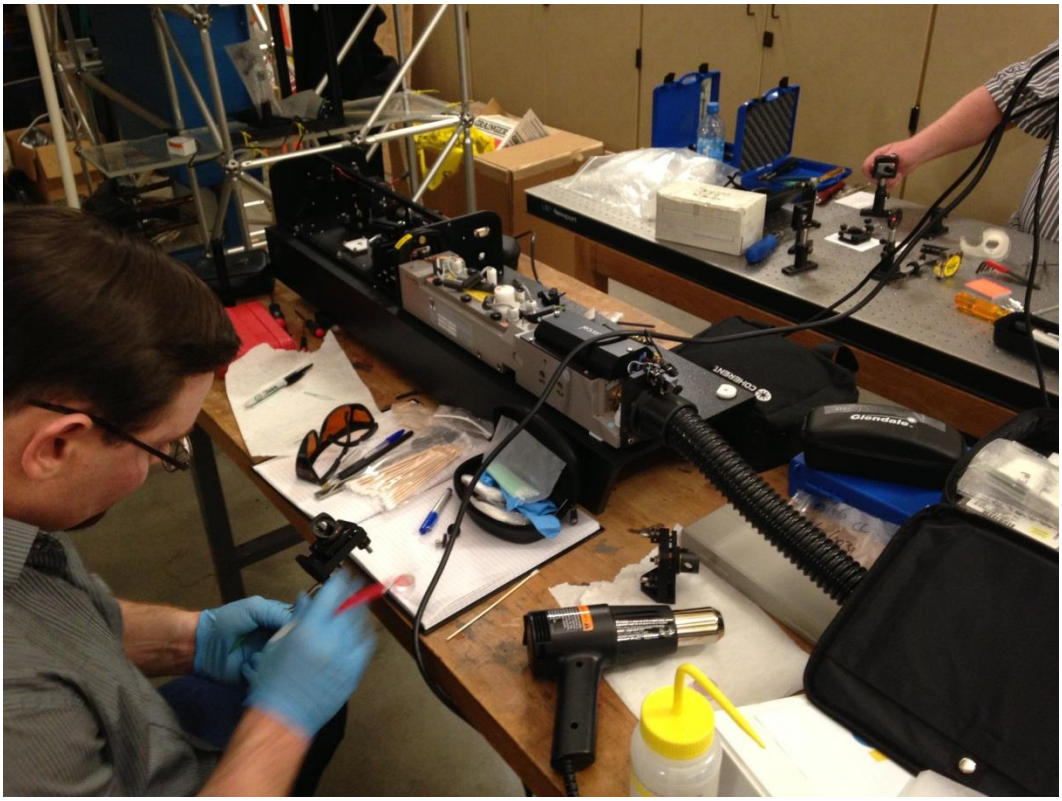

# I. Optics

## A. Cleaning and Replacement of Lenses

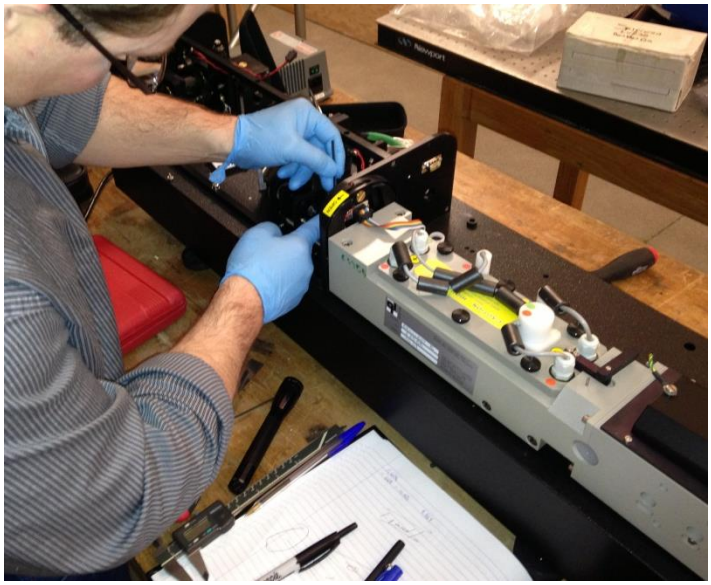

1. Initially, inspect each component of the YAG laser optics section for damage and/or dirt and the condition of the optics to determine whether a lens, mirror, etc. needs to be replaced or simply cleaned.
2. If an optical component has a distinct laser-marking (resulting from laser damage) it must be removed and replaced.
3. Remove the black mount and lens/mirror together and access whether the face can be cleaned.
4. Use optical cleaning Q-tips with

acetone (never to be used with regular cotton swabs as it will eat away at the material leaving a significant amount of residue) and/or isopropyl to clean the faces of the optics. (Be extremely cautious regarding scratching the lens or mirror and only use appropriate cotton swabs)

5. To remove a specific component from its black holding cell, first mark the position of the lens mount in order to have a reference when putting the piece back on since the position is important for alignment purposes later.
6. Use a standard hot air gun to melt the adhesive holding the lens to the black mount and separate it from its position. (Do not use a hot air gun if the lens is to be salvaged in any way as the hot air will melt the material coatings on the lens as well as the adhesive)
7. Scrape off the reaming glue on the black lens-housing piece with an X-Acto knife.
8. Once the new lens or mirror is sufficiently cleaned carefully place it in the black mount, taking particular notice to the direction of the convex/concave side of the lens.
9. Carefully glue down using an incredibly conservative amount of UV epoxy by dipping it down in three places around the edge of the lens before curing it using a UV light source. (UV epoxy is used for the lenses to be fast acting and produces no heat that might damage the component while curing)
10. Once set into the black mount piece, return the component to its position on the laser taking note to align the marks written before removal. (If replacing the lens components in the telescope, section avoid moving the actual positions of the pieces as the distances are important for the laser path)

## B. Cleaning and Replacement of Dichroic Filters

1. If any of the turning mirrors and dichroic filters have unacceptable laser damage and marks, follow a similar approach to the cleaning and replacement of the lenses for these components. (The dichroic components are highly translucent at 1064nm and highly reflective at 532nm and therefore have distinctive visual differences between the two faces, which is extremely important to note when removing and replacing from their mount)
2. Remove the dichroic filter from their respective mounts with a hot air gun and carefully clean the new piece being cautious about damage/scratching the anti-reflective coating on the faces.
3. Use a similar process to reinstall the dichroic filters although instead of using the UV epoxy, glue the pieces in place using Scotch-Weld Epoxy Adhesive Tube


**Translucent Side**


**Reflective Side**

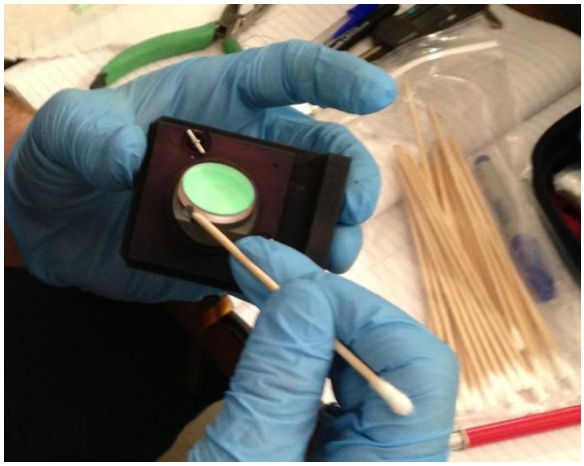

Kit (2216 B/A Gray). (Requires a long duration for the adhesive to cure so leave in a clean and dry place)

### C. Cleaning and Replacement of Other Components

1. Dust and clean the rest of the optical section of the laser for dust and dirt being sure to use appropriate cleaning tools for lenses, mirrors, and other sensitive optical equipment. Paper towels and cotton swabs are sufficient for open surfaces of this section.
2. If the 1064nm dump is cracked, damaged, or needs replacing remove it from its position and use Scotch-Weld epoxy to either glue shards back together or a new dump on the mount.

## II. Laser

Following the cleaning, repair, and replacement of the optical components of the laser the next step involved the actual laser and alignment in its housing shell.

### A. Cleaning and/or Replacement of Laser Rod and Other Components

1. Remove the pocket cell driver from the back of the laser section as well as the shutter on the front of the output coupler.
2. With the power completely off and path of the laser blocked after the polarizer, shine a flashlight down the back of the laser rod and inspect the faces of the laser rod for damage and marks. (WARNING: Power off and laser path blocked will eliminate the possibility of laser light damaging your eyes while inspecting the rod)
3. If the laser rod requires cleaning and/or replacement, before removing the components to access and clean the rod, first setup a station for alignment purposes as shown in the picture below. Use a HeNe laser and project its path down a meter and then turn two 90degree turns and shine on the face of the laser rod. Make sure that the beam path is level and hitting straight on the center of mirrors and rod after going through a target hole (alignment tool that only allows a “pin-hole” size of the laser through). Position the laser in line with the HeNe laser, raised on two cylindrical Al mounts on each corner and use a target hole alignment tool to level the beam at 43mm (height the center of the laser rod will be if positioned on two cylindrical Al mounts). Fine tune and adjust the laser path and laser chamber so that the beam goes perfectly through the laser rod and hits the back HR mirror.

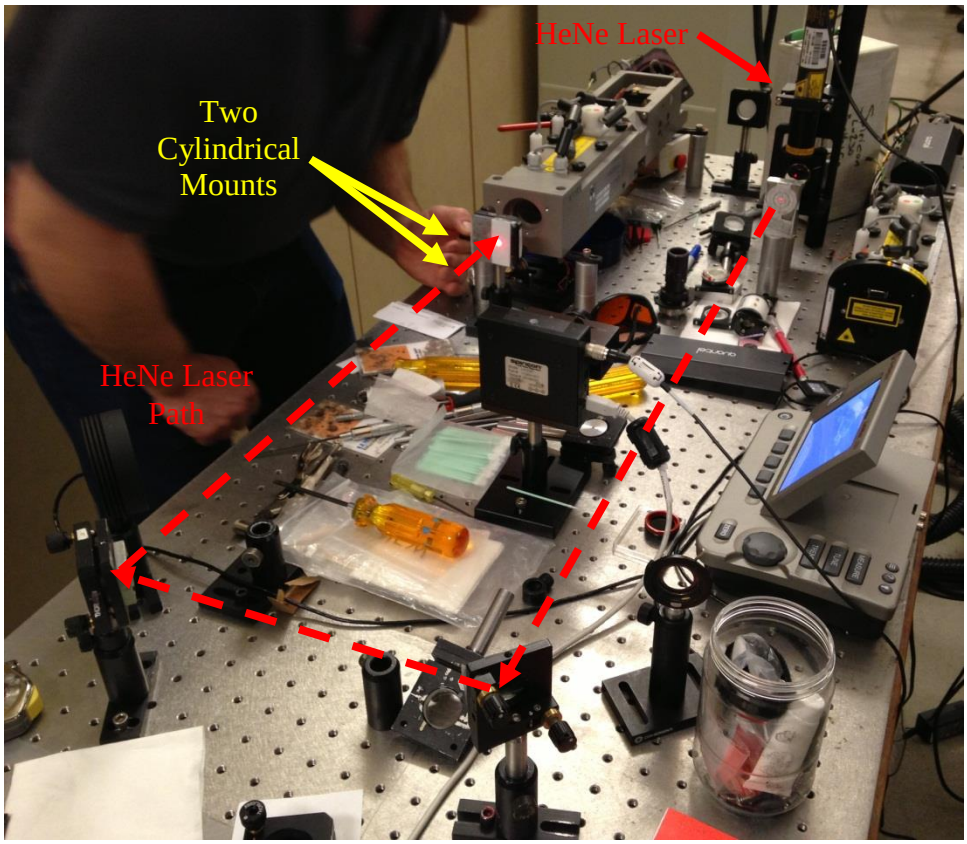


4. Once the laser is aligned with the HeNe the components of the laser may be removed for cleaning. With the power completely disconnected remove flashlamp cover by first unplugging the main power leads (noting the color stickers indicating the path traveled in series) and then dislodging the entire piece with the jack or carefully using an X-Acto knife to separate it from its underlying suction around the edge.

5. If the laser rod, surrounding glass tube, and other components have significant grime, dirt (strong discoloration and forming algae as a result of the high levels of moisture and/or not cycling the laser's DI water through the system as often as required - at least once a week for an hour), or damage they must be removed and cleaned, or replaced.
6. To remove the laser rod first remove the polarizer at the back followed by the output coupler in order to gain access to the screws holding the rod mounts in place. Use an extended screw driver to remove the laser mounts.
7. Next to remove the laser rod, dislodge the rod from its O-rings at both ends by carefully clamping the rod in between the surrounding glass tube and frame edge, as shown in the

figure below. Twist until the rod is loose and then use this access point to slowly and carefully push the rod out (this method is used to avoid touching the two faces of the rod).

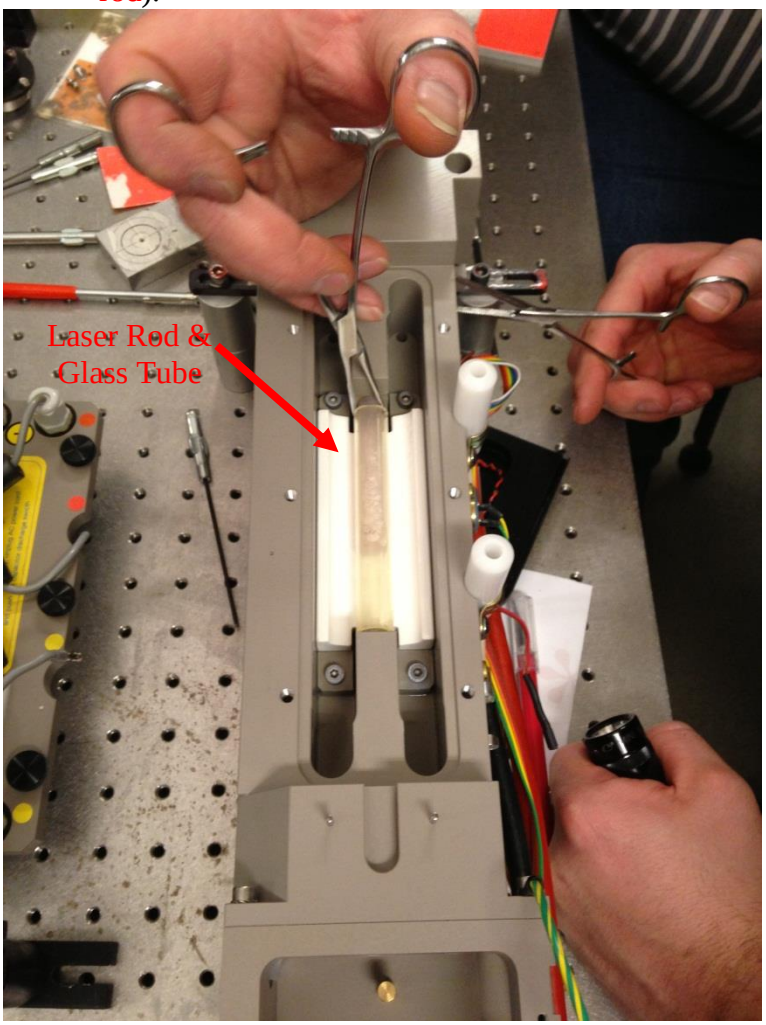



8. Once the rod is removed clean faces as well as the entire outside using optical cotton swabs and optics paper with acetone and isopropyl. Similarly, clean the glass tube and additional component in the flashlamp/rod chamber.
9. Reinstall the laser rod using a similar approach as the removal being extremely cautious about touching the faces of the rod. Reinstall the O-rings and laser rod mounts. (The laser rod is wedged so when reinstalling it use the

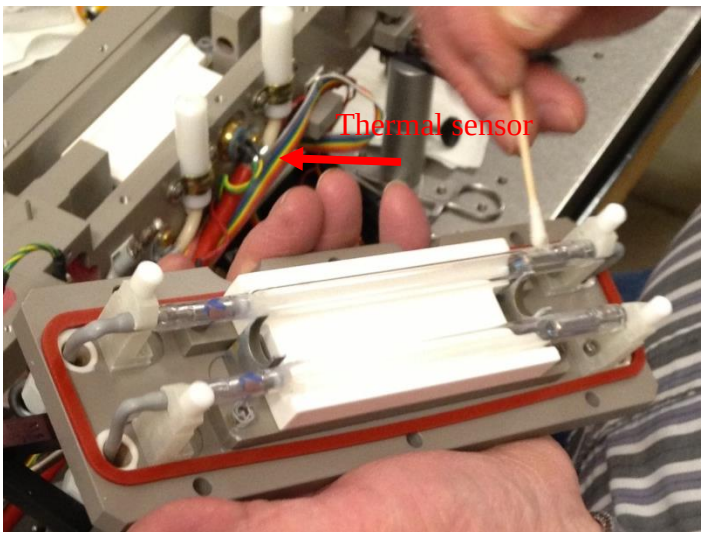

already aligned HeNe laser to position the rod correctly so that reflection of the HeNe on the front face of the rod is off to the left as it was before)

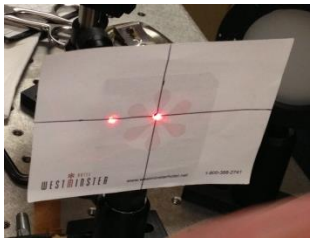

10. Again check the reinstalled rod for marks and damage before proceeding to reinstall the flashlamp cover and reconnect the main power leads.
11. Check that the thermal sensor switch is not popped out of its position. (In the event that the laser is running without sufficient cooling this temperature sensor will register an overheating and pop out, disconnecting the circuit, thus disabling the laser)
12. Carefully clean additional components of the laser's oscillator chamber.

## B. Operating and Maintenance of Water Cooling System

The YAG laser requires a Quantel DI water cooling system that will only operate at 38 degrees C and an additional chiller. The Quantel water cooling system requires new DI water and filter frequently.

1. To operate the water cooling system for the appropriate laser, simply turn the power key.
2. Before using the laser, make sure the chiller is also powered on and running correctly. If an error occurs on startup of the pumping, it is most likely the bypass valve on the side of the system as seen in the picture to the right.

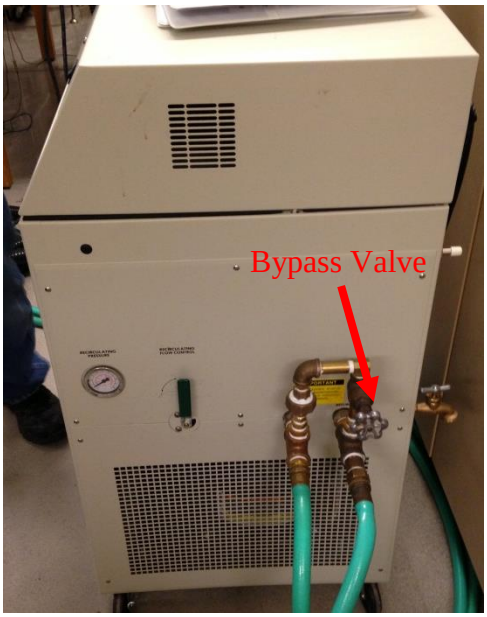



3. To replace the DI water in the system's reservoir slide out the bottom shelf and open remove the reservoir cap. Syphon the old DI water out and then pour in the new DI water using a large funnel.
4. Reconnect the reservoir cap and turn on the water cooling system to cycle the water through the laser system flush remaining old water. Turn the system on and wait to see bubbles in the tube connection at the laser end. Wait a few seconds and turn off the cooling system, wait 5 sec, and then turn back on and again check for bubbles. Repeat until all air bubbles have been removed from the cooling system.

5. Recycle the DI water until the system is sufficiently clean and only new DI water is left inside.
6. If additional problems exist between the cooling system and the laser, the systems' CPU boards may need to be replaced. Before removing the CPU board, check the continuity of the connections between the laser and CPU board using a digital multimeter. Also check the connections in the pocket cell driver to determine which component is actually not functioning properly. (Use a wrist grounding strap when working with these electrical and computer circuits as a slight discharge of static electricity may damage the components of the circuit boards)
7. In the rare case where a CPU board is likely the problem, remove and switch the two boards. If the problem is rooted in the CPU board and a new one is available begin by unscrewing the front cover of the water cooling system.
8. Carefully remove the wires and connections and unscrew the CPU board from its mount. To replace the CPU board the two software chips must be removed and placed on the new board. One is indicated by the written label and the other is underneath the elevated board, which must be removed first, as indicated in the picture below.

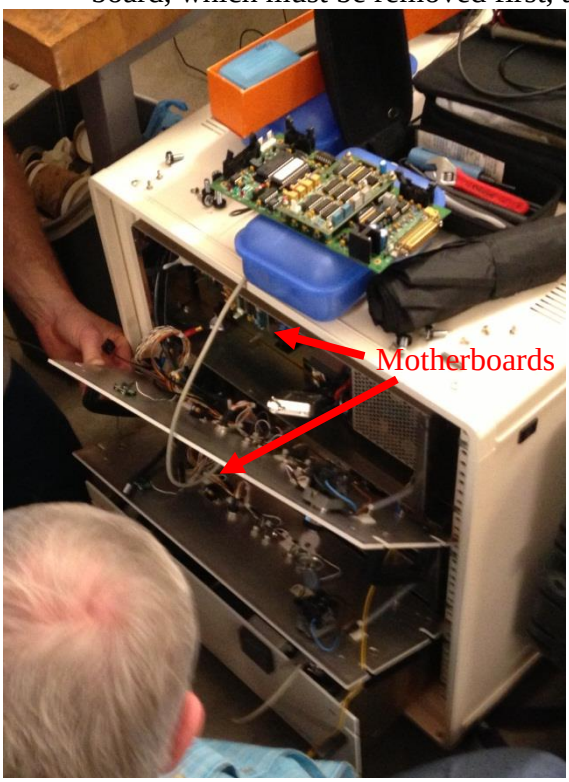


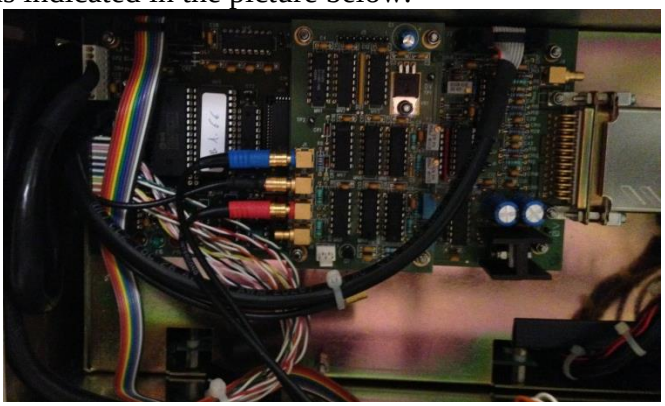

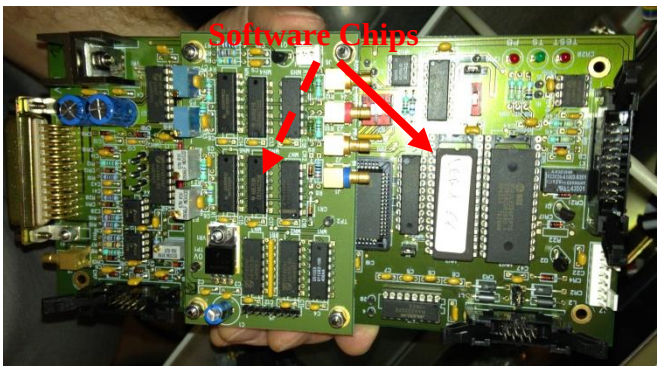


9. Reconnect CPU board, cords, and front cover and test the system.

## C. Realignment of Laser and Oscillator Components

When the "Quality" is of the Q-switch is based on the oscillation of the laser light emitted by the flashlamp and rod between the polarizer and HR mirror. If the components are misaligned the laser may be turned or cutoff to an unacceptable and unusable result. After the components are cleaned and replaced it is essential to align these correctly step by step.

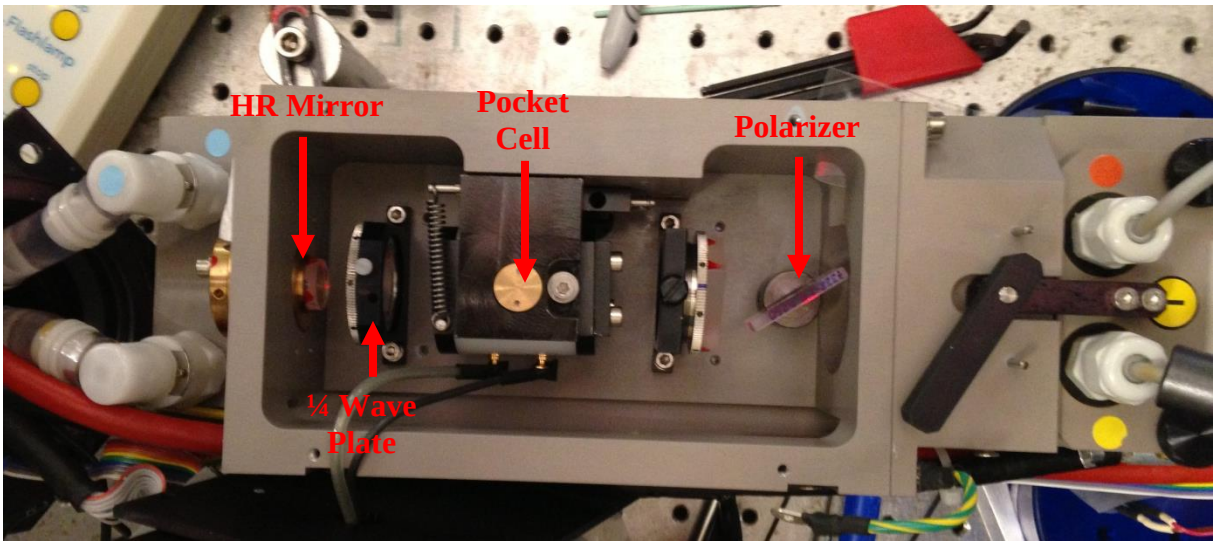


1. When the output coupler is reinstalled the reflection from its face will appear off to the left as shown in the picture below (use a cross-hair paper with a center hole to capture the reflecting beam).

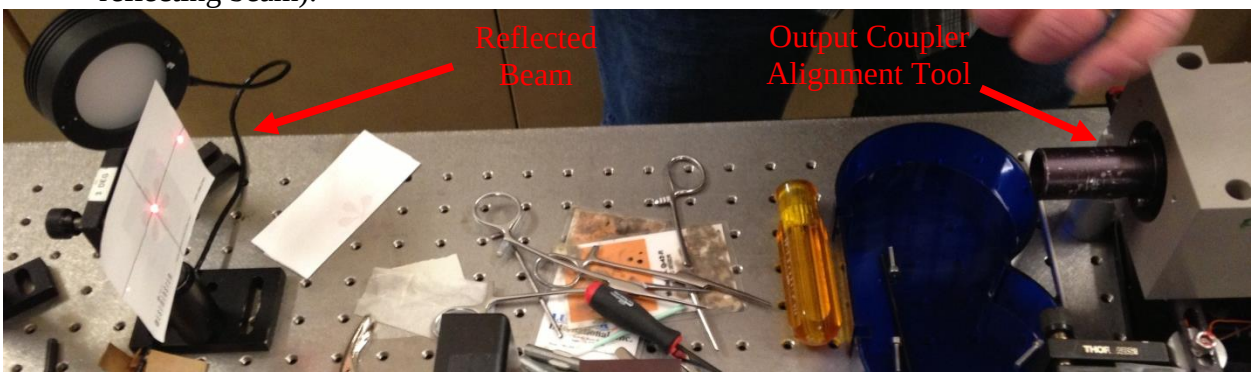


2. To reinstall correctly and align the oscillator components into the laser chamber the Q-switch function of the laser is necessary as well as a setup of mirrors, power meter, and specific camera for analyzing the beam profile of the laser's Q-switch mode, as shown in the picture on the following page (The interlocks on the full laser mount must be disconnected/bypassed in order to run the laser detached from the main body). A basic method can be used simply with burn paper and a power meter. (WARNING: Always use burn paper appropriate for laser work/alignment and always use in plastic bag as the dust from the burning paper will dirty sensitive components)
3. Position each component into the oscillator section of the laser and monitor the profile and power reading (maximum around 800mJ for these lasers). Make minor adjustments to the components to maximize the power, while keeping a quality laser profile. (The picture to the right illustrates the laser profile using Quantel alignment/profile tools and software. Note the "donut" shape and equal size of edges indicating that the components do not cutoff the beam nor produce unwanted turning)

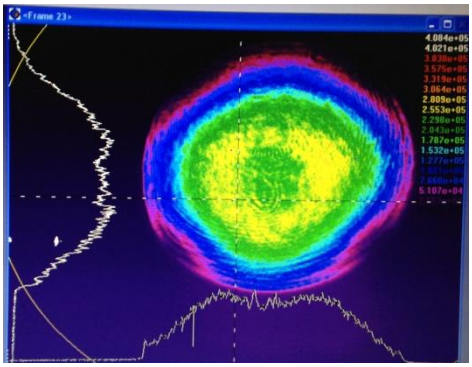

4. Once the profile is sufficient and alignment completed with maximum power and quality of the beam, reconnected the walls to the oscillator chamber and the pocket cell driver.

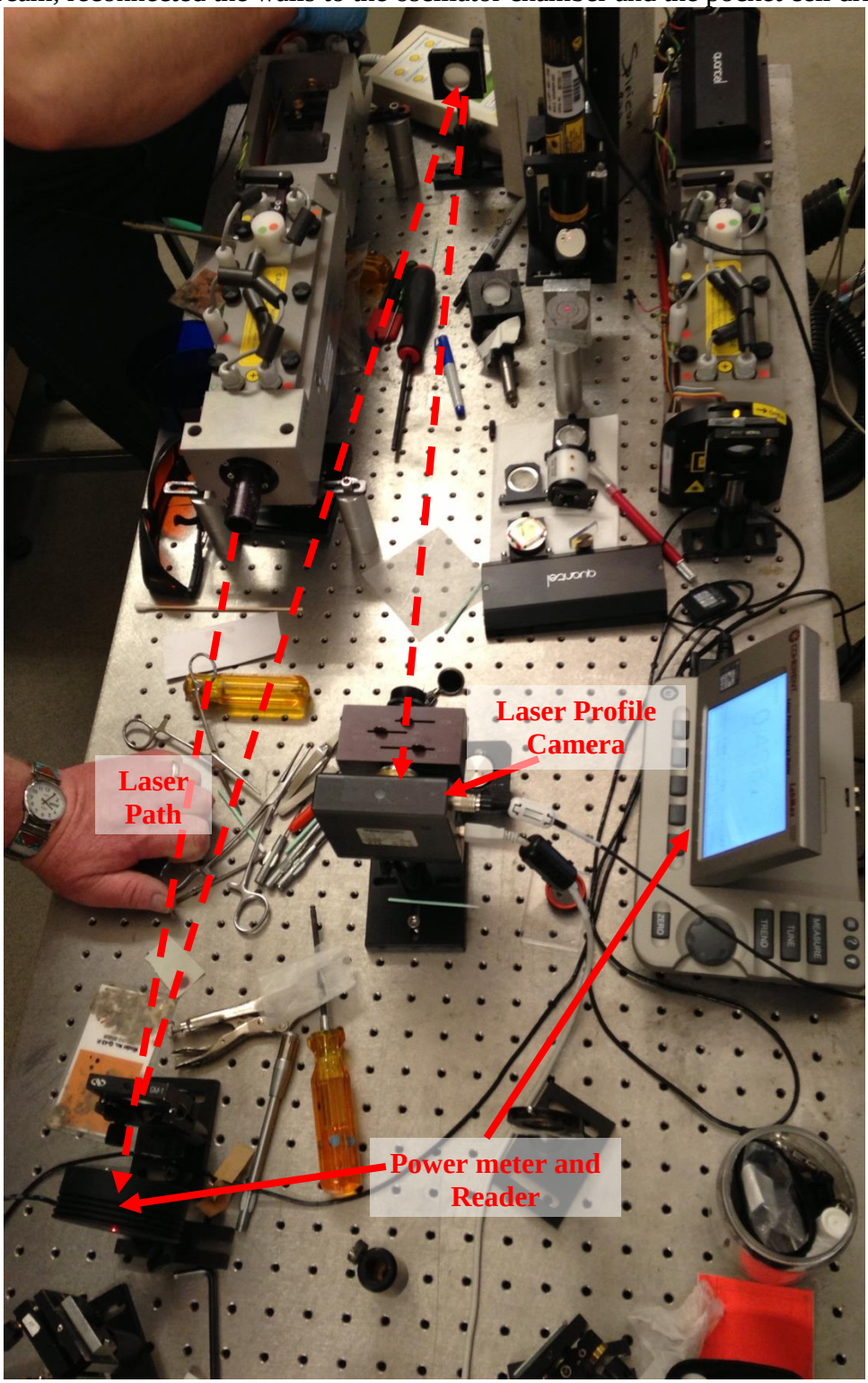

# III. Reassembly

## A. Rejoining Lasers on Mount

1. Begin reassembly of the system by remounting laser 1 and laser 2 onto the full body mount. Reconnect shutters and bypassed interlocks before proceeding.

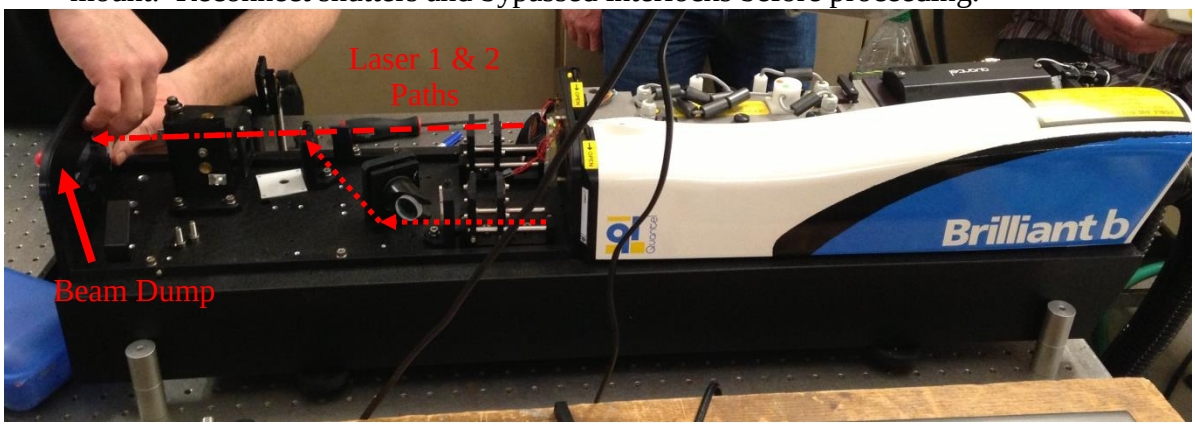


2. For each of the two lasers, align the optical components so that the beams travel straight into the crystal housing cell and hit the 1064nm dump at the far end. (Use burn paper in a plastic bag and a single Q-switch pulse to measure location and profile of beam along its path to the 532nm output shutter) Adjust the polarizer, lenses, and mirrors before fine-tuning the telescopes, remembering the importance of the distances between the lenses in the telescope sections.

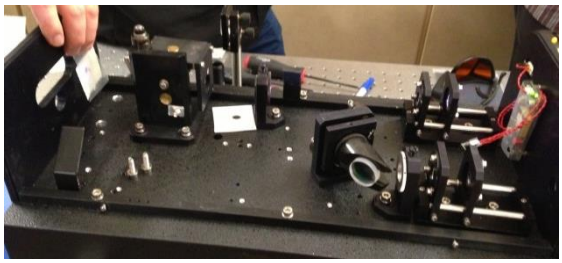

3. Adjust the crystal cell position and tilt as well as the two dichroic mirrors in order to maximize the 532nm beam through the output shutter.

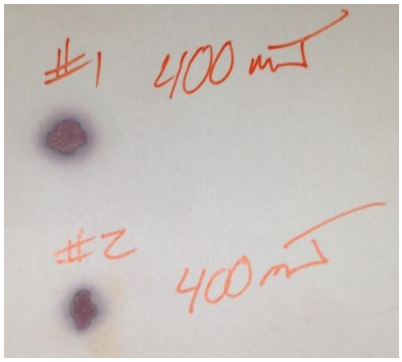


4. Test the Q-switch energy of the 532nm beam for the two lasers separately and make sure that both the energy (maximized at 400mJ each) and beam profile are sufficient. (Notice the horizontal and vertical stretches between the two beams as shown in the beam profile picture below) (When using an energy or power meter always mount the meter at a slight tilt since even a small percentage of the laser reflected back from the meter's face directly through to the internal components can cause severe damage)
5. If the energy is not optimized for 400mJ out of each laser check the voltage of the flashlamps from the two remote boxes, which should be around 1540V. Next, under the Q-switch menu scroll down to the Q-switch delay (*FL-QS Dly: 500uS*). Start with the delay set to 500uS and with the Q-switch on continuous, begin decreasing the delay while observing the energy of the output beam. The optimal delay to achieve maximum energy of 400mJ out of each laser is

approximately 215uS. (Going outside of the range of the Q-switch delay, between 200uS and 500uS, may damage the laser system)